CMS Draft Analysis Note

The content of this note is intended for CMS internal use and distribution only

Measurement of differential top-quark pair production cross sections in the dilepton final state at $\sqrt{s} = 8\,\text{TeV}$

I. Asin, N. Bartosik, O. Behnke, C. Diez Pardos, G. Dolinska, T. Dorland, J. Hauk, J. Kieseler, I. Korol, and A.B. Meyer

DESY

Abstract

Normalised differential top-quark pair production cross sections are measured in pp collisions at $\sqrt{s} = 8\,\text{TeV}$ using the decay channels into two opposite-sign leptons (muons or electrons). The analysed dataset was recorded in 2012 and corresponds to an integrated luminosity of 19.7 fb^{-1}. The $t\bar{t}$ cross section is measured differentially as a function of kinematic observables of the final state leptons, jets associated to b-quarks, and the top quarks. The differential cross sections are measured within a visible phase space and normalised to the corresponding inclusive cross section. For the top quarks, the measurement is performed in the full phase space. From the same analysis, a measurement of the absolute total $t\bar{t}$ production cross section yields a result of $\sigma_{t\bar{t}} = 245.10 \pm 1.05\,(stat.) \pm 14.25\,(syst.) \pm 14.29\,(total)$ pb.

Contents

1 Introduction

A measurement of the $t\bar{t}$ quark pair production cross section in pp collisions at $\sqrt{s} = 8\,\text{TeV}$ is presented using CMS data recorded in 2012 and corresponding to an integrated luminosity of $19.7\,\text{fb}^{-1}$. The $t\bar{t}$ signal is reconstructed in the decay channel into two leptons (electron or muon) in the final state. Experimentally, the dilepton channel is characterised by two isolated, opposite-charged leptons with high transverse momentum, two energetic jets associated to b quarks or antiquarks from the t and $\bar{t}$ quark decays, and large missing transverse energy $\not{E}_{\text{T}}$, due to the neutrinos from the W-boson decays. Backgrounds originate dominantly from Z/γ^*-boson production with additional jets (referred to as Z+jets) and QCD processes and are suppressed by requirements on the isolation of the leptons, the dilepton invariant mass, the missing energy, and by b-tagging.

Using the selected data sample, the total inclusive $t\bar{t}$ production cross section and the normalised differential cross section are measured by determining the number of signal events above background and correcting for losses due to finite experimental detection efficiencies, such as the trigger and reconstruction efficiencies and detector acceptance.

For the measurement of the inclusive cross section, theoretical predictions are used to extrapolate the result into the full phase space. In contrast, for the differential cross section measurement, the results are given in a visible range of the phase space, defined here as $p_T^\ell > 20$ GeV, $|\eta^\ell| < 2.4$, $p_T^b > 30$ GeV and $|\eta^b| < 2.4$, where p_{T} and $|\eta|$ are the transverse momenta and pseudorapidities, respectively, and ℓ and b stand for the final-state charged leptons and jets associated to b quarks or antiquarks (referred to as b jets), respectively. In order to allow for comparison with the latest NLO+NNLL [1, 2] and approximate NNLO predictions [3], top quark and top-quark pair differential cross sections are measured in the full phase space.

The differential cross sections are normalised to the measured inclusive cross section in the corresponding kinematic range. Thus, all global systematic uncertainties affecting the absolute normalisation of the cross section measurement, such as the uncertainty on the integrated luminosity or the branching ratios of the top decay channels, and also a large portion of the experimental uncertainties, are removed. The $t\bar{t}$ production cross section is measured as a function of the transverse momentum of the leptons p_{T}^ℓ, the pseudorapidity of the leptons, η^ℓ, the transverse momentum of the lepton pair $p_{\text{T}}^{\ell\ell}$, the invariant mass of the lepton pair $m^{\ell\ell}$, the transverse momentum of the b jets p_{T}^b, the pseudorapidity of the b jets η^b, the transverse momentum of the b jet pair $p_{\text{T}}^{b\bar{b}}$, the invariant mass of the b jet pair $m^{b\bar{b}}$, the invariant mass of the lepton-bjet system, $m^{\ell b}$, the transverse momentum of the top quarks p_{T}^t, $p_{\text{T}}^{Lead.t}$, $p_{\text{T}}^{NLead.t}$, the transverse momentum of the top quarks measured in the $t\bar{t}$ rest frame $p_{\text{T}}^t(t\bar{t})^*$, the rapidity of the top quarks y^t, the difference in azimuthal angle between the top quarks, $\Delta\phi(t,\bar{t})$, the difference of the absolute values of the top quark rapidities, $|y^t| - |y^{\bar{t}}|$, the transverse momentum of the top-quark pair $p_{\text{T}}^{t\bar{t}}$, the rapidity of the top-quark pair $y^{t\bar{t}}$, the invariant mass of the top-quark pair $m^{t\bar{t}}$.

The top-quark candidates and their kinematic properties are reconstructed using a kinematic top mass reconstruction algorithm similar to the MWT methods described in [4] and [5].

In this analysis, the differential cross sections are corrected for detector efficiencies and acceptances using a regularized unfolding procedure. The size of the bins of the measurement are chosen such that the purity and stability in each bin is larger than 50%, as is explained in the text.

The results are compared to theory predictions obtained with MADGRAPH [6], MC@NLO [7],

POWHEG [8–10], and to the latest NLO+NNLL [1, 2] and approximate NNLO calculations [3]. The measurement presented here follows the same event selection and analysis strategy as described in Ref. [11] for 7 TeV data.

The structure of the document is the following. In Section 2 the data and simulated samples used for the analysis are given. The event selection is described in Section 3. Comparisons between the distributions in the data and in the simulations are provided in Section 4. The methods to determine the contributions from non-$t\bar{t}$ background are detailed in Section 5. For the measurement of the differential cross sections, an algorithm to reconstruct the top-pair kinematics is applied. Details of this kinematic reconstruction are given in Section 6. The corrections to the signal event selection efficiency determined from data and the estimated systematic uncertainties to the measurement of the cross sections are described in Section 7. The absolute inclusive and normalised differential cross section definitions are described in Section 8, and the results on the inclusive cross section and the normalised differential cross section measurements are presented in Section 9.

2 Data and Simulated Samples

The signal processes in this analysis is the production of $t\bar{t}$ quark pairs followed by top quark decays $t \rightarrow W^+b$ and $\bar{t} \rightarrow W^-\bar{b}$, and subsequent leptonic W-boson decays into muons or electrons.

The data set, collected during the LHC 2012 run period, used in this analysis are listed in Table 1. From this data set, certified runs are selected by application of the certified good-run lists as given in [12]. The total integrated luminosity of the complete data sample is $19.7\,\mathrm{fb}^{-1}$ $\pm\,0.9\,\mathrm{fb}^{-1}$ [13].

Table 1: Collision data samples used in the analysis.

Sample	Events	Run range
/DoubleElectron/Run2012A-22Jan2013-v1/AOD	13M	190456–193621
/DoubleElectron/Run2012B-22Jan2013-v1/AOD	23.5M	193834–196531
/DoubleElectron/Run2012C-22Jan2013-v1/AOD	39M	198022–203742
/DoubleElectron/Run2012D-22Jan2013-v1/AOD	34.5M	203777–208686
/DoubleMu/Run2012A-22Jan2013-v1/AOD	5.6M	see *ee* channel
/DoubleMuParked/Run2012B-22Jan2013-v1/AOD	29M	see *ee* channel
/DoubleMuParked/Run2012C-22Jan2013-v1/AOD	37M	see *ee* channel
/DoubleMuParked/Run2012D-22Jan2013-v1/AOD	38M	see *ee* channel
/MuEG/Run2012A-22Jan2013-v1/AOD	2.5M	see *ee* channel
/MuEG/Run2012B-22Jan2013-v1/AOD	15M	see *ee* channel
/MuEG/Run2012C-22Jan2013-v1/AOD	21M	see *ee* channel
/MuEG/Run2012D-22Jan2013-v1/AOD	22M	see *ee* channel

Simulated data samples from the *Summer12* simulation processing, comprising the $t\bar{t}$ signal and the relevant background processes, are used in the analysis. The simulated background contributions stem from Z+jets, $t\bar{t}$ production in association with $W/Z/\gamma$ bosons, tW, W+jets and dibosons (WW, WZ, and ZZ). For the simulation of the QCD background, a lepton-enriched sample (QCD sample hereafter) consisting of a muon-enriched sample with is used for the $\mu^+\mu^-$ and $\mu^\pm e^\mp$ channels, whereas an electron-enriched sample (split into three p_T regions $20\,\mathrm{GeV} \leq p_\mathrm{T} < 30\,\mathrm{GeV}$, $30\,\mathrm{GeV} \leq p_\mathrm{T} < 80\,\mathrm{GeV}$, $80\,\mathrm{GeV} \leq p_\mathrm{T} < 170\,\mathrm{GeV}$, and split into light and heavy flavour) is used for the e^+e^- channel. The Z+jets background samples are generated

126 with MADGRAPH [6] and interfaced with PYTHIA [14] for hadronisation and parton fragmen-
127 tation. The Z+jets simulation is split into two samples for the invariant dilepton mass ranges of
128 10–50 and > 50 GeV. The tW process is simulated with POWHEG [8–10] and uses PYTHIA [14]
129 to simulate the hadronisation and fragmentation steps. The $t\bar{t}$ production in association with
130 bosons (W, Z and γ) is generated with MADGRAPH interfaced with PYTHIA. The diboson
131 samples are produced with PYTHIA [14], as well as the QCD sample. The central $t\bar{t}$ simula-
132 tion is produced using MADGRAPH [6] using the MADSPIN [15] package and interfaced with
133 PYTHIA [14]. The same tools are used to simulate model dependencies on Q^2, jet-parton match-
134 ing or top quark mass. Additional signal samples are used to determine the model uncertainty
135 of the measurement and are generated using POWHEG [8–10] and MC@NLO [7], interfaced with
136 PYTHIA [14] and HERWIG [16], respectively, for hadronisation and parton fragmentation.

137 For comparison with the measured distributions, the events in the simulated data samples are
138 normalised to an integrated luminosity of 19.7 fb^{-1}. The predicted cross sections used for these
139 samples are based on Ref. [17], except for the $t\bar{t}$ sample, and are shown in Table 2. The $t\bar{t}$ signal
140 sample is normalised to the data to present expected rates in all figures prior to Section 9.

Table 2: Summary of simulated data samples used in this analysis, together with the cross section assigned to the process.

Sample	cross section [pb]
/TTJets_MSDecays_central_TuneZ2star_8TeV-madgraph-tauola/Summer12_DR53X-PU_S10_START53_V19-v1	–
/Tbar_tW-channel-DR_TuneZ2star_8TeV-powheg-tauola/Summer12_DR53X-PU_S10_START53_V7A-v1	11.1
/T_tW-channel-DR_TuneZ2star_8TeV-powheg-tauola/Summer12_DR53X-PU_S10_START53_V7A-v1	11.1
/TTWJets_8TeV-madgraph/Summer12_DR53X-PU_S10_START53_V7A-v1	0.232
/TTZJets_8TeV-madgraph_v2/Summer12_DR53X-PU_S10_START53_V7A-v1	0.2057
/TTGJets_8TeV-madgraph/Summer12_DR53X-PU_S10_START53_V19-v1	1.8
/WJetsToLNu_TuneZ2Star_8TeV-madgraph-tarball/Summer12_DR53X-PU_S10_START53_V7A-v2	36257.2
/DYJetsToLL_M-10To50filter_8TeV-madgraph/Summer12_DR53X-PU_S10_START53_V7A-v1	860.5
/DYJetsToLL_M-50_TuneZ2Star_8TeV-madgraph-tarball/Summer12_DR53X-PU_S10_START53_V7A-v1	3503.71
/WW_TuneZ2star_8TeV_pythia6_tauola/Summer12_DR53X-PU_S10_START53_V7A-v1	54.838
/WZ_TuneZ2star_8TeV_pythia6_tauola/Summer12_DR53X-PU_S10_START53_V7A-v1	33.21
/ZZ_TuneZ2star_8TeV_pythia6_tauola/Summer12_DR53X-PU_S10_START53_V7A-v1	17.654
/QCD_Pt_20_MuEnrichedPt_15_TuneZ2star_8TeV_pythia6/Summer12_DR53X-PU_S10_START53_V7A-v3	134680.0
/QCD_Pt_20_30_EMEnriched_TuneZ2star_8TeV_pythia6/Summer12_DR53X-PU_S10_START53_V7A-v1	29148.6
/QCD_Pt_30_80_EMEnriched_TuneZ2star_8TeV_pythia6/Summer12_DR53X-PU_S10_START53_V7A-v1	4615893.0
/QCD_Pt_80_170_EMEnriched_TuneZ2star_8TeV_pythia6/Summer12_DR53X-PU_S10_START53_V7A-v1	183294.9
/QCD_Pt_20_30_BCtoE_TuneZ2star_8TeV_pythia6/Summer12_DR53X-PU_S10_START53_V7A-v1	167388.0
/QCD_Pt_30_80_BCtoE_TuneZ2star_8TeV_pythia6/Summer12_DR53X-PU_S10_START53_V7A-v1	167040.0
/QCD_Pt_80_170_BCToE_TuneZ2star_8TeV_pythia6/Summer12_DR53X-PU_S10_START53_V7A-v1	12981.9
/TT_CT10_TuneZ2star_8TeV-powheg-tauola/Summer12_DR53X-PU_S10_START53_V7A-v1	
/TT_CT10_TuneZ2star_8TeV-powheg-tauola/Summer12_DR53X-PU_S10_START53_V7A-v2	
/TT_8TeV-mcatnlo/Summer12_DR53X-PU_S10_START53_V7A-v1	
/TTJets_MSDecays_matchingup_TuneZ2star_8TeV_madgraph_tauola/Summer12_DR53X_PU_S10_START53_V19_v2	
/TTJets_MSDecays_matchingdown_TuneZ2star_8TeV_madgraph_tauola/Summer12_DR53X_PU_S10_START53_V19_v2	
/TTJets_MSDecays_scaleup_TuneZ2star_8TeV_madgraph_tauola/Summer12_DR53X_PU_S10_START53_V19_v1	
/TTJets_MSDecays_scaledown_TuneZ2star_8TeV_madgraph_tauola/Summer12_DR53X_PU_S10_START53_V19_v1	
/TTJets_MSDecays_mass173_5_TuneZ2star_8TeV_madgraph_tauola/Summer12_DR53X_PU_S10_START53_V19_v1	
/TTJets_MSDecays_mass171_5_TuneZ2star_8TeV_madgraph_tauola/Summer12_DR53X_PU_S10_START53_V19_v1	

2.1 Event Cleaning and Trigger Selection

142 Events are required to fulfill the good-run selection described above. In a first step, beam
143 scraping events are rejected by selecting a significant fraction of high-purity tracks with respect
144 to the total number of tracks ($> 25\%$) if the event has at least 10 tracks. Events with significant
145 noise in the hadronic calorimeters are also removed. In addition, the presence of a non-fake
146 primary vertex with ndof > 4, $|\rho| < 2$ cm, and $|z| < 24$ cm is required.

147 Several dilepton triggers are used for the trigger selection in the data and in MC as detailed in
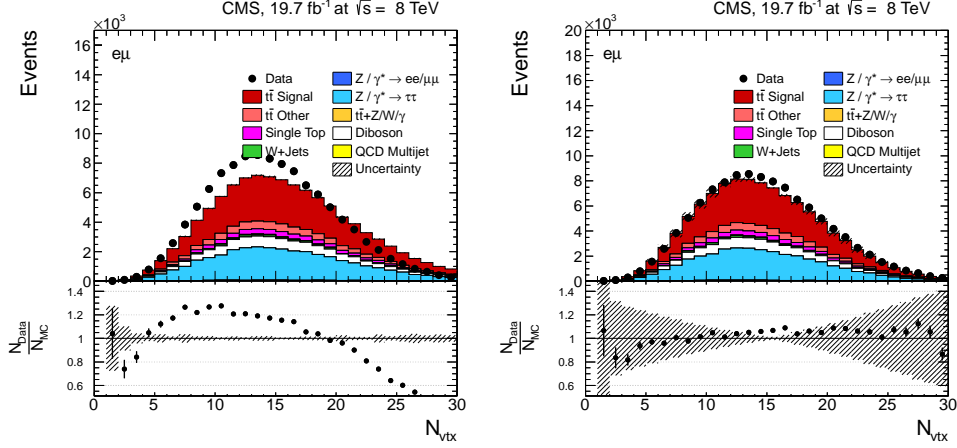
Figure 1: Distribution of the number of primary vertices in the $\mu^\pm e^\mp$ channel before and after pile-up reweighting. The plot is created after the selection of one isolated muon and one isolated electron with only an invariant mass requirement of 20 GeV. The shaded area indicates the uncertainties on the $t\bar{t}$ signal.

Table 3. A logical "OR" between the different trigger terms is applied to the entire 2012 data in each channel.

Table 3: Triggers used in data and in simulation for the three dilepton channels.

sample	channel	trigger
data	$\mu^+\mu^-$	HLT_Mu17_Mu8_v*
data	$\mu^+\mu^-$	HLT_Mu17_TkMu8_v*
MC	$\mu^+\mu^-$	HLT_Mu17_Mu8_v17
MC	$\mu^+\mu^-$	HLT_Mu17_TkMu8_v10
data	e^+e^-	HLT_Ele17_CaloIdT_CaloIsoVL_TrkIdVL_TrkIsoVL_ Ele8_CaloIdT_CaloIsoVL_TrkIdVL_TrkIsoVL_v*
MC	e^+e^-	HLT_Ele17_CaloIdT_CaloIsoVL_TrkIdVL_TrkIsoVL_ Ele8_CaloIdT_CaloIsoVL_TrkIdVL_TrkIsoVL_v17
data	$\mu^\pm e^\mp$	HLT_Mu17_Ele8_CaloIdT_CaloIsoVL_TrkIdVL_TrkIsoVL_v*
data	$\mu^\pm e^\mp$	HLT_Mu8_Ele17_CaloIdT_CaloIsoVL_TrkIdVL_TrkIsoVL_v*
MC	$\mu^\pm e^\mp$	HLT_Mu17_Ele8_CaloIdT_CaloIsoVL_TrkIdVL_TrkIsoVL_v7
MC	$\mu^\pm e^\mp$	HLT_Mu8_Ele17_CaloIdT_CaloIsoVL_TrkIdVL_TrkIsoVL_v7

3   Event Selection

The analysis is performed using the CMS software version `CMSSW_5_3_14_patch1` and the Physics Analysis Toolkit (PAT) [18]. The object reconstruction and identification follow the configuration settings recommended by the Top Physics Analysis Group for dilepton final states [19] with minor modifications to ensure the same phase space for all objects. It is done using the PF2PAT algorithm. It is configured to perform a charged-hadron subtraction (pfNoPileUp) to remove pile-up. Muons (pfNoMuon) and electrons (pfNoElectron) are projected out from the particle-flow candidates before clustering jets. Because pfNoPileUp can only remove charged hadrons, the L1FastJet algorithm is applied to subtract the remaining neutral components. The complete jet energy scale correction contains the steps L1FastJet, L2Relative, L3Absolute and L2L3Residual. The simulation is reweighted to describe the pile-up distributions in the data. In Figure 1, the distribution of the number of primary vertices is shown before and after reweighting for the $\mu^\pm e^\mp$ channel.

163 Signal events are required to have at least two oppositely-charged leptons fulfilling the isolation
164 and identification criteria, as described in the following.

3.1 Muon Selection

166 Muon candidates are reconstructed using the particle-flow algorithm [20] and are required to
167 have a transverse momentum $p_T > 20\,$GeV within a pseudorapidity $|\eta| < 2.4$. Candidates are
168 required to fulfill either the *tracker-muon* or the *global-muon* criteria.

169 An isolation criterion is applied to remove contributions from leptons originating from QCD
170 events. Isolated muon candidates are selected if they fulfill the condition $I_{Rel}^{pf} < 0.15$, where
171 I_{Rel}^{pf} is defined as the sum of transverse energy deposits from charged and neutral hadrons
172 and photons, relative to the transverse momentum of the lepton, inside a cone in η-ϕ space of
173 $\Delta R \equiv \sqrt{(\Delta\eta)^2 + (\Delta\phi)^2} < 0.3$ around the muon. $\Delta\beta$ corrections are applied to the muons.

3.2 Electron Selection

175 Electron candidates are reconstructed using the particle-flow algorithm [20], but the four mo-
176 mentum of the electron reconstructed as Gaussian Sum Filter Electron (*gsf*) is used [19]. Elec-
177 tron candidates are also required to have a transverse energy $E_T > 20\,$GeV within a pseudora-
178 pidity $|\eta| < 2.4$. The *gsf* electron transverse impact parameter (IP) with respect to the primary
179 vertex is required to be less than 0.04 cm. The electron selection uses a multivariate analysis
180 technique (MVA). A minimum MVA value of 0.5 is required to the electron. Electrons originat-
181 ing from the conversion of photons are rejected. Furthermore, electrons are required to be iso-
182 lated by applying the cut $I_{Rel}^{pf} < 0.15$, inside a cone in η-ϕ space of $\Delta R \equiv \sqrt{(\Delta\eta)^2 + (\Delta\phi)^2} < 0.3$
183 around the electron. In addition, $\Delta\beta$ corrections are applied to the electrons.

3.3 Lepton Pair Selection

185 Events with at least two oppositely charged leptons fulfilling the above selection cuts are ac-
186 cepted. If more than two oppositely charged leptons are reconstructed in the event, the one
187 oppositely charged lepton pair with the highest sum of the transverse momenta of the two lep-
188 tons is chosen. The event is then unambiguously classified as e^+e^-, $\mu^\pm e^\mp$, or $\mu^+\mu^-$ depending
189 on the type of the selected lepton pair (i.e. an event with three leptons, e.g. μ^+, μ^-, and e^+, will
190 be assigned either to the $\mu^\pm e^\mp$ or the $\mu^+\mu^-$ channel, but not to both). The invariant mass of the
191 selected lepton pair is required to be larger than $20\,$GeV.

3.4 Jet Selection

193 The $t\bar{t}$ signal is characterised by the presence of energetic hadronic jets corresponding to b jets
194 and softer jets from initial- and final-state radiation (ISR and FSR, respectively). Most back-
195 ground events are not expected to have such hadronic activity, therefore the requirement of jets
196 in the event selection further suppresses the background contribution.

197 Jets are reconstructed using particle candidates from the particle-flow algorithm [20]. The anti-
198 k_T clustering algorithm (with clustering parameter equal to 0.5) is used for the jet identification
199 and kinematics reconstruction. The momentum of the jets is corrected by application of the
200 'L1FastJet', 'L2Relative', 'L3Absolute' and 'L2L3Residual' corrections, the last one only in data
201 while all other corrections in both data and simulation. Identification criteria (*FIRSTDATA*
202 *LOOSE* ID [21]) are applied to suppress detector noise.

203 The event selection requires the presence of at least two jets with $p_T > 30\,$GeV and within
204 $|\eta| < 2.4$.

3.5 b-Jet Selection

A b-tagging algorithm is applied to all reconstructed jets in the event. In this analysis a Combined Secondary Vertex (CSV) [22] algorithm is used. The CSV algorithm uses secondary vertices and track-based lifetime information as an input for a Multivariate Analysis (MVA) The CSV algorithm provides a likelihood-based discriminator able to distinguish between jets arising from b-quark or c- and light *l*-quarks. The BTV POG defines 3 working points for each b-tagging algorithm according the *l*-jet mistag efficiency: $\sim 10\%$, $\sim 1\%$ and $\sim 0.1\%$ for *loose* (L), *medium* (M) and *tight* (T respectively. In this analysis, a *loose* working point is selected: CSVL

Due to the differences in the data and MC b-taggging algorithms efficiencies, the BTV POG derives Data to MC correction SFs using QCD multijet events [23]. Additionally, to correct the possible difference in the b-tagging efficiency due to the different kinematics of the $t\bar{t}$ and QCD multijet events, the b-tagging efficiency (ε_{MC}) is estimated in this analysis using $t\bar{t}$ signal events. The efficiency, as a function of the jet flavour, is shown in Fig. 17.

The b-tagging status of each jet is updated according to the SF [24]. A fraction of

$$1 - SF \tag{1}$$

of originally b-tagged jets are downgraded to a non b-tag status, if the data to MC correction for jet is $SF < 1$. Instead, if the $SF \geq 1$ and the original status of the jet is non b-tagged a fraction

$$\frac{1 - SF}{1 - 1/\varepsilon_{MC}} \tag{2}$$

is upgraded to a tagged status.

After updating the status of the selected jets, according to Sec. 3.4, the event is required to have at least 1 b-tagged jet.

3.6 Missing Transverse Energy

The missing transverse energy is reconstructed as the transverse momentum imbalance of the reconstructed lepton and jets:

$$\not{E}_{x,y} = - \sum_{leptons} p_{x,y} - \sum_{jets} p_{x,y} \tag{3}$$

A Boosted Decision Tree (BDT) is used to identify jets coming from the primary vertex or from pile-up vertices [25]. The resolution of the $\not{E}_T$ variable is very sensitive to jets arising from PU vertices. The resolution of the missing transverse energy is improved by $\sim 5\%$ when using BDT classified jets in comparison to the standard particle-flow reconstruction.

Events in the dimuon and dielectron channels are required to have a missing transverse momentum $\not{E}_T > 40\,\text{GeV}$. No cut on $\not{E}_T$ is applied in the $\mu^\pm e^\mp$ channel.

3.7 Additional Requirements

In the $\mu^+\mu^-$ and e^+e^- decay channels, events are rejected if the dilepton invariant mass is within the region $76\,\text{GeV} < m^{\ell\ell} < 106\,\text{GeV}$ where background from Z^0 production is dominant.

4 Event Yields and Control Distributions

The numbers of observed events in the data compared to the expected events from the simulation are given in Table 4 after each consecutive selection step described below.

- **2 leptons:** Events with at least 2 oppositely-charged isolated leptons and $m^{\ell\ell} > 20\,\text{GeV}$, passing the trigger. The Z+jets background is removed by rejecting events in the Z^0 mass region $76\,\text{GeV} < m^{\ell\ell} < 106\,\text{GeV}$. This requirement is only applied in the $\mu^+\mu^-$ and e^+e^- channels.
- **2 jets:** Fully selected dilepton events with at least 2 jets fulfilling the jet p_T and η requirements.
- **$\not{E}_T$:** Events surviving the full selection, including the requirement on the missing energy.
- **b-tagging:** Events selected after all above cuts including b-tagging.
- **kinematic fit:** Events with physically meaningful solution for the kinematic fit.

In Table 4, $t\bar{t}$ *signal* refers to the prompt dilepton $t\bar{t}$ decays. All other $t\bar{t}$ event topologies, including dilepton decays via a τ lepton, are referred to as $t\bar{t}$ *other* and considered as background.

In the following, the distributions in data are compared to those of the simulations in the subsequent steps of the event selection described above. The shaded area corresponds to the uncertainties on the $t\bar{t}$ signal.

Figure 2 shows the invariant dilepton mass distributions. Here, only the pre-selection requiring a selected pair of leptons, is imposed. The four figures depict separately the $\mu^+\mu^-$, e^+e^-, and $\mu^\pm e^\mp$ channels and their combination (sum). In Figure 3 the number of jets is shown.

For the $\mu^+\mu^-$ and e^+e^- channels, a veto against lepton pair production via the Z^0 resonance is applied in addition, i.e. opposite sign $\mu^+\mu^-$ and e^+e^- candidates in the Z^0 mass region $76\,\text{GeV} < m^{\ell\ell} < 106\,\text{GeV}$ are rejected. Figure 4 shows the p_T of the leptons and the $\not{E}_T$ distributions for the $\mu^+\mu^-$ and e^+e^- channels. Furthermore, each event is required to contain at least two jets fulfilling the jet selection criteria.

In addition to the above selection requirements, in the $\mu^+\mu^-$ and e^+e^- channels events are rejected if their missing transverse energy $\not{E}_T$ is less than 40 GeV. For this event sample, Figures 5 and 6 show the transverse momentum p_T and pseudorapidity η distributions of the leptons. Figure 7 depicts the jet multiplicities and Figure 8 shows the distributions of the jet transverse momenta. In Figure 9 the distributions of the sum of the transverse momenta of all jets (H_T) in the event are shown. Finally, in Figure 10, the multiplicity distribution for b-tagged jets is shown after requiring at least one b-tagged jet.

In all figures starting from Figure 5, the simulated Z+jets contribution is scaled to describe the number of events in the Z^0 area (see Section 5). After the scaling the simulation is observed to provide a good description of the shape of the data and a reasonable overall normalisation, well within the normalisation uncertainties of signal and backgrounds.

5 Background determination

In the $\mu^+\mu^-$ and e^+e^- final states, the normalisation of the Z+jets background simulation is estimated from data using the method described in [26–28], extracting the events outside the Z-veto region from the events inside. As described above, events in this region have a dilepton invariant mass between 76 GeV and 106 GeV and are rejected for the $t\bar{t}$ analysis. Since con-

Table 4: Number of expected signal and background events, compared to the event yields in the 19.7 fb^{-1} data, after each selection step.

$\mu^+\mu^-$ sample	2 leptons	2 jets	$\not{E}_T$	b-tag	kin. fit
$t\bar{t}$ signal	21212.4	16368.3	12425.9	11608.8	10901
$t\bar{t}$ other	3481.2	2667.9	2052.2	1902.7	1808.2
$t\bar{t} + Z/W/\gamma$	271.0	241.3	191.0	175.7	153.4
tW	2355.2	931.1	698.7	621.4	470.8
diboson	6577.1	786.0	235.2	88.5	54.0
W	112.9	60.5	30.8	7.2	7.2
DY$\rightarrow \tau\tau$	19955.2	1068.6	453.2	157.2	101.8
DY$\rightarrow \ell^+\ell^-$	725916	33432.7	1979.0	744.6	471.3
QCD	2032.4	386.9	0	0	0
Sum MC	781914	55943.2	18066	15306.2	13967.7
Data	849712	60902	18826	15807	14403

$\mu^\pm e^\mp$ sample	2 leptons	2 jets	$\not{E}_T$	b-tag	kin. fit
$t\bar{t}$ signal	46339.9	35805.6	35805.6	33488.7	31602.2
$t\bar{t}$ other	7887.4	6070.8	6070.8	5637.4	5375.1
$t\bar{t} + Z/W/\gamma$	556.1	495.4	495.4	455.8	408.4
tW	5182.9	2031.2	2031.2	1789.3	1374.9
diboson	11255.8	630.4	630.4	223.2	153.5
W	1511.7	190.5	190.5	104.0	86.3
DY$\rightarrow \tau\tau$	33312.9	1732.9	1732.9	632.5	483.1
DY$\rightarrow \ell^+\ell^-$	1239.1	88.6	88.8	35.9	22.9
QCD	2824.8	246.2	246.2	246.1	244.2
Sum MC	110111	47291.7	47291.6	42613	39750.6
Data	111655	47208	47208	42440	39640

e^+e^- sample	2 leptons	2 jets	$\not{E}_T$	b-tag	kin. fit
$t\bar{t}$ signal	16739.9	12885.4	9781.7	9132.4	8507.5
$t\bar{t}$ other	2747.7	2122.6	1641.8	1521.4	1431.5
$t\bar{t} + Z/W/\gamma$	214.0	191.0	151.0	137.9	120.3
tW	1859.4	758.8	563.6	490.5	356.8
diboson	4948.9	597.2	180.9	66.1	40.2
W	1028.2	133.0	56.8	27.5	27.1
DY$\rightarrow \tau\tau$	13439.5	780.1	357.4	131.2	111.4
DY$\rightarrow \ell^+\ell^-$	509839	23785.4	1378.2	475.8	296.7
QCD	254.2	129.3	129.3	129.3	127.7
Sum MC	551071	41382.8	14240.7	12112.1	11019.2
Data	567736	43519	13999	11767	10678

| *combined* sample	2 leptons	2 jets	$\not{E}_T$	b-tag	kin. fit
$t\bar{t}$ signal	84292.2	65059.3	58013.2	54229.8	51010.6
$t\bar{t}$ other	14116.3	10861.3	9764.8	9061.5	8614.8
$t\bar{t} + Z/W/\gamma$	1041.1	927.6	837.3	769.4	682.2
tW	9397.5	3721.2	3293.6	2901.3	2202.6
diboson	22781.9	2013.6	1046.5	377.8	247.7
W	2652.7	384.0	278.2	138.7	120.7
DY$\rightarrow \tau\tau$	66707.6	3581.6	2543.5	920.9	696.4
DY$\rightarrow \ell^+\ell^-$	1236990.0	57306.7	3417.9	1246.9	784.6
QCD	5111.4	762.3	375.5	375.5	371.9
Sum MC	1443100.0	144618	79570.4	70021.8	64731.4
Data	1529100.0	151629	80033	70014	64721
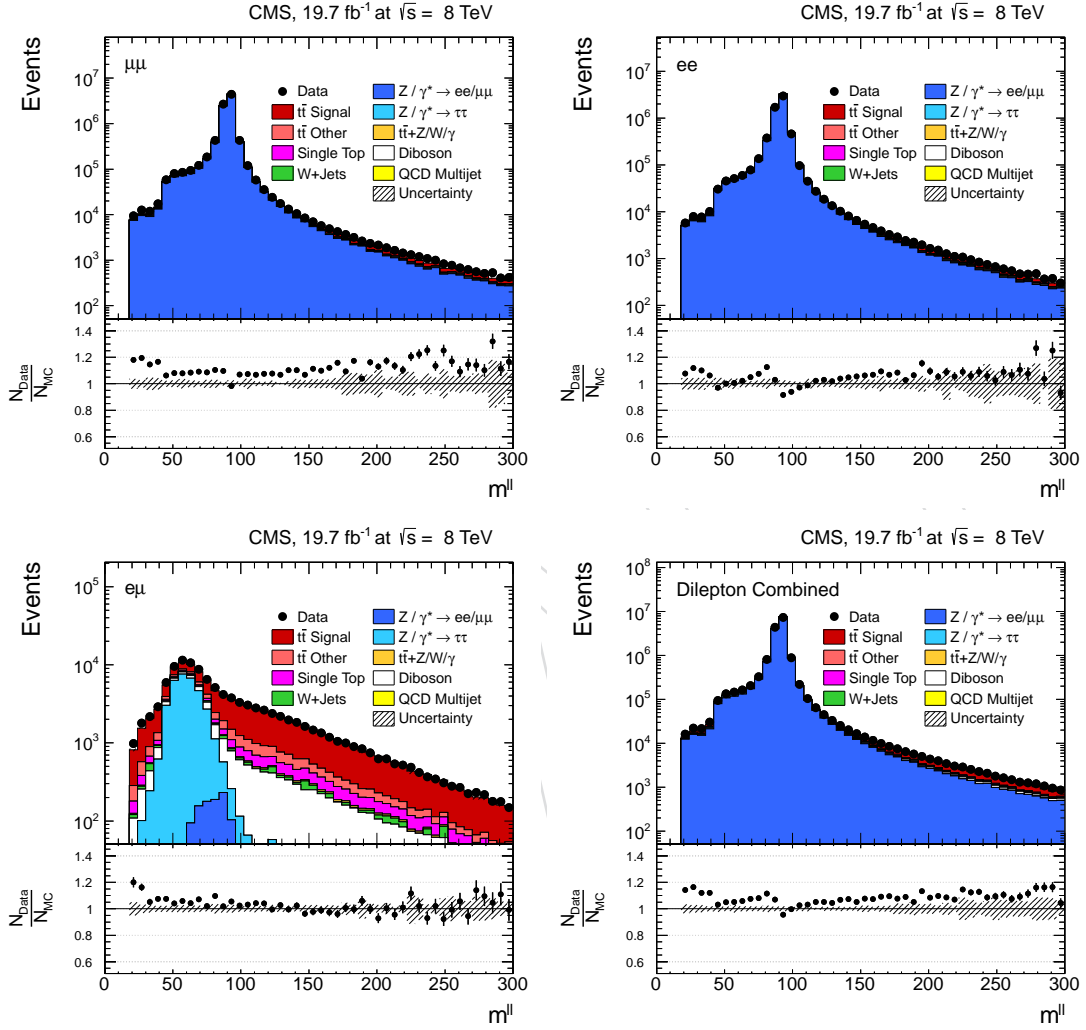
Figure 2: Opposite-charge dilepton invariant mass for the $\mu^+\mu^-$, e^+e^-, and $\mu^\pm e^\mp$ samples after selection of two isolated leptons. The simulated samples are normalised to an integrated luminosity of 19.7 fb^{-1}. Scale factors for trigger and lepton selection presented in Sections 7.1 and 7.2, respectively, are used. At this analysis step, no Z/γ^*+jets scaling is applied yet. The lower right figure shows the combination (sum) of the three channels. The shaded area indicates the uncertainties on the $t\bar{t}$ signal.
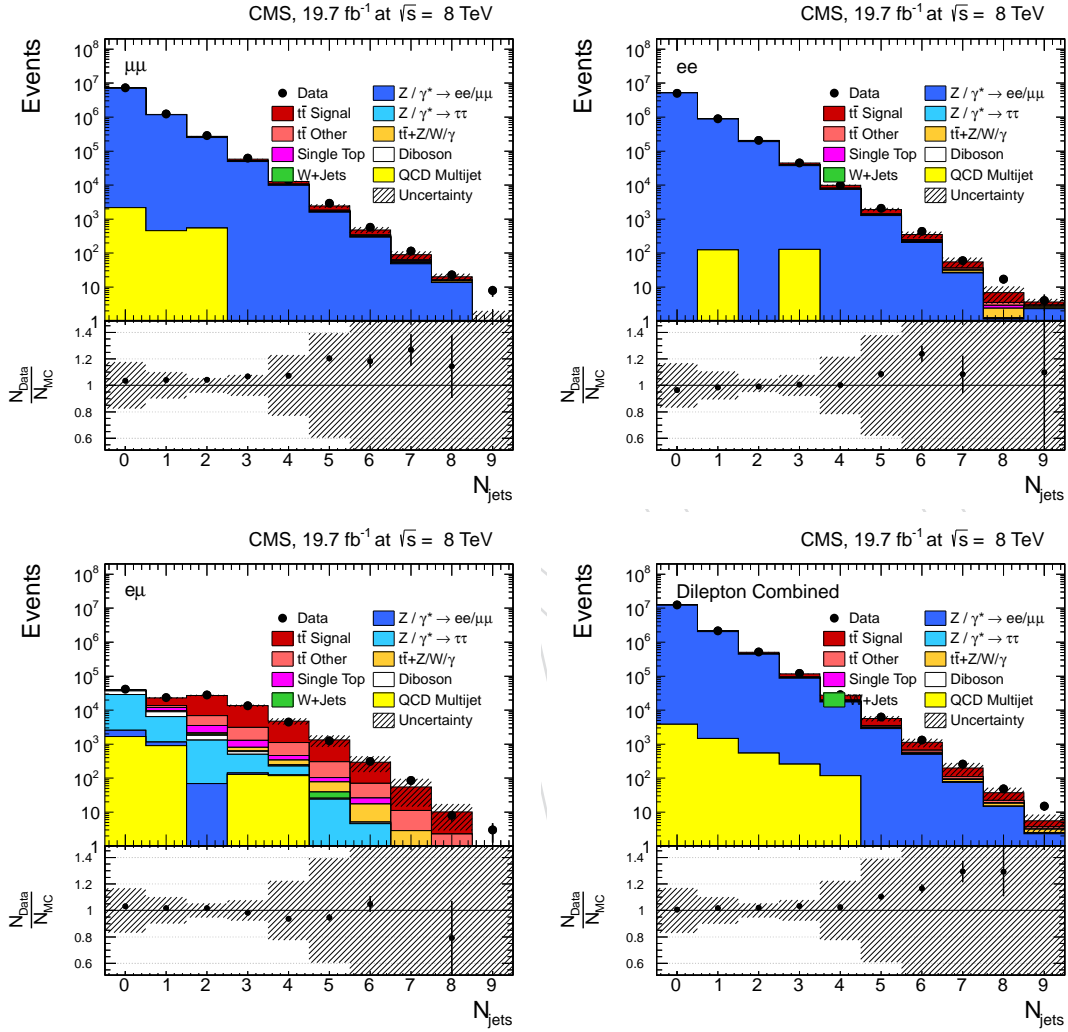
Figure 3: Number of jets for the dilepton samples in the $\mu^+\mu^-$, e^+e^- and $\mu^\pm e^\mp$. The simulated samples are normalised to an integrated luminosity of $19.7\,\text{fb}^{-1}$. Scale factors for trigger and lepton selection presented in Sections 7.1 and 7.2, respectively, are used. At this analysis step, no Z/γ^*+jets scaling is applied yet. The lower right figure shows the combination (sum) of the three channels. The shaded area indicates the uncertainties on the $t\bar{t}$ signal.
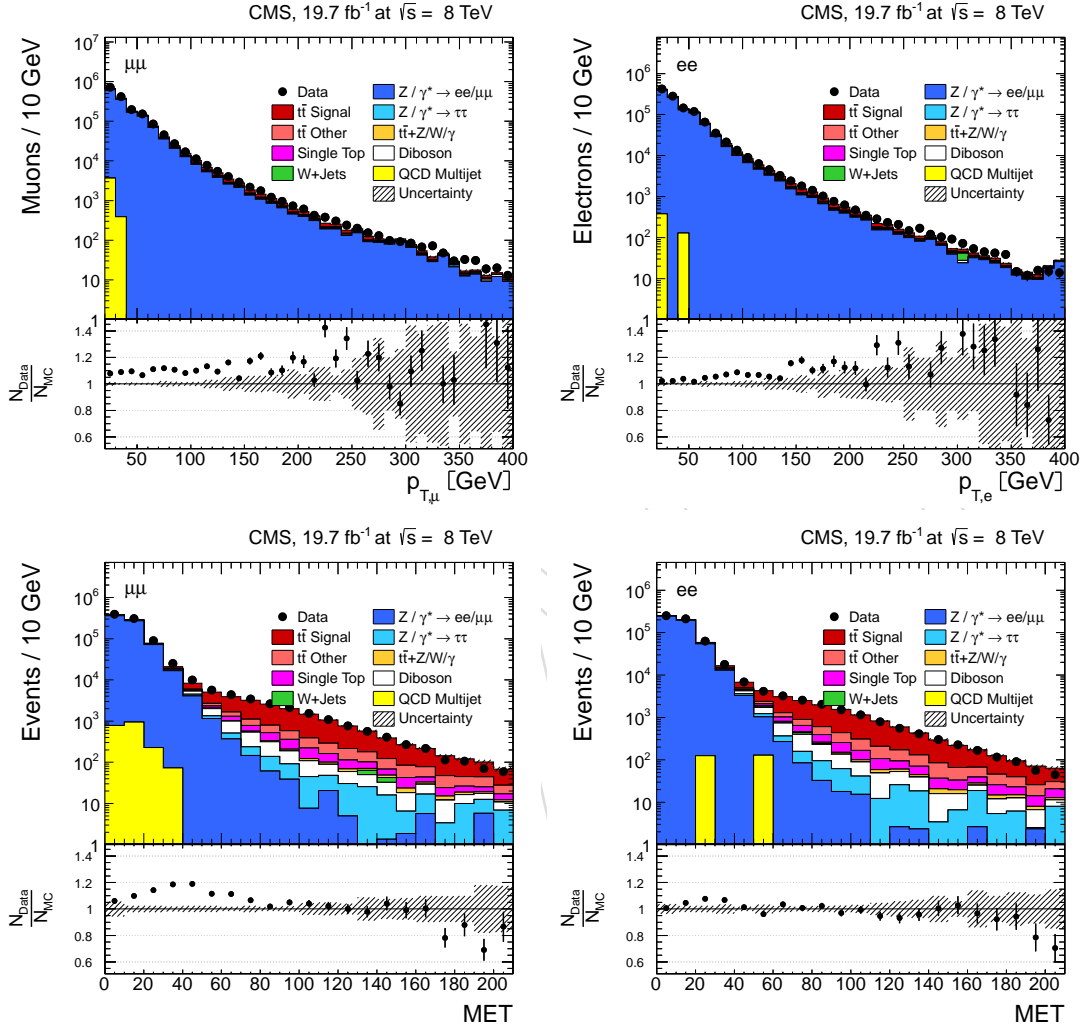
Figure 4: Transverse momentum p_T of isolated lepton candidates (top row) and missing transverse energy spectra (bottom row) for the $\mu^+\mu^-$ and e^+e^- channels with $m^{\ell\ell} < 76$ GeV or $m^{\ell\ell} > 106$ GeV. The simulated samples are normalised to an integrated luminosity of $19.7\,\mathrm{fb}^{-1}$. Scale factors for trigger and lepton selection presented in Sections 7.1 and 7.2, respectively, are used. At this analysis step no Z/γ^*+jets scaling is applied yet. The shaded area indicates the uncertainties on the $t\bar{t}$ signal.
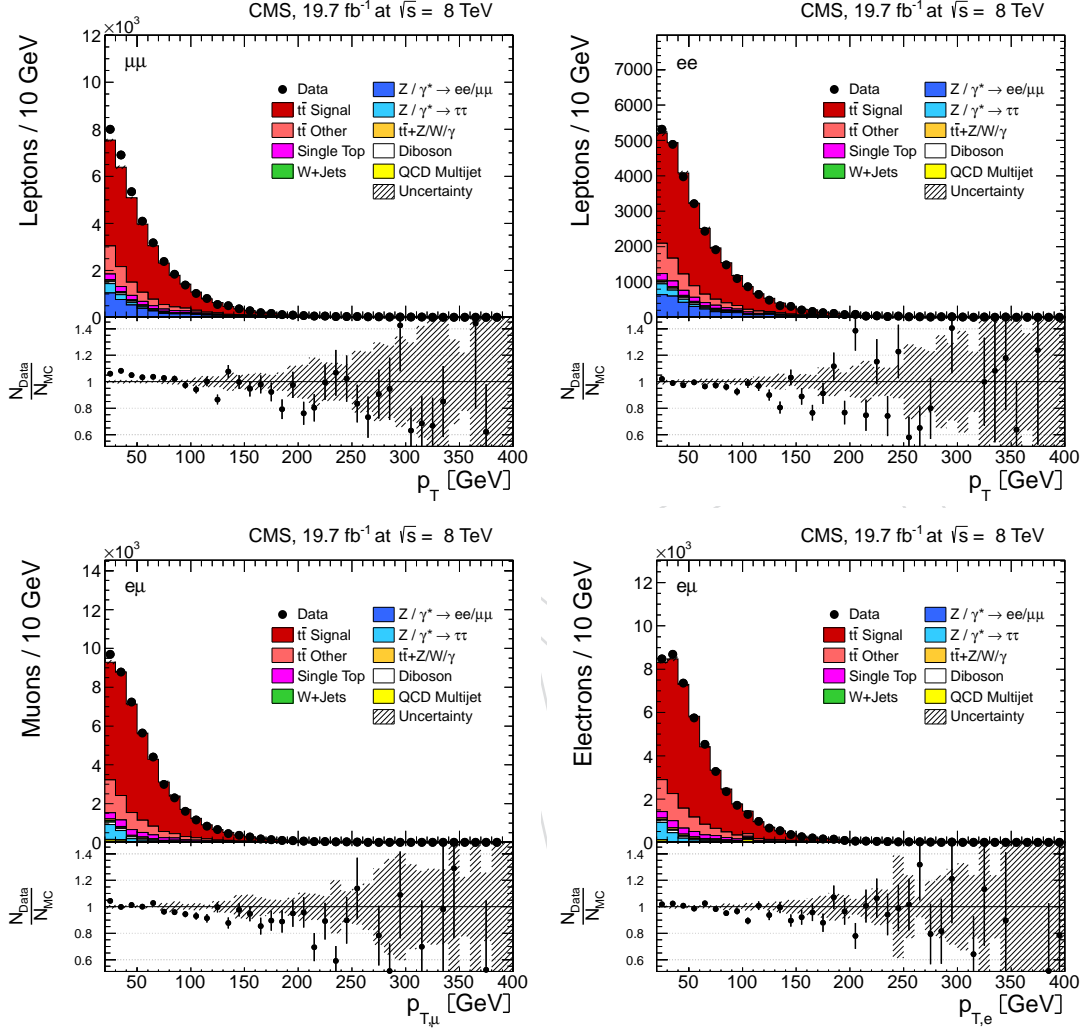
Figure 5: Transverse momentum p_T distributions of isolated muon (left figures) and electron (right figures) candidates for the $\mu^+\mu^-$, e^+e^- (top row) and $\mu^\pm e^\mp$ (bottom row) samples. For the $\mu^+\mu^-$ and e^+e^- channels, the events with $76 < m^{\ell\ell} < 106$ GeV or $\not{E}_T < 40$ GeV are rejected. The simulated samples are normalised to an integrated luminosity of $19.7\,\text{fb}^{-1}$. Scale factors for trigger selection presented in Section 7.1 are used. For the $\mu^+\mu^-$ and e^+e^- channels, the Z/γ^*+jets sample (blue area) is scaled to describe the number of events in the Z^0 area (see Section 5). The shaded area indicates the uncertainties on the $t\bar{t}$ signal.
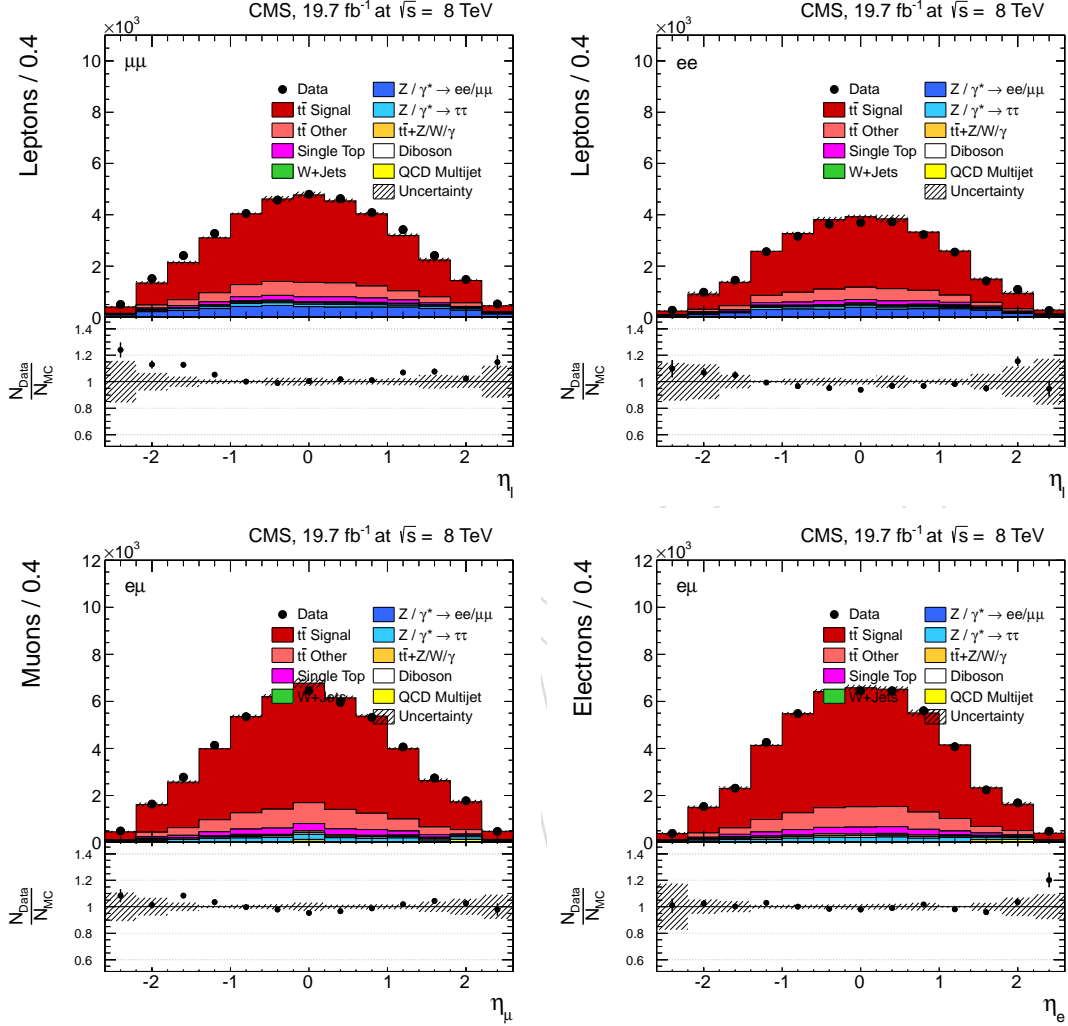
Figure 6: pseudorapidity η distributions of isolated muon (left figures) and electron (right figures) candidates for the $\mu^+\mu^-$, e^+e^- (top row) and $\mu^\pm e^\mp$ (bottom row) samples. For the $\mu^+\mu^-$ and e^+e^- channels, the events with $76 < m^{\ell\ell} < 106$ GeV or $\not{E}_T < 40$ GeV are rejected. The simulated samples are normalised to an integrated luminosity of 19.7 fb^{-1}. Scale factors for trigger and lepton selection presented in Sections 7.1 and 7.2, respectively, are used. For the $\mu^+\mu^-$ and e^+e^- channels, the Z/γ^*+jets sample (blue area) is scaled to describe the number of events in the Z^0 area (see Section 5). The shaded area indicates the uncertainties on the $t\bar{t}$ signal.
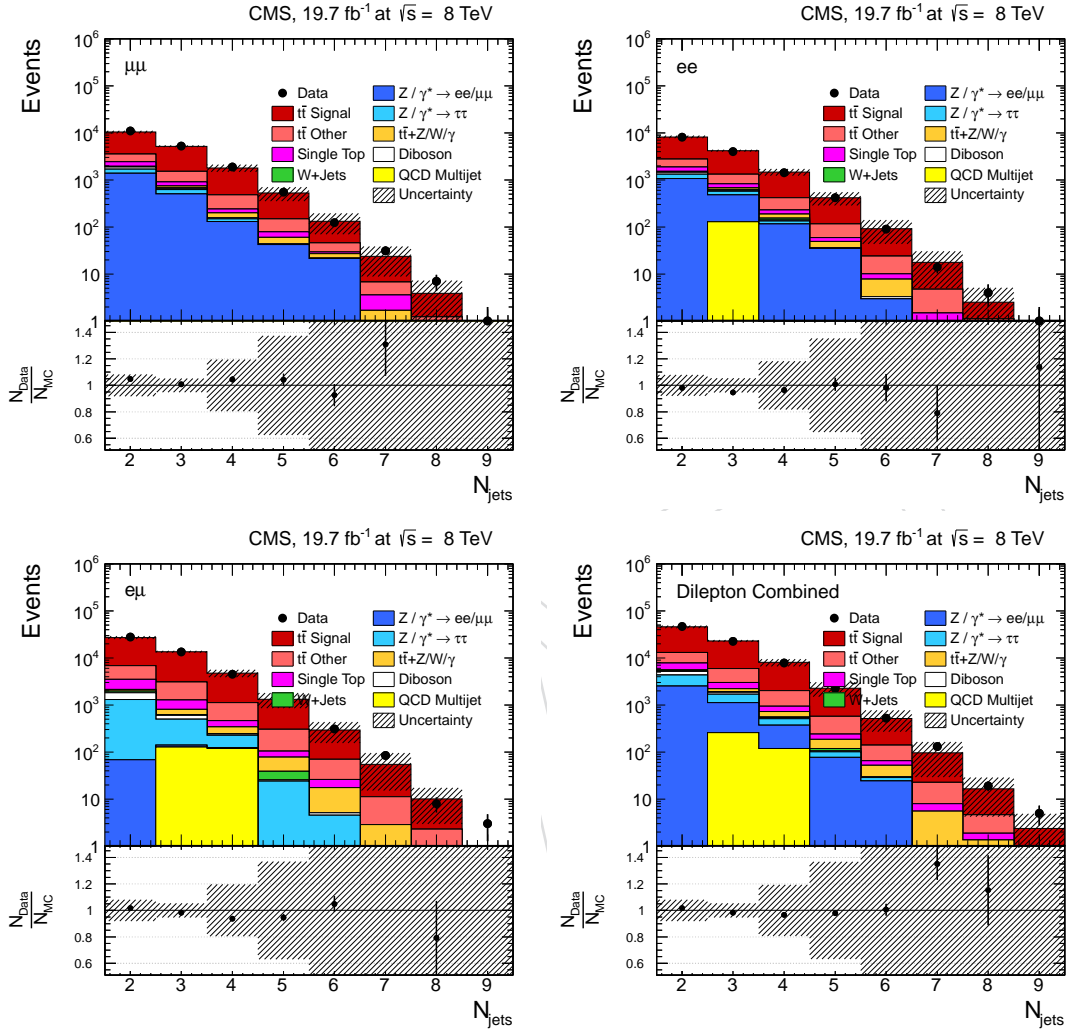
Figure 7: Multiplicity of jets for the $\mu^+\mu^-$, e^+e^- and $\mu^\pm e^\mp$ isolated dilepton dijet samples. For the $\mu^+\mu^-$ and e^+e^- channels, the events with $76 < m^{\ell\ell} < 106$ GeV or $\not{E}_T < 40$ GeV are rejected. The simulated samples are normalised to an integrated luminosity of $19.7\,\text{fb}^{-1}$. Scale factors for trigger and lepton selection presented in Sections 7.1 and 7.2, respectively, are used. For the $\mu^+\mu^-$ and e^+e^- channels the Z/γ^*+jets sample (blue area) is scaled to describe the number of events in the Z^0 area (see Section 5). The lower right plot shows the combination (sum) of the three channels. The shaded area indicates the uncertainties on the $t\bar{t}$ signal.

Figure 8: Transverse momentum p_T of jets for the $\mu^+\mu^-$, e^+e^- and $\mu^\pm e^\mp$ isolated dilepton dijet samples. For the $\mu^+\mu^-$ and e^+e^- channels, the events with $76 < m^{\ell\ell} < 106$ GeV or $\not{E}_T < 40$ GeV are rejected. The simulated samples are normalised to an integrated luminosity of $19.7\,\text{fb}^{-1}$. Scale factors for trigger and lepton selection presented in Sections 7.1 and 7.2, respectively, are used. For the $\mu^+\mu^-$ and e^+e^- channels the Z/γ^*+jets sample (blue area) is scaled to describe the number of events in the Z^0 area (see Section 5). The lower right plot shows the combination (sum) of the three channels. The shaded area indicates the uncertainties on the $t\bar{t}$ signal.
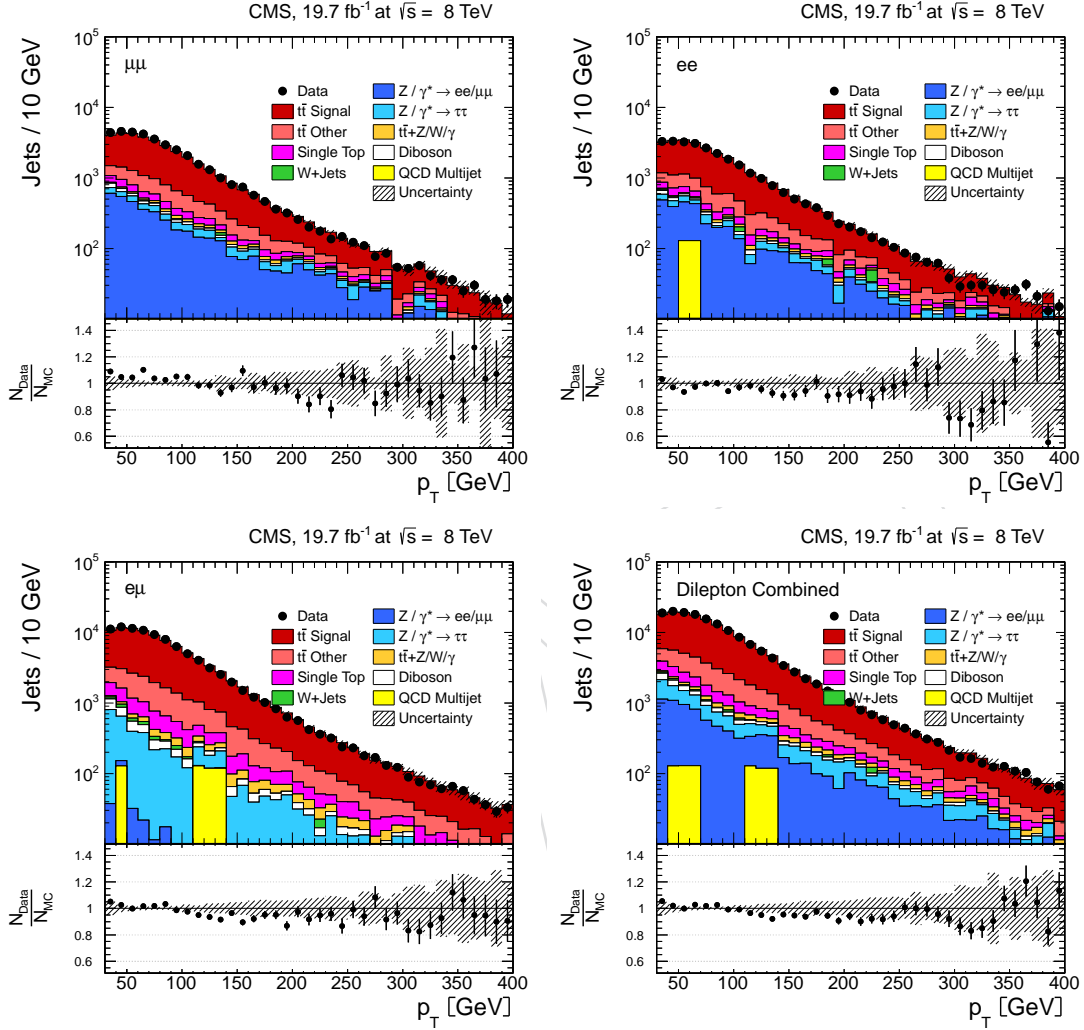
Figure 9: Scalar sum of jet transverse energies H_T for the $\mu^+\mu^-$, e^+e^- and $\mu^\pm e^\mp$ isolated dilepton dijet samples. For the $\mu^+\mu^-$ and e^+e^- channels, the events with $76 < m^{\ell\ell} < 106$ GeV or $\not{E}_T < 40$ GeV are rejected. The simulated samples are normalised to an integrated luminosity of $19.7\,\text{fb}^{-1}$. Scale factors for trigger and lepton selection presented in Sections 7.1 and 7.2, respectively, are used. For the $\mu^+\mu^-$ and e^+e^- channels the Z/γ^*+jets sample (blue area) is scaled to describe the number of events in the Z^0 area (see Section 5). The lower right plot shows the combination (sum) of the three channels. The shaded area indicates the uncertainties on the $t\bar{t}$ signal.
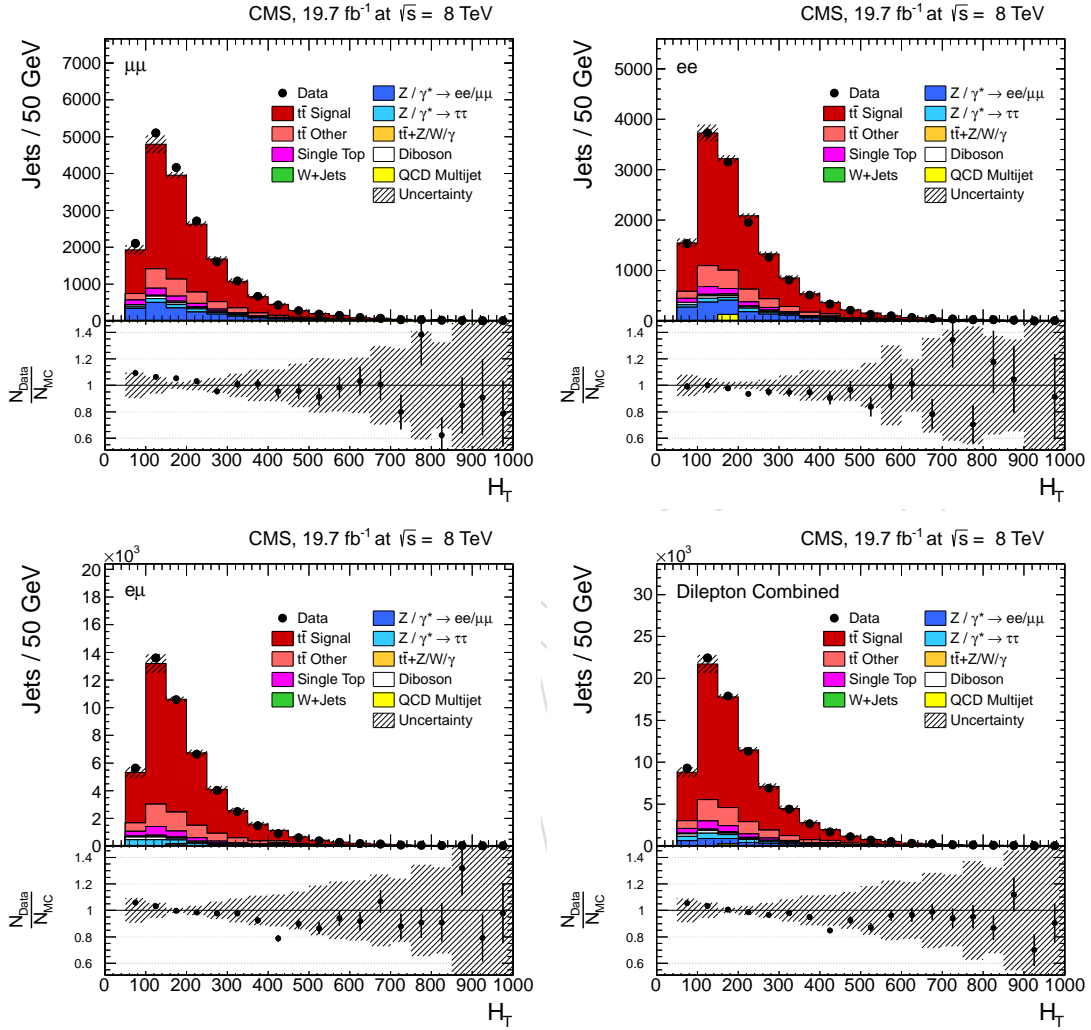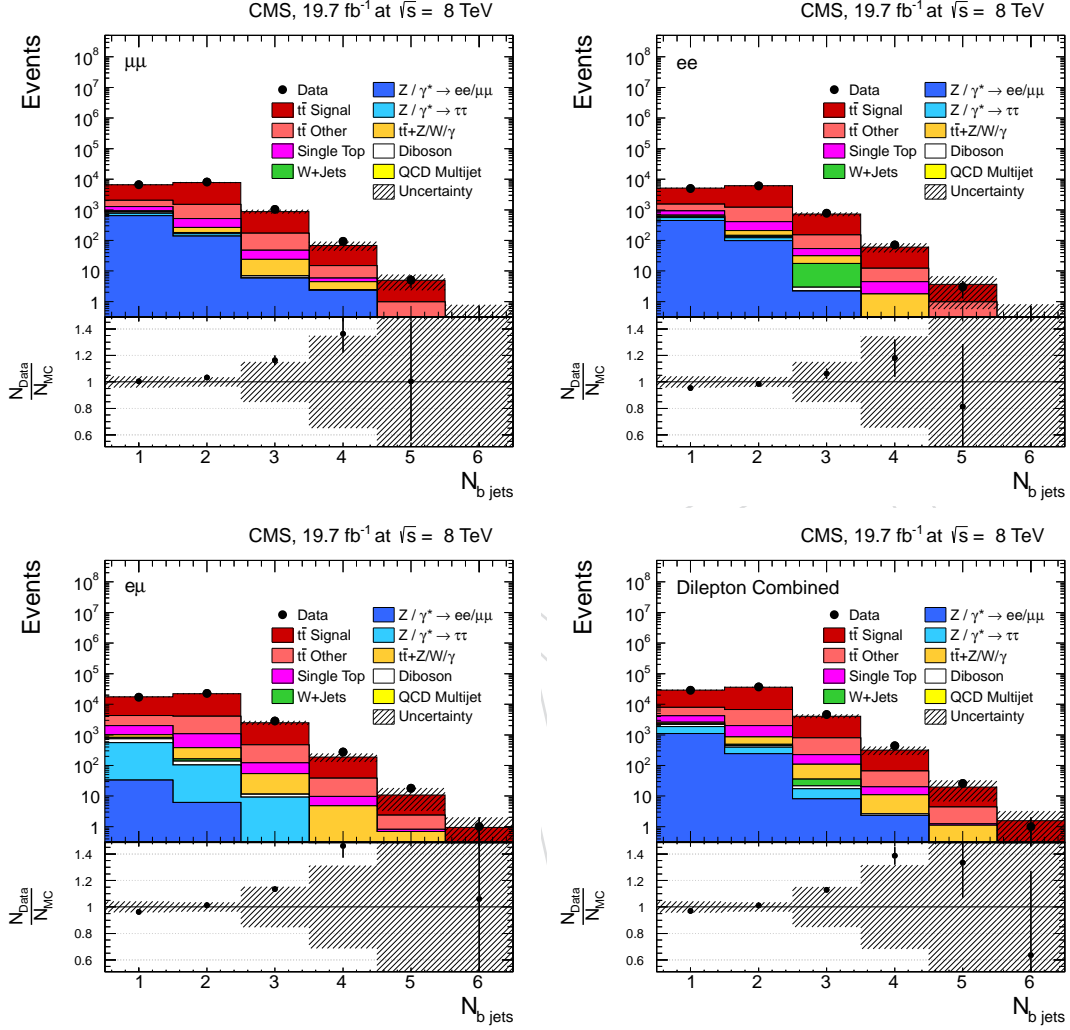
Figure 10: Number of b-tagged jets (CSVL) for the $\mu^+\mu^-$, e^+e^- and $\mu^\pm e^\mp$ isolated dilepton dijet samples after requiring at least one b-tagged jet. For the $\mu^+\mu^-$ and e^+e^- channels, the events with $76 < m^{\ell\ell} < 106$ GeV or $\not{E}_T < 40$ GeV are rejected. The simulated samples are normalised to an integrated luminosity of 19.7 fb^{-1}. Scale factors for trigger, lepton selection and b-tagging presented in Sections 7.1, 7.2, and 7.3 respectively, are used. For the $\mu^+\mu^-$ and e^+e^- channels the Z/γ^*+jets sample (blue area) is scaled to describe the number of events in the Z^0 area (see Section 5). The lower right plot shows the combination of the three channels. The shaded area indicates the uncertainties on the $t\bar{t}$ signal.

276 tamination from non–Z+jets background contributions can still be present in the Z-veto region,
277 this contribution is subtracted from the $\mu^\pm e^\mp$ channel and then scaled according to the event
278 yields in the e^+e^- and $\mu^+\mu^-$ channels.

279 The expected number of events outside the Z-veto can be measured from data as:

$$N_{out}^{l^+l^-,obs} = R_{out/in}^{l^+l^-}(N_{in}^{l^+l^-} - 0.5N_{in}^{e\mu}k_{ll}) \tag{4}$$

where $ll = \mu^+\mu^-$ or e^+e^- and $R_{out/in}$ is the ratio of the number of events outside/inside the
Z-veto region taken from the Z+jets simulated sample:

$$R_{out/in} = \frac{N_{Z+jetsMC}^{out}}{N_{Z+jetsMC}^{in}}.$$

Here, k_{ll} is a correction factor that takes into account the differences between electron and muon
reconstruction. This correction can be determined from the number of e^+e^- and $\mu^+\mu^-$ events
in the Z peak region before applying the $\not{E}_T$ requirement (labelled as *loose*). Since $N^{e^+e^-_{in,loose}}$ and
$N^{\mu^+\mu^-_{in,loose}}$ are proportional to the square of the corresponding single-lepton candidate selection
efficiencies, the correction factor can be expressed as:

$$k_{ee} = \sqrt{\frac{N^{e^+e^-_{in,loose}}}{N^{\mu^+\mu^-_{in,loose}}}}$$

$$k_{\mu\mu} = \sqrt{\frac{N^{\mu^+\mu^-_{in,loose}}}{N^{e^+e^-_{in,loose}}}}$$

280 A value of $k_{ll} = 1.18$ (0.85) is found for $\mu^+\mu^-$ (e^+e^-) events with a negligible uncertainty. The
281 global scaling factors $\mathcal{C}_{Z+jets} = Z + jets_{data}/Z + jets_{MC}$ are determined such that the integral of
282 the simulated events in the peak region is identical to that of the data. The Drell-Yan normal-
283 ization scale factor in the $\mu^\pm e^\mp$ channel is derived following the same prescription as in [29]:
284 $SF(\mu e) = \sqrt{SF(ee) \times SF(\mu\mu)}$. The results and scaling factors are summarized in Table 5.

285 The remaining background contributions, such as QCD-multijet events or backgrounds orig-
286 inating from diboson processes as well as single-top (tW) and $t\bar{t} + Z/W/\gamma$ production are
287 estimated from the simulation.

Table 5: Data-driven Z+jets background estimation in the $\mu^+\mu^-$ and e^+e^- channels after the missing
transverse energy requirement.

	$\mu^+\mu^-$	e^+e^-	$\mu^\pm e^\mp$
Z+jets MC	597.80	450.65	-
Estimate from data	568.02	394.05	-
$R_{out/in}$	0.169	0.158	-
$\mathcal{C}_{Z+jets}$	0.95	0.87	0.91

288 In Figure 11 the Z+jets distributions for the $\mu^+\mu^-$ and e^+e^- channels are shown after applica-
289 tion of the global scaling factors $\mathcal{C}_{Z+jets}$ of 0.95 in $\mu^+\mu^-$, 0.87 in e^+e^- and 0.91 for $\mu^\pm e^\mp$. The
290 same scaling factors are applied to the Z+jets background simulation of the final event sample,
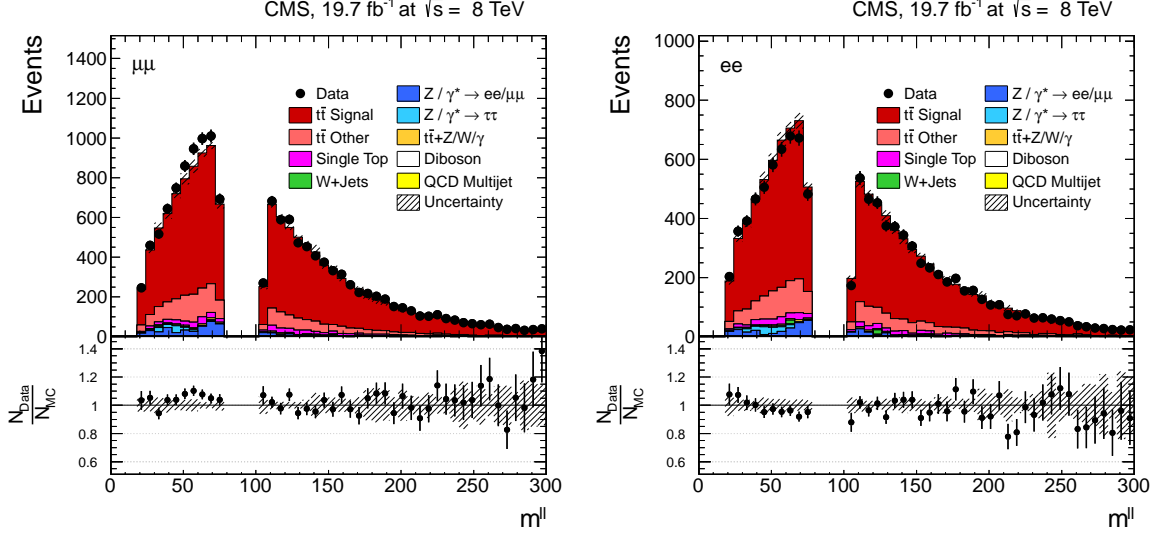291 outside the veto region.

Figure 11: The Z+jets sample (blue area), for the $\mu^+\mu^-$ and e^+e^- channel, after all selection cuts, including $\not{E}_T > 40\,\text{GeV}$. The simulations of Z+jets are scaled by 0.95 for $\mu^+\mu^-$, 0.87 for e^+e^- and 0.91 for $\mu^{\pm}e^{\mp}$. The shaded area indicates the uncertainties on the $t\bar{t}$ signal.

5.1 Recoil Correction of Drell-Yan Events

Z-recoil corrections are determined in [30] and applied to simulated $Z/\gamma^* \to ll$ in order to correct for residual differences in $\not{E}_T$ response and resolution between data and simulation [25]. The correction to the transverse component of the hadronic recoil, $u_\perp$, follows the next steps:

- For a given hadronic recoil transverse component value of the DY Monte–Carlo event, $u_\perp$, estimate the integral value of the Monte-Carlo fit f_{MC} function up–to the measured value: $I = \int_{-\infty}^{u_\perp^{MC}} f_{MC}$

- Derive the corresponding $u_\perp^{corr}$ such that the integral of the data fit f_{data} up to the corrected recoil value is the same as the integral on the MC fit: $u_\perp^{corr\cdot} = f_{data}^{-1}(I)$

The same method applies to the parallel component $u_\parallel$.

The $\not{E}_T$ is recalculated from the corrected hadronic recoil and the leptons arising from the Z-boson. The effect of the recoil correction is shown in Fig. 12, where the $\not{E}_T$ distribution before and after applying the recoil correction is presented.
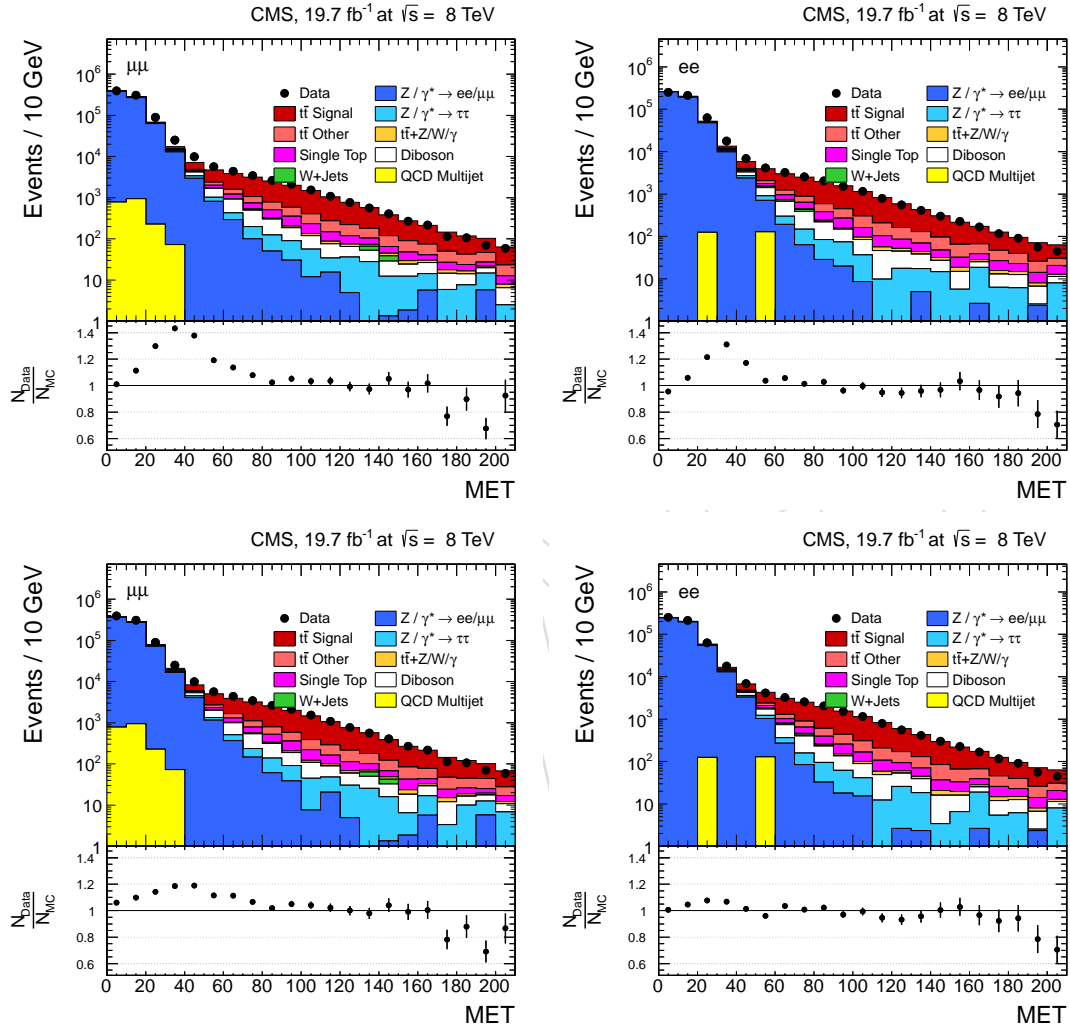
Figure 12: Missing transverse energy distribution in the $\mu^+\mu^-$ (left) and e^+e^- (right) channels. The MET distribution is shown after two lepton and QCD- and Z-veto event selection. The MET is shown before (top row) and after (bottom row) applying the hadronic recoil correction.

6 Reconstruction of the Top-Quark Kinematics

For each event the kinematics of the top and of the anti-top quark is fully reconstructed. A new reconstruction method is used. The main differences compared to the previous method [11, 31] are:

- the top quark mass is constraint to a nominal value of 172.5 GeV;
- different kinematic weights are used to resolve solution ambiguities and at the same time keeping kinematic biases at a minimal level;
- the reconstruction efficiency is increased by reconstructing each event several times with randomly smearing measured objects according to their detector resolutions.

In the latter two aspects the new method is similar to the AMWT reconstruction technique described in [4] and [5]. In the following a detailed account of the new method is given.

An algebraic method [32] is used, applying six kinematic constraints, to determine the only unknowns of the event, the momentum vectors of the two undetected neutrinos. An event may contain more than two b-jet candidates and for each pair of such jets there are two possible assignments of the two jets to the two selected leptons. The constraints and following steps are tried out separately for each suitable jet pair and separately for the two lepton–jet assignments. Jets are only considered if they fulfill the general jet selection requirements defined in Section 3.4 and at least one of the two jets has to be b-tagged (see Section 3.4).

The constraint equations are constructed using the four momenta of the two leptons, of the two jets and the missing transverse energy. Assuming that the missing transverse energy is entirely caused by the two neutrinos leads to

$$
\begin{aligned}
\not{E}_x &= p_{x,\nu} + p_{x,\bar{\nu}} \\
\not{E}_y &= p_{y,\nu} + p_{y,\bar{\nu}}
\end{aligned}
\tag{5}
$$

which eliminates two missing variables. Assuming that the lepton and the neutrino from the same top branch have an invariant mass equal to the W mass of 80.4 GeV provides two further constraints:

$$
\begin{aligned}
m_{W^+}^2 &= (E_{\ell^+} + E_\nu)^2 - (p_{x,\ell^+} + p_{x,\nu})^2 \\
&\quad - (p_{y,\ell^+} + p_{y,\nu})^2 - (p_{z,\ell^+} + p_{z,\nu})^2
\end{aligned}
\tag{6}
$$

$$
\begin{aligned}
m_{W^-}^2 &= (E_{\ell^-} + E_{\bar{\nu}})^2 - (p_{x,\ell^-} + p_{x,\bar{\nu}})^2 \\
&\quad - (p_{y,\ell^-} + p_{y,\bar{\nu}})^2 - (p_{z,\ell^-} + p_{z,\bar{\nu}})^2
\end{aligned}
\tag{7}
$$

Finally, two additional constraints are obtained by requiring the reconstructed top and anti-top quark masses to be equal to 172.5 GeV.

$$
\begin{aligned}
m_t^2 &= (E_{\ell^+} + E_\nu + E_b)^2 - (p_{x,\ell^+} + p_{x,\nu} + p_{x,b})^2 \\
&\quad - (p_{y,\ell^+} + p_{y,\nu} + p_{y,b})^2 - (p_{z,\ell^+} + p_{z,\nu} + p_{z,b})^2
\end{aligned}
\tag{8}
$$

$$
\begin{aligned}
m_{\bar{t}}^2 &= (E_{\ell^-} + E_{\bar{\nu}} + E_{\bar{b}})^2 - (p_{x,\ell^-} + p_{x,\bar{\nu}} + p_{x,\bar{b}})^2 \\
&\quad - (p_{y,\ell^-} + p_{y,\bar{\nu}} + p_{y,\bar{b}})^2 - (p_{z,\ell^-} + p_{z,\bar{\nu}} + p_{z,\bar{b}})^2
\end{aligned}
\tag{9}
$$

Some simplifying assumptions are used for the further evaluation: the masses of leptons and neutrinos are neglected and the masses of the b-jets are set to the b-quark mass used in the simulation.

The system of equations (5) to (9) can be transformed into a single equation which is a 4th order polynomial in one of the neutrino momentum components and can be written as

$$0 = \sum_{i=0}^{4} c_i(m_t, p_{\ell^+}, p_{\ell^-}, p_b, p_{\bar{b}}) \, p_{\text{x}}(\bar{\nu})^i \tag{10}$$

334 where, without loss of generality, $p_{\text{x}}(\bar{\nu})$ has been chosen as the variable. The coefficients of this
335 equation depend on the four momenta of the observable particles. The equation can be solved
336 analytically with a maximum four-fold ambiguity.

337 For a seizable fraction of events the Equation (10) is not solvable for the measured values of
338 particle momenta and missing energy.

339 This is caused by measurement fluctuations leading the equation into the unphysical region.

340 In order not to loose such events, each event is reconstructed 100 times, each time smearing
341 relevant observables randomly according to their resolutions.

342 In this analysis the energies and directions of the two jets and the two leptons are smeared.

343 The smearing factors are determined from the signal MC simulation for reconstructed b-jets
344 and leptons matched to the true b-quarks and leptons from top decays.

345 The smearing of energies is implemented as a correction factor for the reconstructed energy
346 sampled randomly from the MC distribution of the ratio of the true energy on particle level
347 divided by the reconstructed energy.

348 The shape of these distributions is found to be largely independent on the true energy; thus the
349 distribution obtained in the complete kinematic region of the analysis is used for the sampling.
350 The corresponding distributions for b-jets and leptons are shown in Figure 13.

351 For the directions, a random gaussian smearing is applied in a random direction around the
352 nominal direction. According to the MC simulation the angular resolutions depend only weakly
353 on the b-jet or lepton kinematics and thus the average resolutions were taken for the gaussian
354 smearing. Figure 14 shows the distributions from which the average resolutions were obtained.
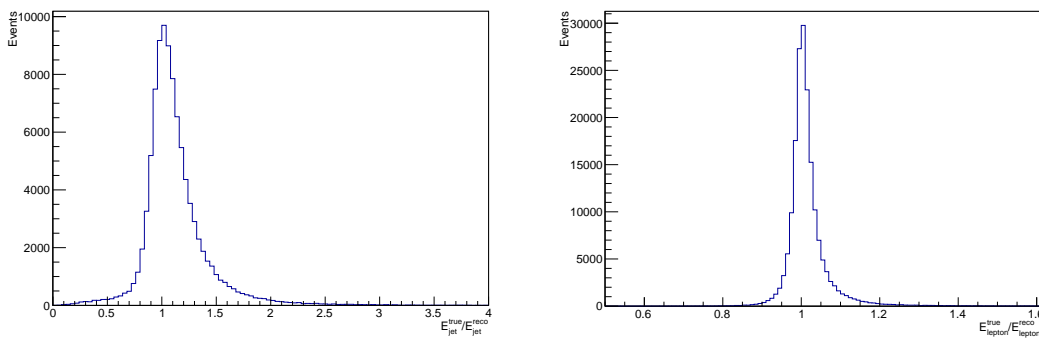

Figure 13: Distributions of the energy correction factors used for the energy smearing in the kinematic reconstruction of the top-quark kinematics. The factors are shown (left) for the b-quarks and (right) for the leptons.

355

356 One additional smearing is applied: the values of the W masses that were used in the constraint
357 Eq. (6) and (7) are randomly sampled from a relativistic Breit-Wigner distribution, estimated
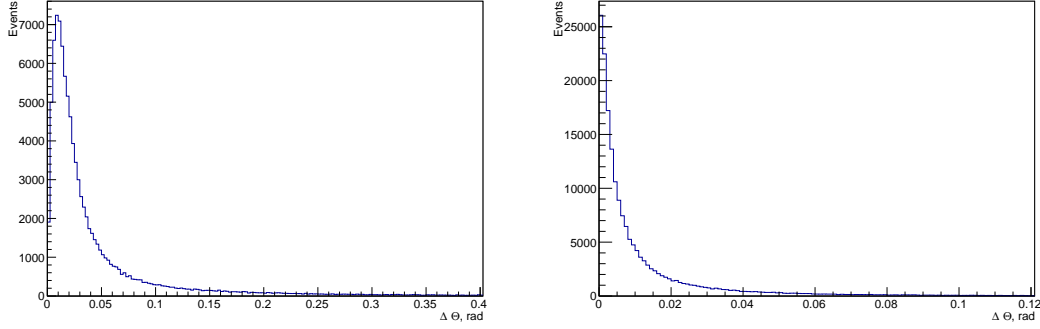358 from the generator W mass distribution of the signal MC.

Figure 14: Distributions of the angle between the particle level direction and the detector level direction (left) for jets and (right) for leptons.

For a given event smearing the solution of Eq. (10) is chosen (from the up to four solutions) which yields the minimum invariant mass of the top-quark-pair. This selection was introduced in [33], where it was shown to deliver for the correct jets and lepton–jet assignment in most cases the correct solution. For each solution a weight is calculated as $w = w_{m^{\bar{l}b}} \cdot w_{m^{l\bar{b}}}$, where $m^{\bar{l}b}$ and $m^{l\bar{b}}$ are the reconstructed (including the smearing) invariant masses of the lepton-jet pairs from the top and the anti-top decays, respectively. The weights $w_{m^{\bar{l}b}}$ are $w_{m^{l\bar{b}}}$ are calculated according to the expected (true) lepton-b-jet mass distribution in top decays after the kinematic selection cuts, estimated from the signal MC at particle level. The three momentum vector of the top quark is determined as a weighted average $\langle \vec{p}_t \rangle$ of all smeared solutions:

$$\langle \vec{p}_t \rangle = \frac{1}{w_s} \sum_{i=1}^{100} w_i \vec{p}_{t,i}, \quad \text{with} \quad w_s = \sum_{i=1}^{100} w_i. \tag{11}$$

Here w_i denotes the weight and $\vec{p}_{t,i}$ the reconstructed top quark three momentum obtained for the i-th smearing of the event[1]. The four momentum vector of the top quark is completed by its energy which is calculated from $\langle \vec{p}_t \rangle$ and constraining the top-quark mass to the nominal value of the MC simulation, 172.5 GeV. The kinematics of the anti-top quark is analogously determined.

The kinematic reconstruction outlined above is tried for all suitable pairs of b-jet candidates in the event, separately for the two lepton–jet assignments. If two or more jets are classified as b-tagged, then these jets are tried first; only if no kinematic solution is found at all then also combinations with one b-tagged and one untagged jet are considered. Finally, the jet pair and lepton–jet assignment (and resulting top and anti-top quark kinematics) is chosen which yields the maximum w_s.

All top-quark-pair related kinematic observables are directly determined from the reconstructed four momentum vectors of the top and the anti-top quark. For differential cross-sections as function of the lepton and b-jets kinematics the measured momenta (without smearing) of these particles are used.

In the kinematic reconstruction applied in [11, 31] no event smearing was used. Instead, the mass of the top quark was scanned over a wide range in order to account for detector resolution effects. The algorithm applied in the present analysis yields on average a 6% higher reconstruction efficiency compared to the method used in [11, 31]. In the old method the problem of solution ambiguities was tackled by using the solution with the maximum weight according

---

[1]When for a given smearing no kinematic solution is found w_i. and $\vec{p}_{t,i}$ are set to zero.

to the expected neutrino energy distributions in the laboratory frame. The weight distribution was determined from the complete Monte Carlo signal sample. This lead to some biases in the kinematic reconstruction towards smaller top and anti-top quark momenta and more central rapidities. According to the Monte Carlo simulation such biases are much reduced for the new reconstruction method.
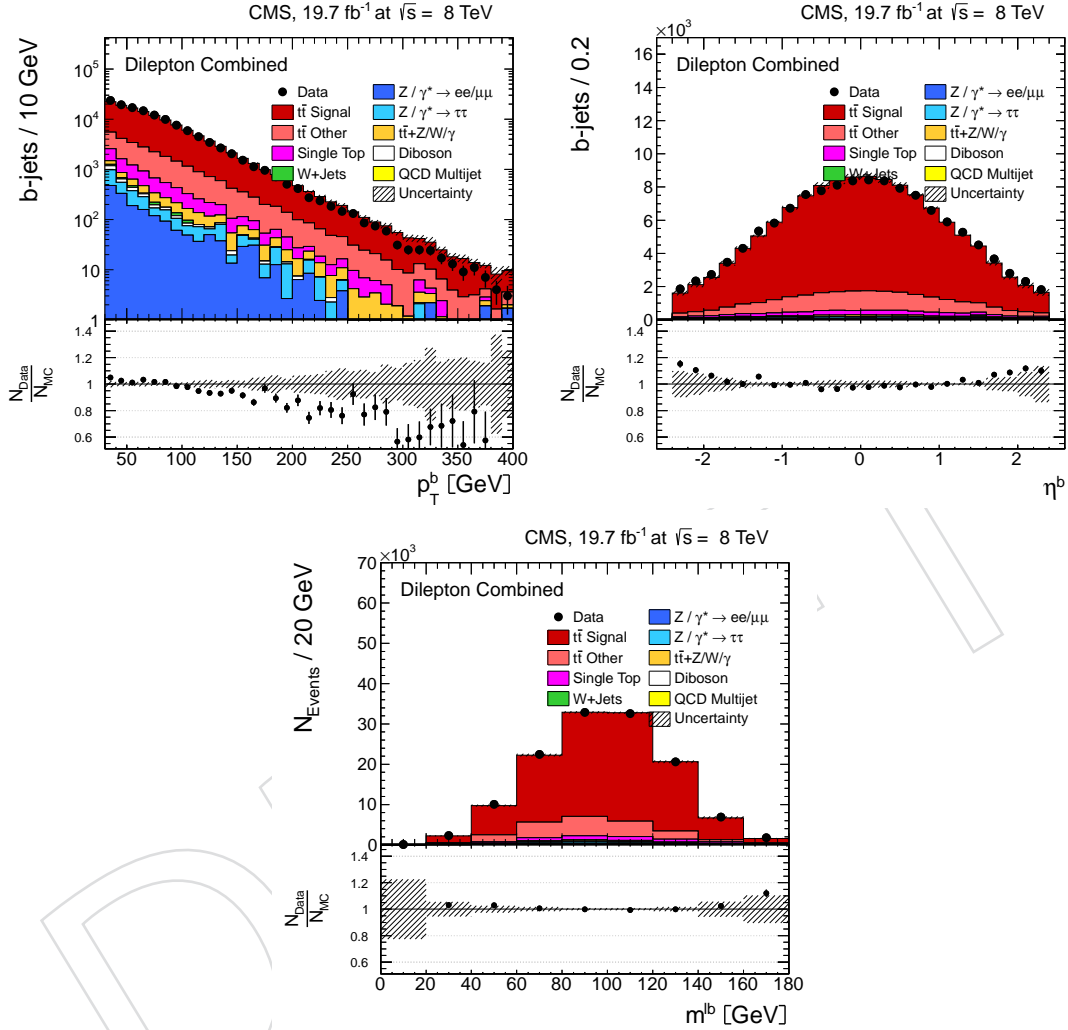

Figure 15: Distributions of the b-jets, and the lepton-b-jet system as obtained from the kinematic reconstruction. The top row shows the transverse momenta (left) and the pseudorapidity (right) distributions. The bottom plot shows the invariant mass of the lepton-b-jet system. Small scale factors as described in Section 7.4 are applied. The shaded area indicates the uncertainty on the $t\bar{t}$ modeling.

In Figures 15 to 16, the b-jet, top-quark and $t\bar{t}$ kinematic observables, as obtained from the kinematic reconstruction, are presented. A general good description of the data by the simulation is observed. The leptons (Fig. 5) and jets p_T(Fig. 8) spectra is predicted by the simulation to be harder than data. This effect was seen in the 7 TeV analysis [11]. Different event selection, in addition to requirements explained in Sec. 3, were tested to understand a possible source of this trend:
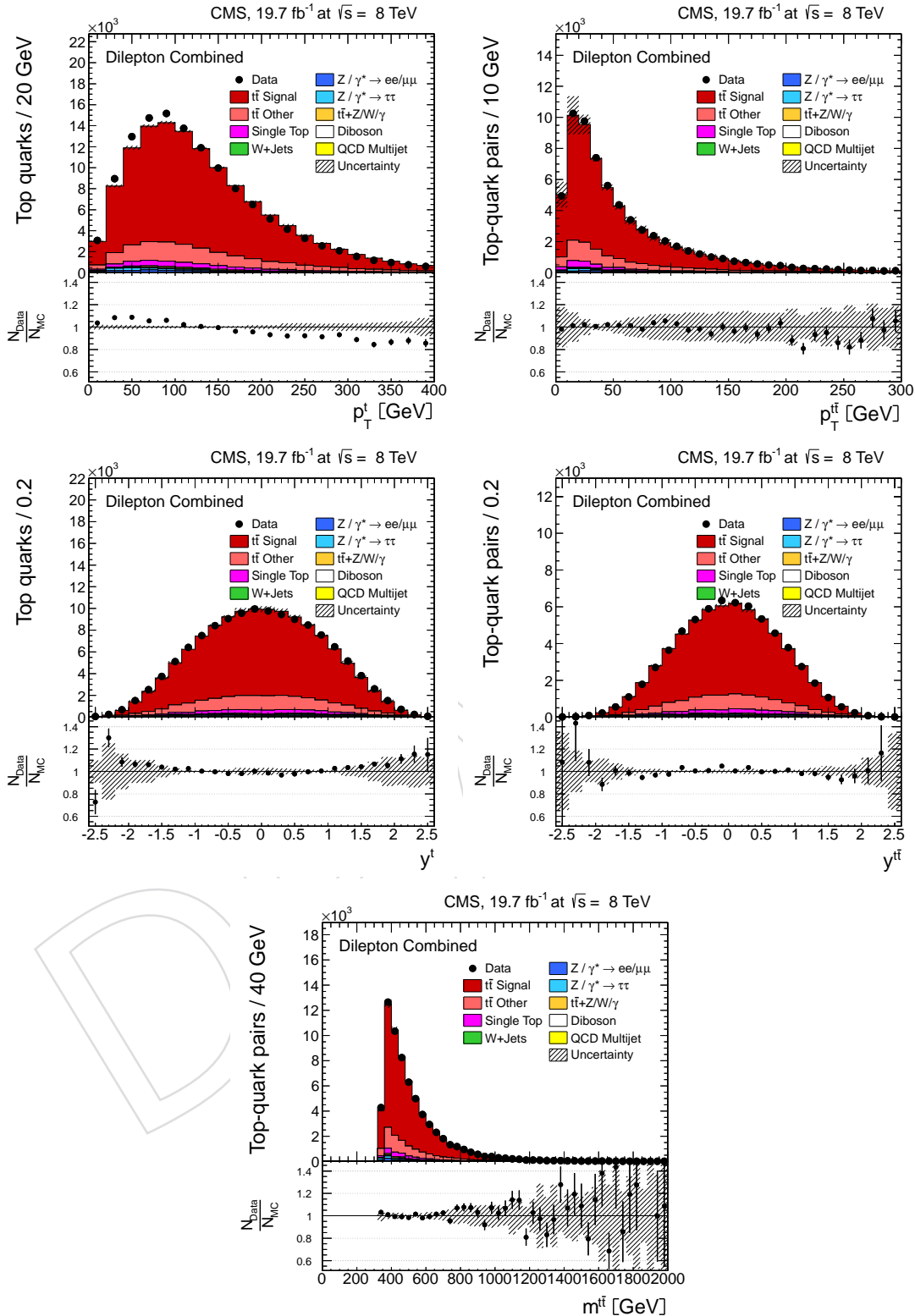
- PU<11
- PU$\in [11, 16]$

Figure 16: Distribution of top quark and $t\bar{t}$ quark pairs as obtained from the kinematic reconstruction. The left plots show the distribution for the top and anti-top quarks, the right plots show the $t\bar{t}$ system. The top row shows the transverse momenta, the middle plots show the rapidities of the top quark and top quark pair system, and the bottom plots show the reconstructed mass distribution of the top quark pair system. Small scale factors as described in Section 7.4 are applied. The shaded area indicates the uncertainty on the $t\bar{t}$ modeling.

392   • PU>16

393   • ≥ 2 CSVL jet

394   • ≥ 1 CSVT jet

395   Results of this tests can be seen in Appendix C. It can be observed that the trend in the lepton,
396   jet and top quark p_T spectrum remains despite the different event selection.

7   Scaling Factors and Systematic Uncertainties

398   In this section, each of the uncertainties is discussed for both the absolute measurement of
399   the inclusive cross section, as well as for the measurement of the normalised differential cross
400   section.

401   For the absolute measurement of the inclusive cross section, the full set of uncertainties, includ-
402   ing those affecting the normalisation of the data, i.e. the trigger and reconstruction efficiencies,
403   the acceptances, the calibrations, the model uncertainties, the integrated luminosity as well as
404   background estimates need to be taken into account. Dominant uncertainties of the measure-
405   ment of the absolute cross section originate from the b-tagging efficiency, the hadronisation
406   model, the lepton selection model and triggering, as well as the luminosity measurement.

407   In contrast, for the measurement of normalised differential cross sections $\frac{1}{\sigma}\frac{d\sigma}{dX}$, where X stands
408   for the respective observable, only those uncertainties are relevant that effect the shape of the
409   distributions. As a consequence, since all the normalisation uncertainties cancel, the relative
410   systematic error is significantly smaller.

411   In this analysis, for the measurement of the normalised differential cross sections, each uncer-
412   tainty is determined individually in each bin of the measurement. For each source of systematic
413   uncertainty, the impact on the final result is determined quantitatively in each bin of the mea-
414   surement by repeating the full analysis with appropriate variation of the corresponding input
415   assumption. The difference between the varied result and the nominal result is determined,
416   separately for each source of systematic uncertainty. The overall uncertainty on the measure-
417   ments is then derived by adding the individual contributions in quadrature.

418   In the following, the uncertainties are discussed in detail. A summary of the results and their
419   combination is given in Section 7.12. In the context of some of the uncertainties, correction
420   factors, generally referred to as "scale factors" (SF), are mentioned. Scale factors $SF = \frac{\epsilon_{data}}{\epsilon_{MC}}$ are
421   used where necessary to optimize the – generally already good – description of the data by the
422   simulation. The scaling factors are generally applied as event weights to the simulation, unless
423   stated differently.

7.1   Trigger Efficiency

425   The trigger efficiency is measured using triggers that are only weakly correlated to the dilepton
426   triggers, as described in Ref. [34]. A dependence on pseudorapidity of the muon and electron
427   of a few percent is observed and SFs are derived. Uncertainties in the inclusive cross section of
428   1.3% in the $\mu^+\mu^-$ channel, 1.4% in the e^+e^- and 1.3% in the $\mu^\pm e^\mp$ channel.

7.2   Lepton Selection

430   The identification and isolation efficiencies for muons (electrons) are estimated using the "tag-
431   and-probe" method with Z-boson event samples as a function of p_T and pseudorapidity [34],
432   and are found to be above 95% (90%) in all bins of the measurement. The muon efficiency is

well described in the simulation, i.e. with residual scale factors being very close to unity. For the electron efficiencies, the overall difference between data and simulation is estimated to be less than 2%. Uncertainties in the inclusive cross section of around 2.3% for the $\mu^+\mu^-$ channel, 2.4% for the e^+e^- and 2.2% for the $\mu^\pm e^\mp$ channel.

7.3 b-Tagging

Data-to-simulation SF for the b-tagging efficiency of individual b-jets, c-jets and light-(l) jets (typically referred to as *mistag rate* for c- and l-jets) are measured by the BTV group [23] using muon-jet and J/Ψ data samples. The SF are parameterised as a function of the jet p_T and η. For the CSVL tagger used in this analysis, the SF for b flavour jets is found to be between 0.96 and 1.00 with an error of up to 3.5% in the p_T=20-800 GeV and $|\eta| < 2.4$ ranges. The SF for c-jets is assumed to be the same as for b-jets with twice the quoted uncertainty, and the SF for l-jets is measured to be between 0.95 and 1.40 in this p_T range.

The individual b-tagging efficiency (ϵ_{MC}) of b-jets, and mistag rate for c- and l-jets, is determined from simulation. It does not only depend on the jet kinematic properties, but also on the analysis specific details. Results for this analysis are shown in Figure 17 as a function of the jet flavour, jet p_T and jet η.

The determination of the b-tagging uncertainty follows the recommendations of the BTV group, Ref. [35]. The uncertainty on the normalisation is determined by varying the SF within its uncertainty in the same direction, independently of the kinematic region.

To account for the uncertainty on the differential cross-section, the SF is varied by the corresponding uncertainty antagonistically depending on the kinematics of the jet. The SFs are scaled as a function of the p_T and $|\eta|$ of the jet independently, and antagonistically. The SF is scaled down (up) if the transverse momentum of the jet is smaller (greater) the median of the jets p_T for a variation "up", while for a "down" variation the SF is scaled up (down) if the p_T is smaller (larger) than the median value. E.g.:

- Variation "up": $SF - \Delta SF$ if $p_T < p_T^{median}$ and $SF + \Delta SF$ if $p_T > p_T^{median}$
- Variation "down": $SF + \Delta SF$ if $p_T < p_T^{median}$ and $SF - \Delta SF$ if $p_T > p_T^{median}$

A similar approach is used for the variation of the SF as a function of the $|\eta|$ of the jet. The median values are $p_T = 65\,GeV$ and $|\eta| = 0.75$.

The variation of the scale factor depends also in the flavour of the original parton which originates the jet. The heavy flavour (b and c) jets are considered fully correlated, while the light jets fully uncorrelated to the b-jets.

The variations of both variations (p_T and $|\eta|$) and each flavour are then summed in quadrature to give a global b-tagging uncertainty. For the inclusive cross section an uncertainty of 0.7%, 0.7% and 0.6% are measured in $\mu^+\mu^-$, e^+e^- and $\mu^\pm e^\mp$ channels respectively.

7.4 Kinematic Reconstruction Efficiency

The kinematic reconstruction algorithm used to reconstruct the properties of the top quarks has been described in Section 6. For a fraction of events (about 6%) no physical result is found and the events are rejected. This efficiency of the kinematic reconstruction algorithm has been studied in detail, as explained in the following.

The efficiencies of the kinematic reconstruction in the data and in the simulations are compared with respect to the lepton observables, the b jets and the $\not{E}_T$ distributions and are shown in
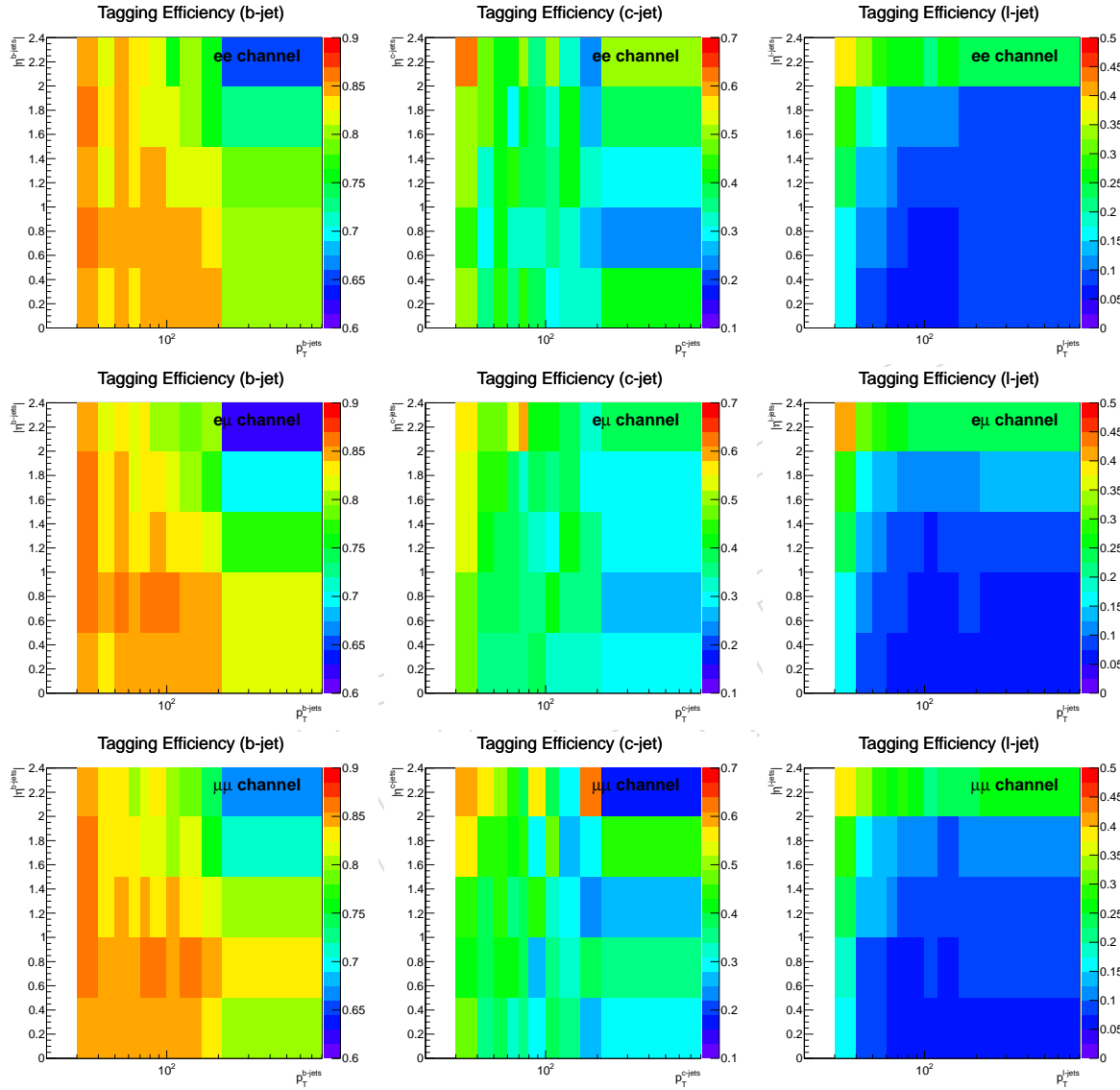
Figure 17: b-tagging efficiency of invidual b-jets (left) and mistag rate for c-jets (middle) and l-jets (right) as function of jet p_T and η for e^+e^- (top), $\mu^\pm e^\mp$ (center) and $\mu^+\mu^-$ (bottom) channels, determined from the simulation.

Figures 18 and 19 for the e^+e^-, $\mu^\pm e^\mp$ and $\mu^+\mu^-$ channels. The selection efficiency, calculated from the ratio of events before and after the kinematic event reconstruction and scale factors are also presented on these plots.
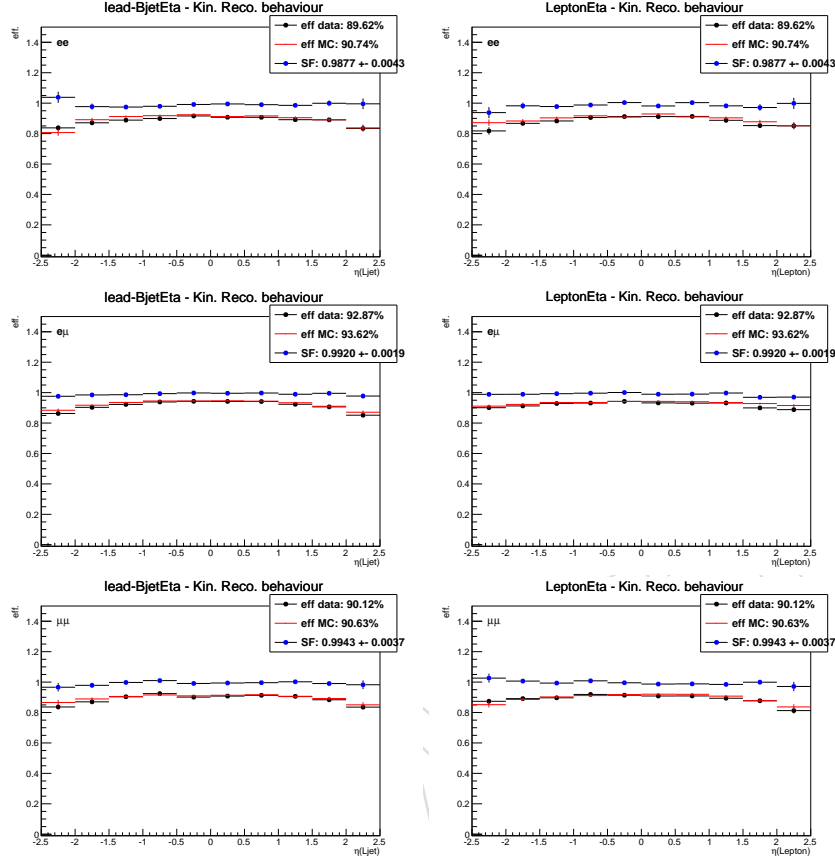

Figure 18: Efficiency of the kinematic reconstruction algorithm as a function of the jet (left column) and lepton (right row) η, in the e^+e^- (top row), $\mu^\pm e^\mp$ (central row) and $\mu^+\mu^-$ (bottom row) channels both for data (black) and simulation (red). The corresponding scale factor is also shown (blue).

7.5 Backgrounds

A large source of systematic uncertainty is the contribution from background events to the final sample. The background determination has been described in Section 5.

The uncertainty due to background normalisation is determined by variation of the backgrounds. In the $\mu^+\mu^-$ and e^+e^- channels the background from Z+jets processes is by far dominant, and its normalisation is varied by $\pm30\%$. The effect on the inclusive cross section is of the order of 2.4% in $\mu^+\mu^-$, 1.9% in e^+e^- channel and negligible in the $\mu^\pm e^\mp$ channel.

The contribution from backgrounds originating from Z+jets processes decaying into τ leptons, diboson, and single-top tW production are estimated from the simulation. Each source is varied up and down by $\pm30\%$. The resulting uncertainty on the total cross section measurement is about 1.4% in $\mu^+\mu^-$, 2.1% in e^+e^-, and 1.6% in the $\mu^\pm e^\mp$ channel.

7.6 Jet Energy Scale Uncertainty

To determine the uncertainty due to the jet energy scale (JES) the p_T- and η-dependent JES uncertainties provided by the CMS JetMET POG [36] are used, which are of the order of few
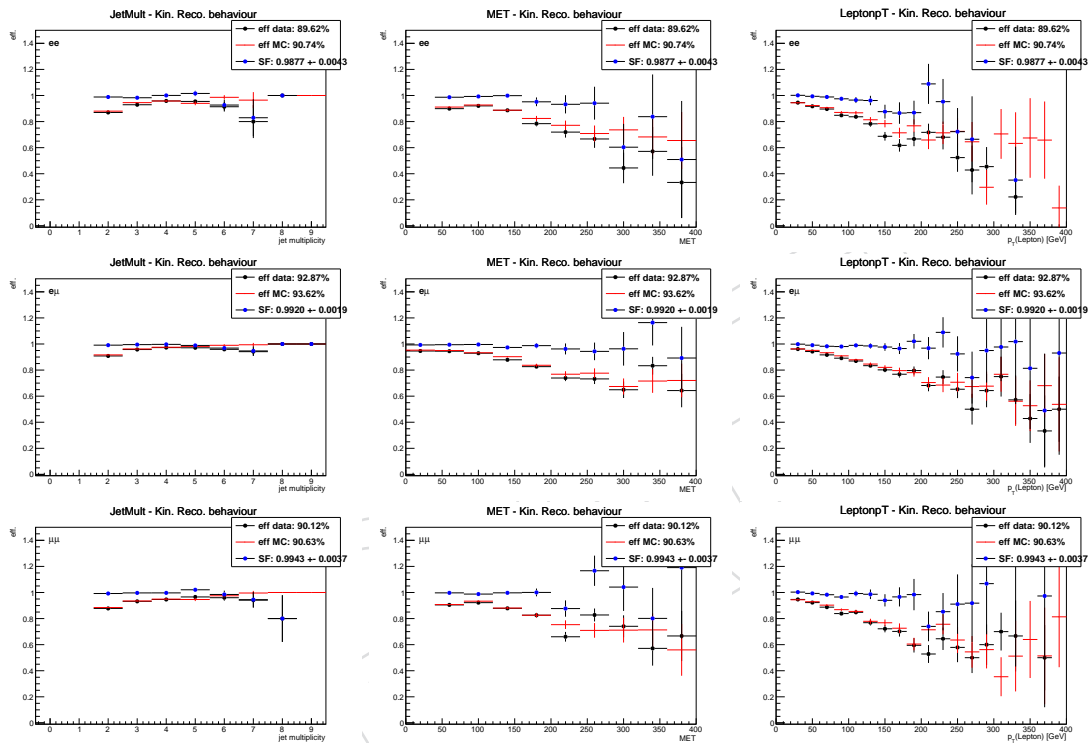
Figure 19: Efficiency of the kinematic reconstruction algorithm as a function of the jet multiplicity (left column), E_T^{miss} (central column) and leading lepton transverse momentum (right column), in the e^+e^- (top row), $\mu^\pm e^\mp$ (central row) and $\mu^+\mu^-$ (bottom row) channels both for data (black) and simulation (red). The corresponding scale factor is also shown (blue).

percent for high-energy jets. The simulation is run with the jet four momenta being scaled up and down by the corresponding uncertainties. The vectorial changes of the jet momenta are propagated to the missing transverse energy. The selection efficiency is recalculated with the rescaled simulated samples and the difference with respect to the original samples is taken as systematic uncertainty from the JES. This uncertainty on the total inclusive cross section is $\mu^+\mu^-$: 3.8%, e^+e^-: 4.0%, $\mu^\pm e^\mp$: 2.3%.

7.7   Jet Energy Resolution Uncertainty

The jet energy resolution in the simulation is increased by factors of 1.052, 1.057, 1.096, 1.134, 1.288 in the η ranges 0.0, 0.5, 1.1, 1.7, 2.3, 5.0 according the prescription given by the Jet/MET group [37].

The error on the inclusive cross section amounts to $\mu^+\mu^-$: 0.4%, e^+e^-: 0.4%, $\mu^\pm e^\mp$: 0.9% for the individual dilepton channels.

7.8   Pile-up

The pfNoPileUp removal algorithm is used to remove contributions from pile-up (PU) events as good as possible. However, pile-up events also affect the lepton isolation, the jet energy scale and the missing transverse energy distributions. The effects on the lepton isolation and global jet energy scale is already considered. To estimate the impact from pile-up on the signal selection efficiency, the simulated pile-up distribution is varied $\pm 5\%$ with respect the nominal value, and the cross section is recalculated.

The effect on the inclusive cross section is found to be below 0.2% and 0.4% for the same flavour (e^+e^- and $\mu^+\mu^-$) channels and 0.8% for $\mu^\pm e^\mp$ channel.

7.9   Luminosity

The uncertainty on the integrated luminosity for the 2012 data sample is presently 4.4% [13].

7.10   Decay Branching Fraction

The branching fractions for $W \to \ell\nu$ and $\tau \to \ell\nu\nu$ are taken from PDG [38]. The branching fraction of $b_{W\to\ell\nu} = 0.1080 \pm 0.0009$ is taken for all three lepton flavours. The branching fraction of taus decaying into a muon is given by $b_{\tau\to\mu\nu\nu} = 0.1741 \pm 0.0004$. For taus decaying to an electron it is $b_{\tau\to e\nu\nu} = 0.1783 \pm 0.0004$. Events resulting from tau decays are considered background and not included in the branching ratio calculation. A systematic uncertainty of 1.5% is assigned to the branching fraction.

7.11   Model Uncertainties

Dedicated signal simulation samples are used for the determination of the model uncertainties of this measurement. For each of the samples the analysis was then redone and the variation with respect to the reference was determined as explained in the following.

Hadronisation Uncertainty

The uncertainty arising from assumptions on the hadronisation process is determined by taking the difference of the results using a simulation of POWHEG [8–10] and MC@NLO [7]. The estimated value for the uncertainty on the inclusive cross section is 1.3% for the $\mu^+\mu^-$ channel, 1.9% for the $\mu^\pm e^\mp$ channel and 2.4% for the e^+e^- channel.

Table 6: Summary of the systematic uncertainties for the measurement of the inclusive $t\bar{t}$ cross section. The contribution from non-Z+jets backgrounds is referred to as *Background (other)*.

source	uncertainty (%)			
	$\mu^+\mu^-$	e^+e^-	$\mu^\pm e^\mp$	combined
Trigger efficiency	1.3	1.4	1.3	1.3
Lepton selection	2.3	2.3	2.2	2.3
Backgrounds (other)	1.8	2.5	2.2	2.2
Backgrounds (Z+jets $\rightarrow \mu\mu$ / ee)	1.1	0.9	0.0	0.4
Jet energy scale	3.1	3.1	2.1	2.5
Jet energy resolution	0.6	0.5	0.1	0.2
Pile-up	0.1	0.2	0.4	0.3
B-tagging	0.7	0.6	0.6	0.6
Kinematic fit	0.4	0.5	0.2	0.3
Hadronisation	1.1	2.6	1.9	1.9
Top quark mass	1.0	0.9	0.6	0.7
Q^2 scale	2.0	1.9	1.1	1.4
ME/PS thresh.	0.6	0.8	0.4	0.5
PDF	0.2	0.3	0.3	0.3
$\mathcal{BR}\,(t\bar{t} \rightarrow \ell\ell + X)$	1.5	1.5	1.5	1.5
Luminosity	4.4	4.4	4.4	4.4
Total systematic error	7.6	8.2	6.3	6.7
Statistical error	1.0	1.1	0.5	0.4

Top Quark Mass

For the uncertainty of the top quark mass – which in the default sample is 172.5 GeV– two samples with with a top mass of 169.5 GeV and 171.5 GeV are used to estimate the impact of the top mass uncertainty on the signal selection efficiency.

Hard Scattering Q^2 Scale and Matching Scale

For the Q^2 scale, two samples are used with the scale being increased and decreased by a factor of four. The impact on the selection efficiency is small. The systematic uncertainty is estimated individually in each bin by taking the averaged differences of the up and down variations to the default.

Furthermore, the effect of additional jet production in MADGRAPH [6] is studied by varying the threshold between jet production on matrix-element level and via parton showering (matching scale). The systematic uncertainty is estimated individually in each bin by taking the averaged differences of the up and down variations to the default. The uncertainty on the effect of the initial and final state radiation on the signal efficiency is covered by the uncertainty on the Q^2 and matching scales.

Parton Distribution Function

The uncertainty arising from the parton distribution functions (PDF) is assessed by reweighting the $t\bar{t}$ signal sample according to the 44 CTEQ66 error PDF sets, at 90% confidence level. The effects of these variations are added in quadrature. The uncertainties in the inclusive cross section are in the 0.2-0.3% range, depending on the specific channel.

Table 7: Summary of the median values of the uncertainty values for top-quark differential cross sections (in %). Uncertainties are indicated for variables measured in the visible and full phase space separately. They correspond to the fraction of systematics that are uncorrelated between different bins of the measurement. The contribution from non-Z+jets backgrounds is referred to as *Background (other)*.

Source	Visible PS Uncertainty (%)				Full PS Uncertainty (%)			
	$\mu^+\mu^-$	e^+e^-	$\mu^\pm e^\mp$	combined	$\mu^+\mu^-$	e^+e^-	$\mu^\pm e^\mp$	combined
Trigger efficiency	0.1	0.1	0.1	0.1	0.1	0.2	0.1	0.1
Lepton selection	0.1	0.1	0.1	0.1	0.1	0.1	0.1	0.1
Backgrounds (other)	0.3	0.8	0.5	0.4	0.2	0.7	0.5	0.4
Backgrounds (Z+jets $\rightarrow \mu\mu$ / *ee*)	0.4	0.4	≤ 0.1	0.2	0.4	0.6	0.1	0.1
Jet energy scale	0.7	0.8	0.3	0.4	1.0	1.8	0.8	0.8
Jet energy resolution	0.5	0.5	0.1	0.2	0.6	0.7	0.4	0.3
Pile-up	0.2	0.3	0.1	0.1	0.2	0.3	0.2	0.1
B-tagging	0.2	0.3	0.1	0.1	0.3	0.3	0.2	0.2
Kinematic fit	≤ 0.1	≤ 0.1	≤ 0.1	≤ 0.1	≤ 0.1	≤ 0.1	≤ 0.1	≤ 0.1
Hadronisation	2.0	2.0	1.3	1.4	2.3	2.0	1.5	1.4
Top quark mass	1.2	1.3	0.7	0.6	1.7	1.6	0.8	0.7
Q^2 scale	1.2	1.7	1.0	0.7	1.7	1.9	1.4	1.2
ME/PS thresh.	1.1	1.3	0.6	0.5	1.0	1.9	0.8	0.8
PDF	0.2	0.2	0.1	0.2	0.5	0.5	0.5	0.5

7.12 Overview of Systematic Uncertainties

The breakdown of systematic uncertainties for the absolute inclusive cross section measurement is shown in Table 6. The quadratic sum of all the sources of uncertainty yields a total uncertainty of approximately 6-8%.

For the normalised differential cross section analysis the uncertainties are determined and applied separately in each bin of the measurement. The contributions from each uncertainty to each bin of the measurement are visualized in Figures 20 to 23, where the squared sum of the experimental and theoretical systematic errors are displayed separately for each bin of the normalised differential cross section measurement. The figure shows that the dominant sources of uncertainty are the model uncertainties. This is expected, as most experimental uncertainties are correlated among the various bins of the measurement and thus do not affect the shape of the distributions. By far, the largest systematic errors are located at large values of transverse momentum or mass. A closer study has proven that these variations are due to the statistical accuracy of the presently available simulations.

To achieve a better view of the different sources of uncertainty, Figures 24 to 27 show the relative errors separately for the purely experimental uncertainties, the model uncertainties and the statistical uncertainty in each bin of the normalised differential cross section. The figures illustrate that the model uncertainties generally exceed the experimental uncertainties.

In Table 7, the median value, of all measurent bins, of the systematic uncertainty of all variables are listed. Uncertainties due to an specific systematic source are listed. The results are separated between results measured in the visible phase space and extrapolated to the full phase space. More details on the visible phase space are given in Sec. 8.2.

573 In App. D the full correlation matrix of systematic uncertainties are shown. Correlation matri-
574 ces are presented for all variables measured in this analysis in the combined channel. Details
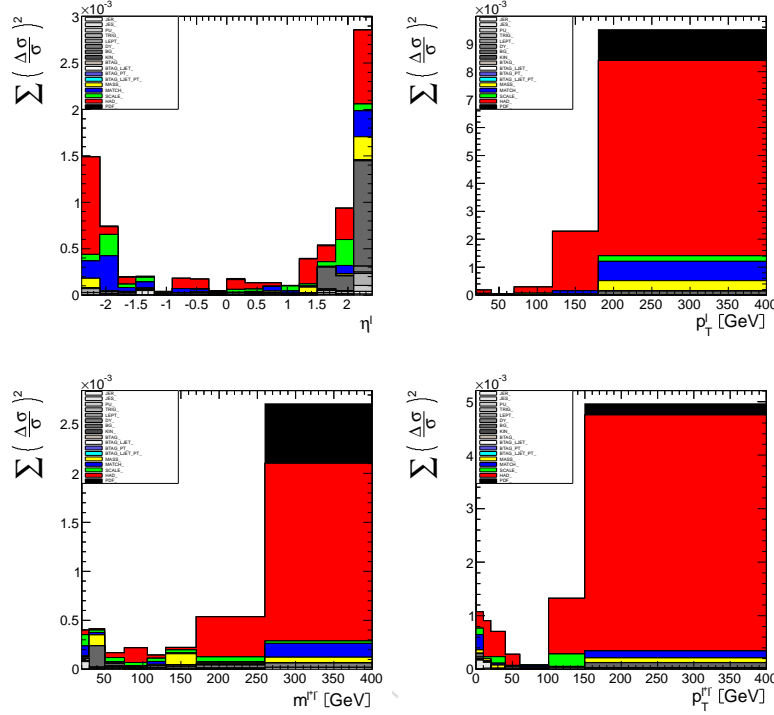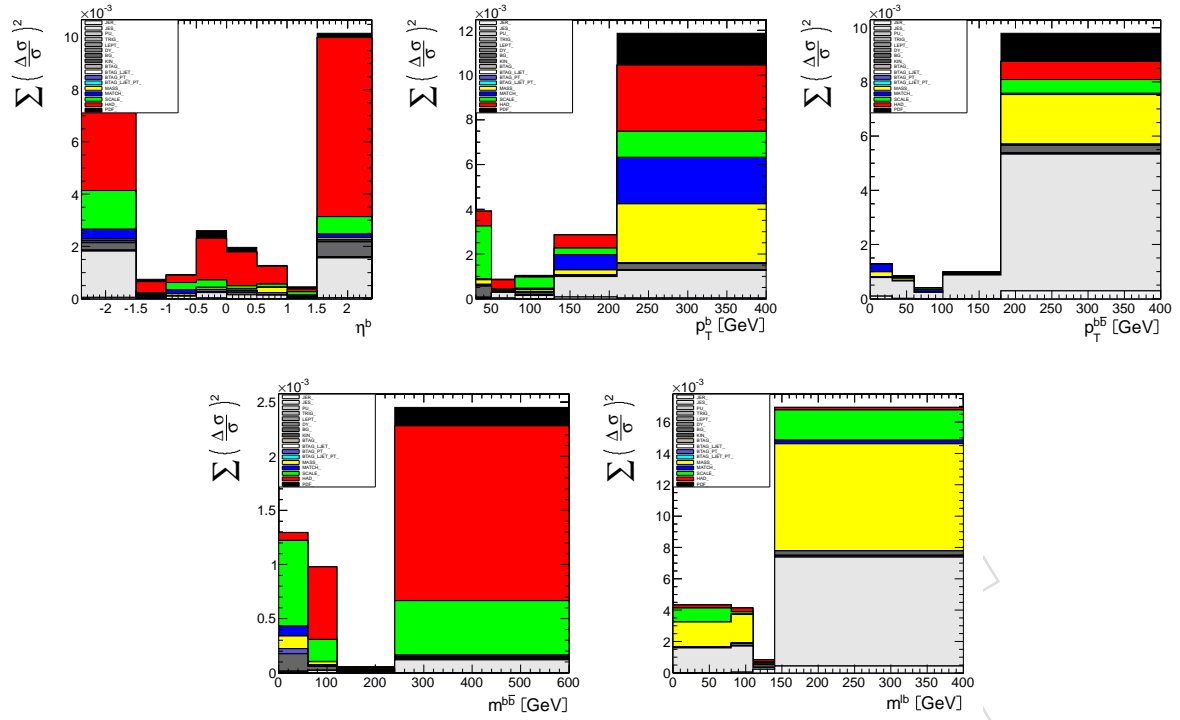575 on the calculation of the covariance matrix are given in App. D.

Figure 20: The squares of the systematic errors in each bin of the measurement for differential cross
section distributions as a function of the leptons and the lepton-pair.

8 Cross Section Definition and Extraction

577 The cross section is measured from the event sample obtained after all the full event selection,
578 including the b-tagging and the kinematic top-quark reconstruction described in Section 6. The
579 same event selection is used for the measurement of the normalised differential cross sections
580 as a function of top quark, lepton and b-jet kinematic observables, and also for the absolute
581 inclusive cross section measurement.

582 The measurement proceeds by determining the cross sections independently for each of the
583 three decay channels ($\mu^+\mu^-$, e^+e^-, $\mu^\pm e^\mp$) using the event selection, background estimation
584 and efficiency corrections described in previous sections. The combination of the three decay
585 channels is performed at the cross section level and is described in Section 8.4.

8.1 Inclusive Cross Section Definition

587 In each channel, the inclusive cross section is calculated from the number of selected events,
588 after background subtraction, and correcting for detector and reconstruction efficiencies, as:

$$\sigma_{t\bar{t}} = \frac{(N_{\text{Data}} - N_{\text{BG}}) \cdot f_{sig.}}{\epsilon_{\text{sig}} \, b_{t\bar{t}\to\ell\ell X} \, L} \tag{12}$$

$$f_{sig.} = \frac{N_{t\bar{t}\,signal.}}{N_{t\bar{t}\,signal.} + N_{t\bar{t}\,other}} \tag{13}$$

Figure 21: The squares of the systematic errors in each bin of the measurement for differential cross section distributions as a function of the b-jets, b-jet-pair and lepton-b-jet invariant mass.
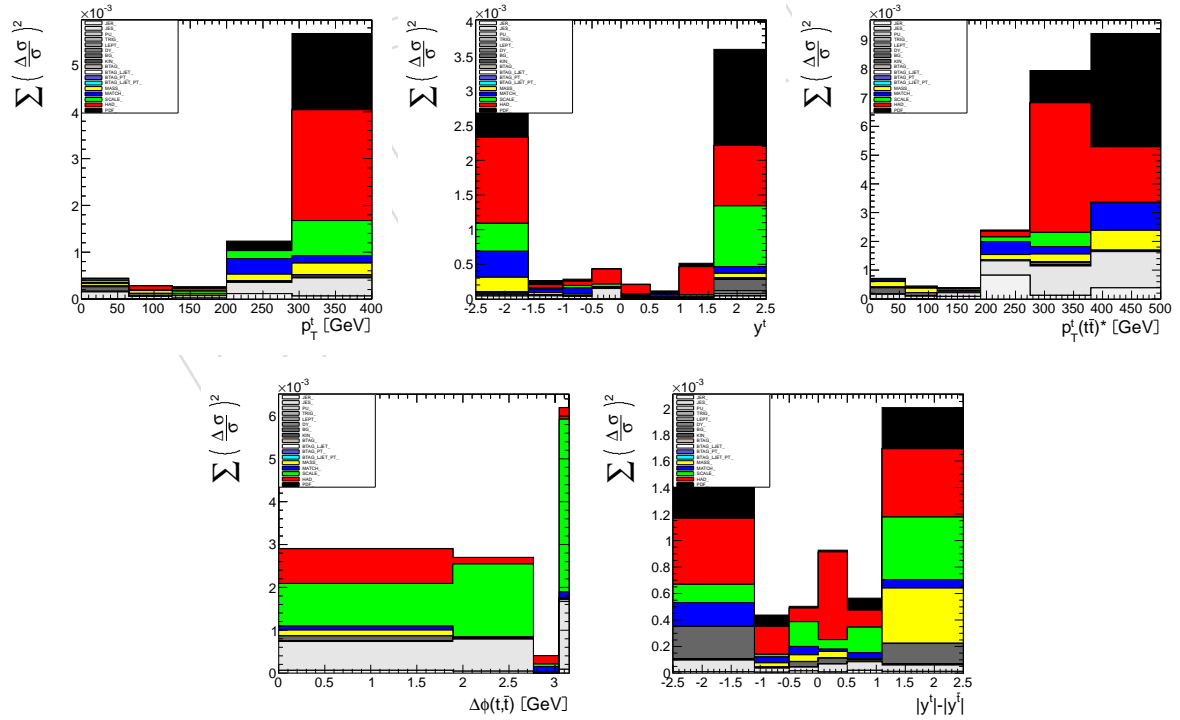

Figure 22: The squares of the systematic errors in each bin of the measurement for differential cross section distributions as a function of the top quarks.
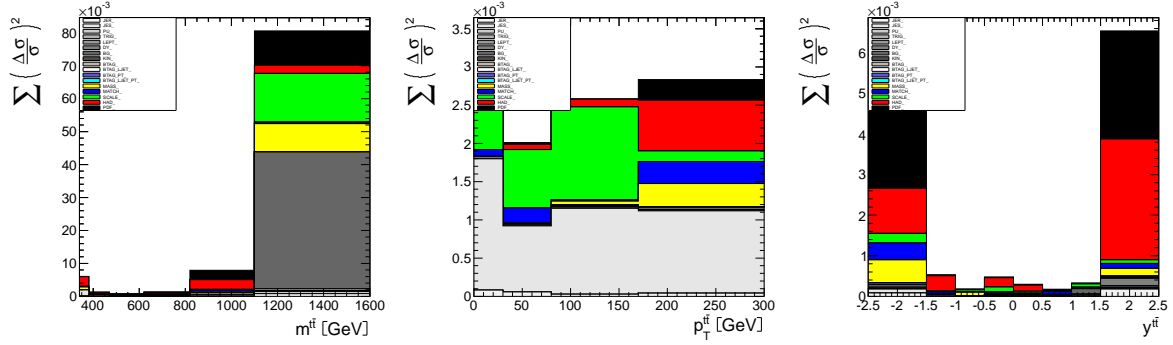
Figure 23: The squares of the systematic errors in each bin of the measurement for differential cross section distributions as a function of the $t\bar{t}$ system.
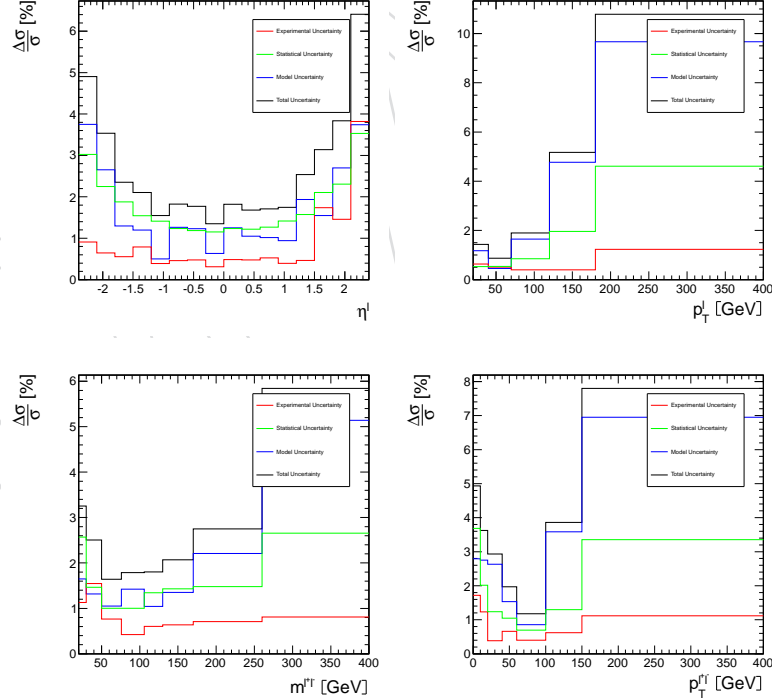

Figure 24: Comparison of relative systematic (model and experimental) and statistical errors in each bin of the measurement for differential cross section distributions as a function of the leptons and lepton-pair.
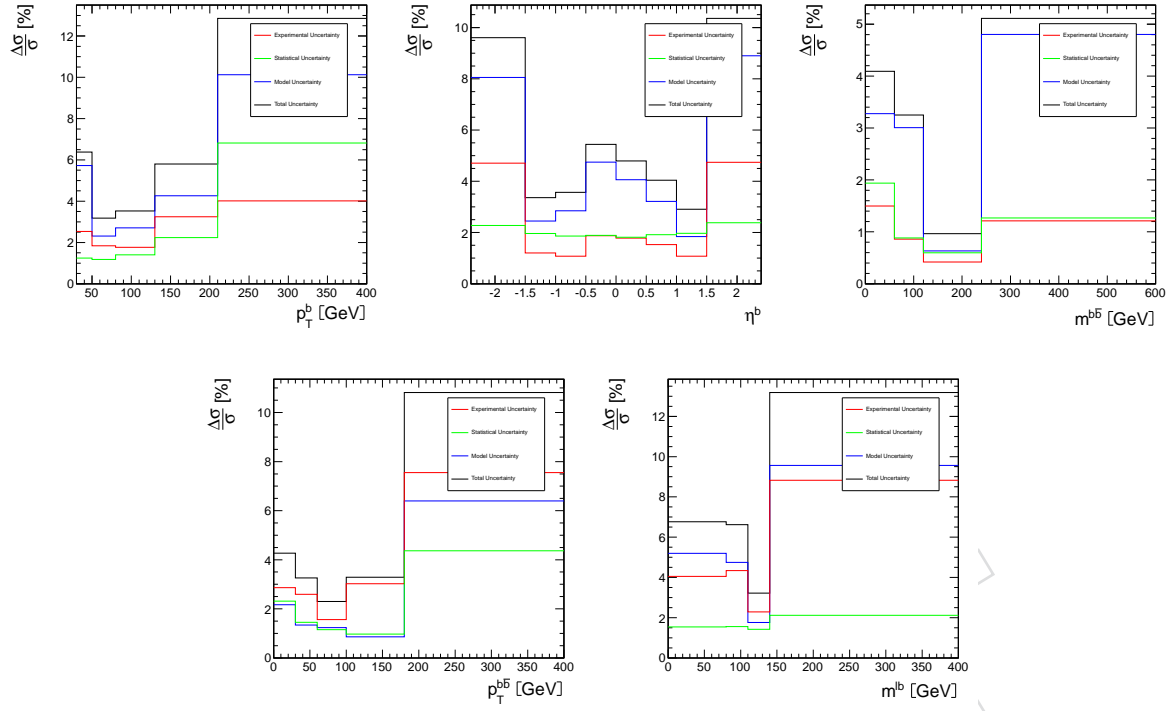
Figure 25: Comparison of relative systematic (model and experimental) and statistical errors in each bin of the measurement for differential cross section distributions as a function of the b-jet, b-jet-pair system and lepton-b-jet invariant mass.
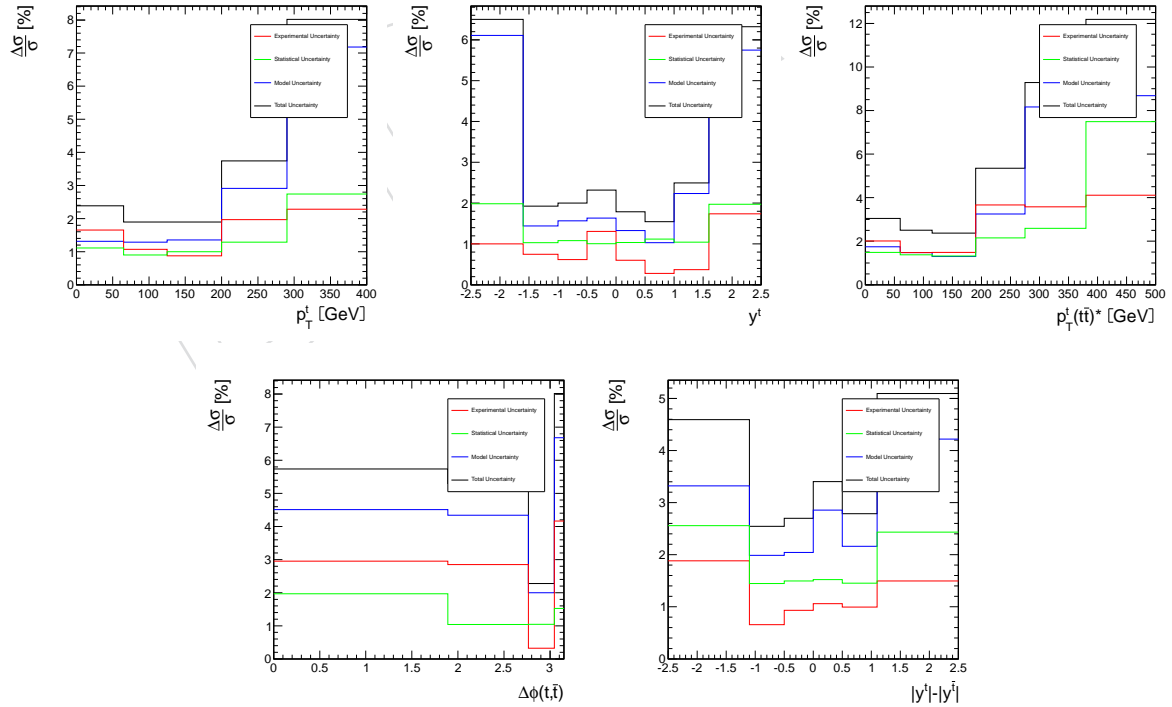

Figure 26: Comparison of relative systematic (model and experimental) and statistical errors in each bin of the measurement for differential cross section distributions as a function of the top quarks.
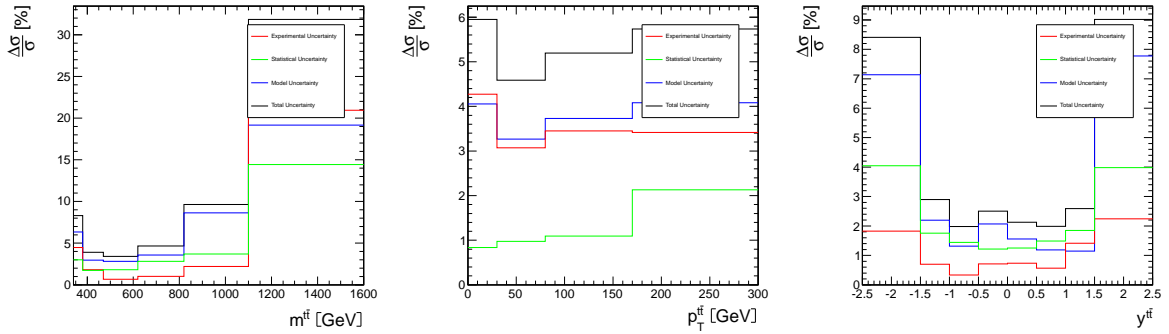
Figure 27: Comparison of relative systematic (model and experimental) and statistical errors in each bin of the measurement for differential cross section distributions as a function of the $t\bar{t}$ system.

Here, N_{Data} corresponds to the number of events in data after full event selection, N_{BG} is the number of background events not considering $t\bar{t}$ events not decaying into prompt leptons. This number of events is then corrected by a factor that takes into account the $t\bar{t}$ signal fraction f_{sig}. to reduce any dependency in the normalisation of the input $t\bar{t}$ simulation. The signal event selection efficiency, ϵ_{sig}, is the ratio of the number of reconstructed events that survive all the selection steps to the number of total events that were originally produced. It is taken from the simulation of the signal as corrected by the scale factors for trigger, lepton selection, and b-tagging efficiencies (cf. Section 7).

The $t\bar{t}$ decay branching ratio for the dilepton channel is given by $b_{t\bar{t}\to\ell\ell X}$. L is the total integrated luminosity centrally provided by CMS. The absolute inclusive cross section quoted here is defined in the full phase space, i.e. the simulation is used to correct for the fraction of unmeasured events inside and outside the experimentally accessible phase space. The statistical uncertainty on $\sigma_{t\bar{t}}$ arises from N_{Data}, assuming Gaussian behaviour. The systematic error is assessed by individual variation of the sources of systematic uncertainties as described in Section 7.

8.2 Normalised Differential Cross Section Definition

The normalised differential $t\bar{t}$ cross sections $\frac{1}{\sigma}\frac{d\sigma}{dX}$ are measured as a function of the kinematic properties of the leptons, lepton pairs, the b-jets, b-jet pairs, top quarks and top quark pair. The kinematic properties of the top quarks and $t\bar{t}$ are reconstructed from the kinematic top-quark event reconstruction described in Section 6.

Except for the top quark and top-quark pair properties, the differential cross sections are defined at particle level in a certain kinematic ("visible") phase space. A b jet at particle level is defined in Monte Carlo simulation as a generator level jet which contains the decay products of a stable B-hadron. The two highest transverse momentum jets originated from distinct B-hadrons are selected as the representative jets at particle level. The visible phase space is defined for the the region in which the transverse momentum of the leptons is $p_T^\ell > 20$ GeV and their pseudorapidity $|\eta^\ell| < 2.4$. The b jets are required to have a transverse momentum $p_T^b > 30$ GeV and a pseudorapidity $|\eta^b| < 2.4$. The phase space definition for the leptons (b jets) on particle level corresponds to the lepton (jet) selection on reconstruction level. The top quark and top-quark pair differential cross sections are defined at parton level in the full phase space.

For each observable X the measurement is performed as described above, but separately for

621   each bin i and normalised to the bin width Δ_X^i:

$$\frac{1}{\sigma}\frac{d\sigma^i}{dX} = \frac{1}{\sigma}\frac{x^i}{\Delta_X^i \, L} \tag{14}$$

622   Here, x^i denotes the measured event count in bin i after background subtraction, correction for
623   detector efficiency, acceptance and bin-to-bin migration. This correction is facilitated by a full
624   unfolding approach that is summarized below.

625   The normalised differential cross section measurement for each observable is then derived by
626   dividing the corrected number of signal events by the width of the bin Δ_X^i, the integrated lumi-
627   nosity L, and by the corresponding measured total cross section in the same phase space. The
628   choice of the bin width is motivated in Section 8.3.

629   The statistical error on the measurement in each bin arises from N_{Data}^i, assuming Gaussian
630   behaviour. The systematic error is assessed by individual variation of the sources of systematic
631   uncertainties as described in Section 7. Due to this normalisation, the systematic uncertainties
632   are significantly reduced.

8.3   Bin-to-bin Migration and Unfolding

634   For the measured observables, effects from finite experimental resolution can lead to migrations
635   of events across bin boundaries, that is, events that are actually produced (generated) in one
636   bin might be measured (reconstructed) in another bin. These bin-to-bin migrations are studied
637   in terms of the *purity* and *stability* in each bin, as determined from the simulation.

638   The purity p^i denotes the number of events that are generated and correctly reconstructed in
639   a given bin i relative to the number of events that are reconstructed in bin i but generated
640   anywhere. The stability s^i denotes the number of events that are generated and correctly re-
641   constructed in a given bin i relative to the number of events that are generated in bin i but
642   reconstructed anywhere:

$$p^i = \frac{N_{rec\&gen}^i}{N_{rec}^i} \tag{15}$$

$$s^i = \frac{N_{rec\&gen}^i}{N_{gen}^i} \tag{16}$$

643   where *rec* refers to reconstructed events fulfilling the full selection requirements described be-
644   fore and *gen* refers to generated events where the final state leptons and partons before radia-
645   tion fulfill the phase space requirements.

646   Without migration effects, purity and stability would be equal to one. The purity (stability)
647   is sensitive to migrations into (out of) the bin. In order to keep bin-to-bin migrations accept-
648   ably small, the bin widths for each observable are optimized such that for each bin purity and
649   stability are greater than about 50%.

650   In order to correct for bin migrations and efficiency, a regularized unfolding is applied on all
651   differential distributions. These methods have been described in [39, 40] and are briefly sum-
652   marized here.

653   From the signal Monte Carlo, a *response matrix* A is calculated:

$$A_{ij} := \frac{N_{rec}^{j \to i}}{N_{gen}^{j}} \tag{17}$$

Here, $N_{rec}^{j \to i}$ denotes the number of reconstructed events that are generated in bin j and reconstructed in bin i. This means that the entries A_{ij} can be regarded as transition probabilities from generator level bin j to reconstructed level bin i. The corrected (unfolded) event yield x^j in bin j is then given by solving the equation:

$$\sum_{j} A_{ij} x^j = N_{Sig}^i := N_{Data}^i - N_{BG}^i \tag{18}$$

Equation 18 can be solved in a χ^2-sense. Introducing a vector notation for binned distributions $\vec{a} = (a^1, \ldots, a^j, \ldots, a^n)$, the problem can be formulated as

$$\chi_A^2 (\vec{x}) := \left(A\vec{x} - \vec{N}_{Sig} \right)^T COV_{\vec{N}_{Sig}} \left(A\vec{x} - \vec{N}_{Sig} \right) \tag{19}$$

where $COV_{\vec{N}_{Sig}}$ is the covariance matrix of the background-subtracted data distribution.

A typical feature of unfolding problems are large fluctuations in the result x^j due to the rank deficiency of the response matrix. This makes a smoothing prescription necessary (*regularization*), which is implemented by adding a penalty term

$$\chi_L^2 (\vec{x}) := \sum_{ij} \frac{x^i}{N_{gen}^i} L_{ij}^2 \frac{x^j}{N_{gen}^j} \tag{20}$$

to Equation 19, that is sensitive to fluctuations in the bin wise ratio between the unfolded result $\vec{x}$ and expected MC truth $\vec{N}_{gen}$. Here, L_{ij}^2 is given by the elements of the following *curvature matrix*:

$$\boldsymbol{L}^2 \equiv (L_{ij}^2) := \begin{pmatrix} 1 & -1 & & & \\ -1 & 2 & -1 & & \\ & \ddots & \ddots & \ddots & \\ & & -1 & 2 & -1 \\ & & & -1 & 1 \end{pmatrix} \tag{21}$$

The penalty term is steered via the *regularization parameter* τ, such that $\vec{x}$ is obtained by minimizing the following χ^2-function:

$$\chi^2 (\vec{x}) := \chi_A^2 (\vec{x}) + \tau^2 \cdot \chi_L^2 (\vec{x}) \tag{22}$$

Note that, given a proper choice of τ, the penalty term (20) damps short-range fluctuations in the result $\vec{x}$ without affecting the global shape of $\vec{x}$.

The adjustment of τ is a critical choice in every unfolding problem, since it has to facilitate the removal of unphysical fluctuations without introducing a bias. In order to optimize τ, the *global correlation method* is used. This method employs the notion of global correlation [41], which is a

674 measure of the correlation between a single bin and its periphery. For a bin j and a solution $\vec{x}$ it
675 is defined by scanning all linear combinations $\sum_{j \neq i} \alpha_j x^j$, $\alpha_j \in \mathbb{R}$ for the one which is maximally
676 correlated to x^i:

$$\rho_i := \max_{(\alpha_1,\ldots,\alpha_n)} \rho \left(x^i, \sum_{j \neq i} \alpha_j x^j \right) \tag{23}$$

677 Note that ρ_i is sensitive to the regularization parameter τ, exhibiting large values in the two
678 cases of under-smoothing and over-smoothing. Hence, the regularization level is optimised by
679 searching for the τ that minimizes the *average squared global correlation*:

$$\bar{\rho}\left(\tau \right) := \frac{1}{n} \sqrt{\sum_i \rho_i\left(\tau \right)^2} \tag{24}$$

680 The unfolded mean values x^j are directly calculated by minimizing Equation 22. The statistical
681 covariance matrix $COV_{\vec{x}}$ of the result $\vec{x}$ is obtained by error propagation from $COV_{\vec{N}_{Sig}}$. For this
682 purpose, pseudo-experiments are employed overlaying the input data distribution with noise
683 according to its statistical uncertainty. This way, not only the unfolded statistical uncertainties
684 δx^j are obtained, but all bin-to-bin correlations $\rho\left(x^i, x^j \right)$ are properly quantified.

685 Systematic uncertainties are propagated in the usual way: the analysis is repeated for the nom-
686 inal and all the shifted Monte Carlo samples and the bin-wise relative shifts on the unfolded
687 distributions are calculated.

688 Checks are performed to study any possible bias of the unfolding method. Pseudo-data, with
689 different varied truth shapes, is unfolded using the unfolding method explained above. Results
690 are shown in Appendix B.1. Additionally 1000 pseudo-experiments are performed and the pull
691 distributions are derived. Results are shown in B.2.

692 **8.4 Combination of Channels**

693 The cross sections values for the three $\mu^+\mu^-$, e^+e^- and $\mu^\pm e^\mp$ channels are combined based on
694 the statistical error of the measurement. Since the three results are statistically independent,
695 the combination proceeds by computing the error weighted mean for each cross section mea-
696 surement. For the normalised differential cross sections the combination is performed in each
697 bin of each measurement.

The combined cross section is thus given by

$$\sigma = \sum \left(\frac{\sigma_i}{\delta\sigma_i^2} \right) \Big/ \sum \left(\frac{1}{\delta\sigma_i^2} \right) \tag{25}$$

698 where σ_i are the cross section results (either the inclusive cross section or the normalised differ-
699 ential cross section) in the different decay channels with $i = \mu^+\mu^-$, e^+e^- and $\mu^\pm e^\mp$, and $\delta\sigma_i$ are
700 their corresponding uncertainties.

The statistical uncertainty on the combined cross section is

$$\delta\sigma = 1 \Big/ \sqrt{\sum \left(\frac{1}{\delta\sigma_i^2} \right)}. \tag{26}$$

Table 8: Signal and background contributions after full event selection.

source	$\mu^+\mu^-$	e^+e^-	$\mu^\pm e^\mp$	combined
non-dilepton $t\bar{t}$	1080.19	1431.51	5375.08	8614.77
$t\bar{t} + Z/W/\gamma$	153.43	120.31	408.44	682.18
tW	470.79	356.83	1374.94	2202.56
Diboson	53.96	40.24	153.46	247.66
$Z/\gamma^\star \to \tau^+\tau^-$	101.82	111.44	483.09	696.36
$Z/\gamma^\star \to \mu^+\mu^-$ / $Z/\gamma^\star \to e^+e^-$	471.27	296.61	22.91	784.64
W+jets	7.21	27.12	86.34	120.67
QCD	0	127.68	244.23	371.91
total backgrounds	30666.7	2511.8	8148.40	13720.80
$t\bar{t}$	10901	8507.45	31602.20	51010.60
data	14403	10678	39640	64721

701 The systematic uncertainties are assessed on the combined cross sections, i.e. the full analysis
702 including the three separate channels and their combination is repeated for every systematic
703 variation and the difference with respect to the nominal (non-varied) combined value is taken
704 as systematic uncertainty for each bin and each measured observable. This way the possible
705 correlations of the systematic errors between the different channels are taken into account.

706 9   Results of the Measurement

707 9.1   Inclusive Cross Section

708 The inclusive cross section for $t\bar{t}$ production is calculated for each channel after full event se-
709 lection and extrapolated to the full phase space as described in Section 8.1.

710 The signal and background contributions for the different channels are detailed in Table 8.

Table 9: Inclusive cross sections as measured separately for the three dilepton channels.

Channel	$\mu^+\mu^-$	e^+e^-	$\mu^\pm e^\mp$	combined
Events in data	14403	10678	39640	64721
Background events	1258.5	1080.23	2773.4	5105.97
Total efficiency and acceptance	19.4%	15.1%	28.2%	22.6%
Branching ratio	1.16%	1.16%	2.33%	4.65%
Cross section [pb]	253.5	236.7	244.6	245.1
Statistical error [pb]	2.3	2.6	1.3	1.0
Systematic error [pb]	15.4	15.9	13.7	14.3
Total error [pb]	15.6	16.1	13.8	14.3

711 The results of the measurement for the inclusive $t\bar{t}$ production cross sections in each channel
712 are listed in Table 9. The selection efficiency is taken from the simulation of the signal and
713 corrected for the trigger and b-tagging efficiencies. The results from the three channels are in
714 agreement with each other within their statistical uncertainties.

715 The combination of the three decay dilepton channels is performed according to the prescrip-
716 tion given in Section 8.4 and an inclusive $t\bar{t}$ quark pair production cross section of $\sigma_{t\bar{t}} =$
717 $245.10 \pm 1.05(stat.) \pm 14.25(syst.) \pm 14.29(total)$ pb is obtained.

₇₁₈ Reasonable agreement with a recent CMS measurement [28] can be claimed, given that the two
₇₁₉ analyses differ substantially in a number of aspects, e.g. the kinematic reconstruction and the
₇₂₀ electron identification. Figure 28 shows a comparison of the measurements with a Next-to-
₇₂₁ Leading-Order (NLO) calculation with MCFM (version 5.7) [42] using the PDF set CTEQ66M,
₇₂₂ and with an approximate Next-to-Next-to-Leading-Order (NNLO) prediction using MSTW2008NNLO.
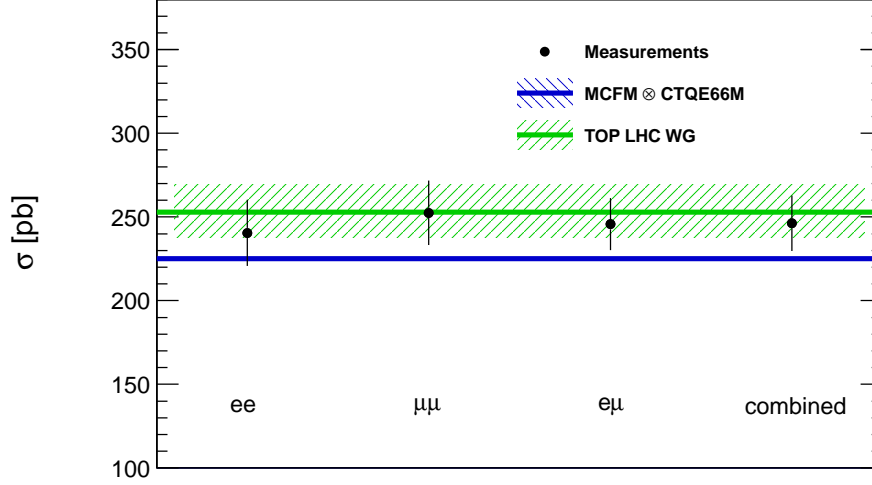
Figure 28: Measured inclusive $t\bar{t}$ quark pair production cross sections in the three dilepton decay channels and their combined value. The measurement is compared to an NLO prediction calculated with MCFM using the CTEQ66M PDF set, and to an approximate NNLO calculation using MSTW2008NNLO.

9.2 Normalised Differential Cross Sections

₇₂₄ The normalised $t\bar{t}$ cross sections are measured differentially as a function of the kinematic prop-
₇₂₅ erties of the leptons, the lepton pairs, the b jets, the top quarks, and the top quark pair as
₇₂₆ described in Section 8.2.

₇₂₇ In each bin of the measurement, the number of signal events after background subtraction
₇₂₈ is corrected for detector efficiencies and acceptances by performing regularized unfolding as
₇₂₉ described above in Section 8. The normalised differential cross section is then derived by di-
₇₃₀ viding the corrected number of events by the bin width and the measured total cross section in
₇₃₁ the same phase space.

₇₃₂ Figures 29 through 44 show the distributions for the following observables: the transverse
₇₃₃ momentum of the leptons p_{T}^{ℓ}, the pseudorapidity of the leptons, η^{ℓ}, the invariant mass of the
₇₃₄ lepton pair, $m^{\ell\ell}$, the transverse momentum of the lepton pair, $p_{\mathrm{T}}^{\ell\ell}$, the transverse momentum
₇₃₅ of the b jets, p_{T}^{b}, the pseudorapidity of the b jets, η^{b}, the transverse momentum of the b-jet
₇₃₆ pair, $p_{\mathrm{T}}^{b\bar{b}}$, the invariant mass of the b-jet pair, $m^{b\bar{b}}$, the invariant mass of the lepton-b-jet system,
₇₃₇ $m^{\ell b}$, the transverse momentum of the top quarks in the laboratory and in the $t\bar{t}$ rest frame
₇₃₈ reference system, p_{T}^{t}, $p_{\mathrm{T}}^{t}(t\bar{t})^{*}$, the rapidity of the top quarks, y^{t}, the difference between the
₇₃₉ absolute rapidities of top and antitop quarks, $|y^{t}| - |y^{\bar{t}}|$, the difference in the azimuthal angle
₇₄₀ between top and antitop quarks, $\Delta\phi(t,\bar{t})$, the transverse momentum of the top-quark pair, $p_{\mathrm{T}}^{t\bar{t}}$,
₇₄₁ the rapidity of the top-quark pair, $y^{t\bar{t}}$, the invariant mass of the top-quark pair, $m^{t\bar{t}}$.

The results are depicted separately for the decay channels $\mu^+\mu^-$ (top row), e^+e^- (2nd row), $\mu^\pm e^\mp$ (3rd row) and their combination (bottom row). For each of these observables the purity, stability and efficiency are shown (left columns). The distributions measured in data are compared with the predictions from Monte Carlo simulations for the $t\bar{t}$ signal and remaining backgrounds (middle column). In general, good agreement is observed between data and simulation. The measured differential cross sections are presented and compared to the expectation from MADGRAPH [6]+PYTHIA [14], POWHEG [8–10]+PYTHIA [14], and MC@NLO [7]+HERWIG [16] (right column). The top-quark-pair invariant mass and transverse momentum distributions are also compared to the latest NLO+NNLL prediction [1, 2]. Additionally, the data are compared with the latest approximate NNLO predictions [3] for the top quark quantities as shown in Figures 38 and 42. The approximate NNLO prediction [3] describes the top p_T spectrum in data better than the other predictions. To understand if the preference of the data with respect to higher order predictions, in top quark distributions, is biased due to an experimental effect, the analysis is repeated by modifying some selection criteria. Results (considering only the statistical error) for the combination of e^+e^-, $\mu^\pm e^\mp$ and $\mu^+\mu^-$ channels are shown in Appendix C together with the yield plots. No significant change is observed.

In general, good agreement is found within uncertainties between the data and the theory predictions, both for the individual channels and for their combination. All measured cross section values, including bin boundaries, are listed in the Tables 10 to 17.
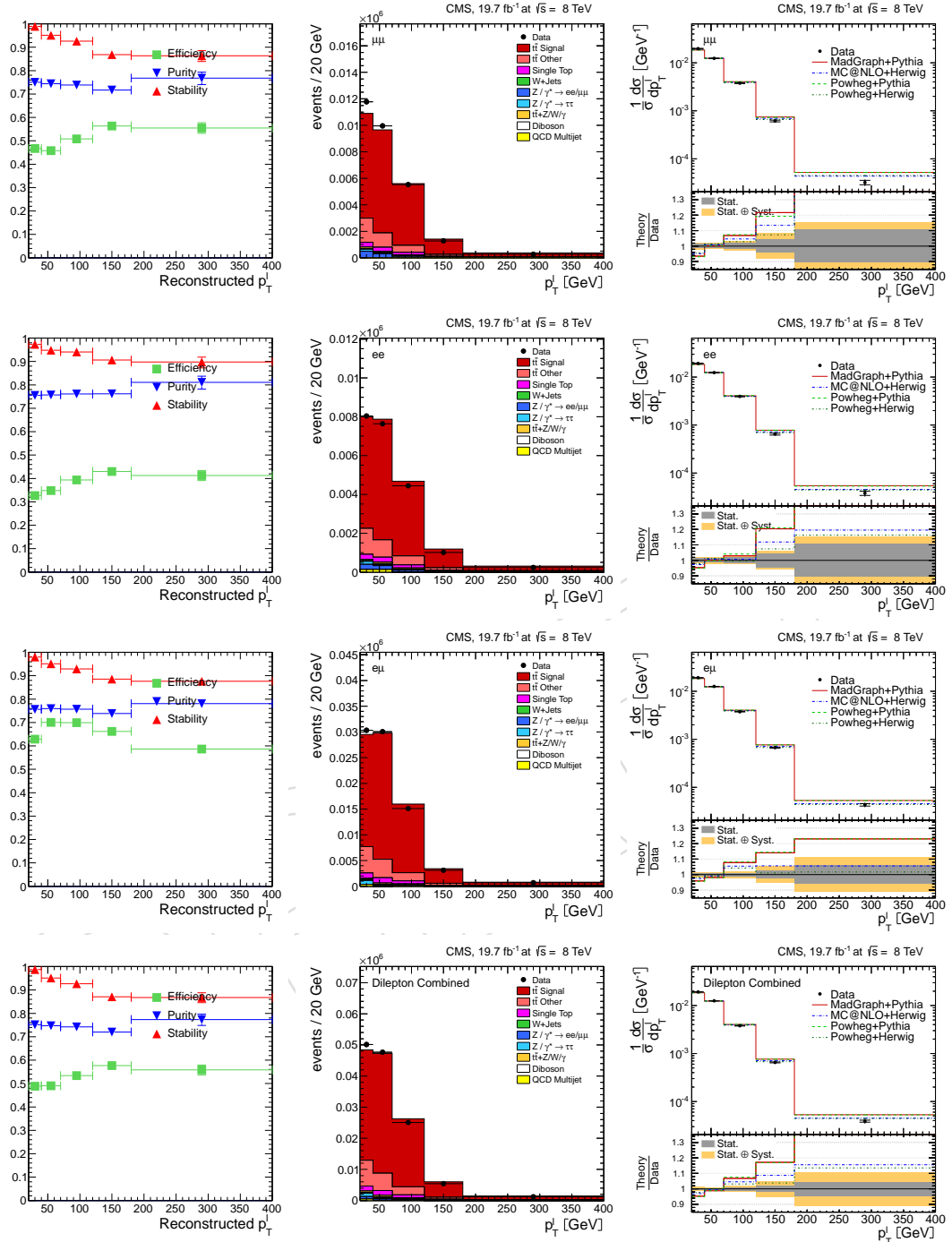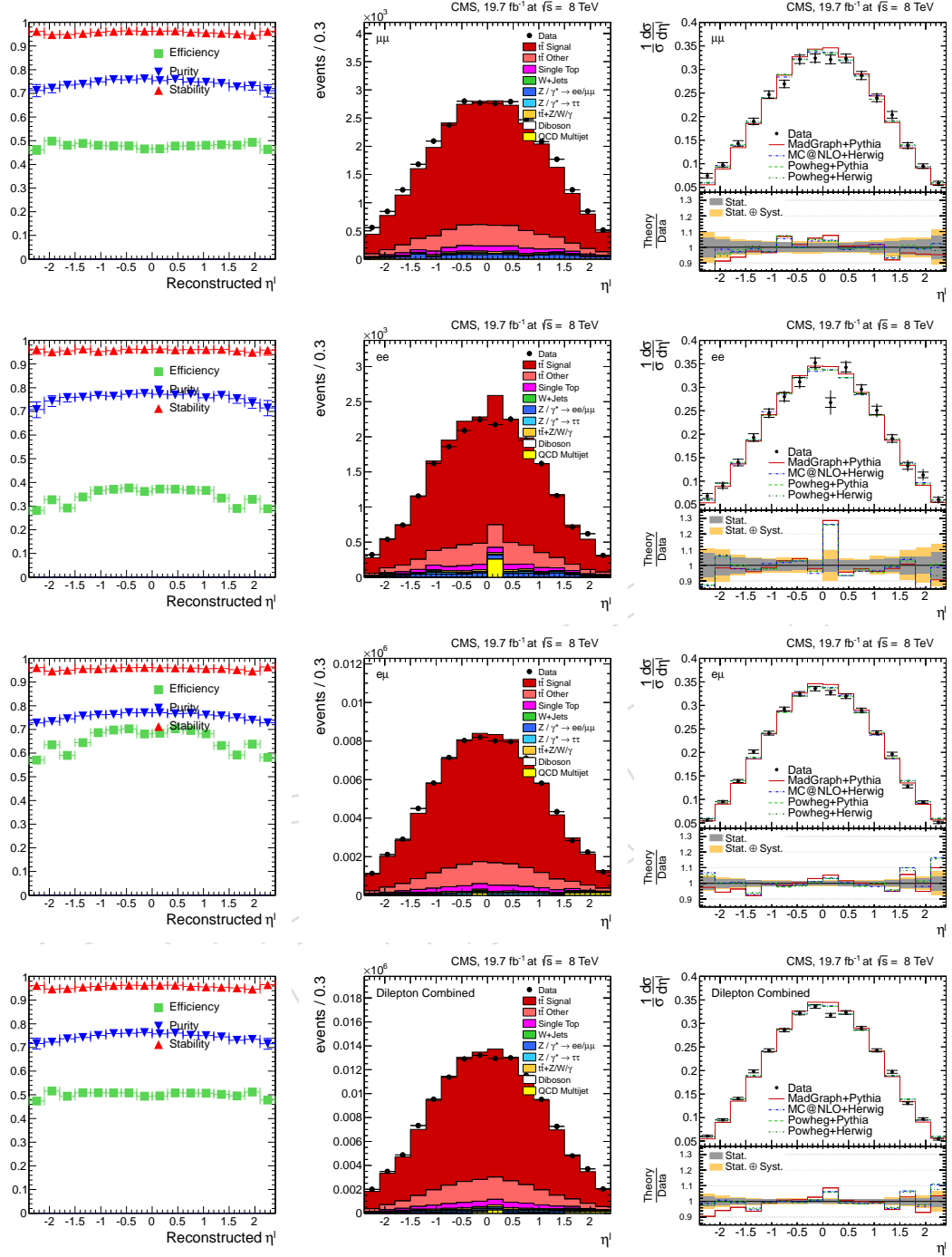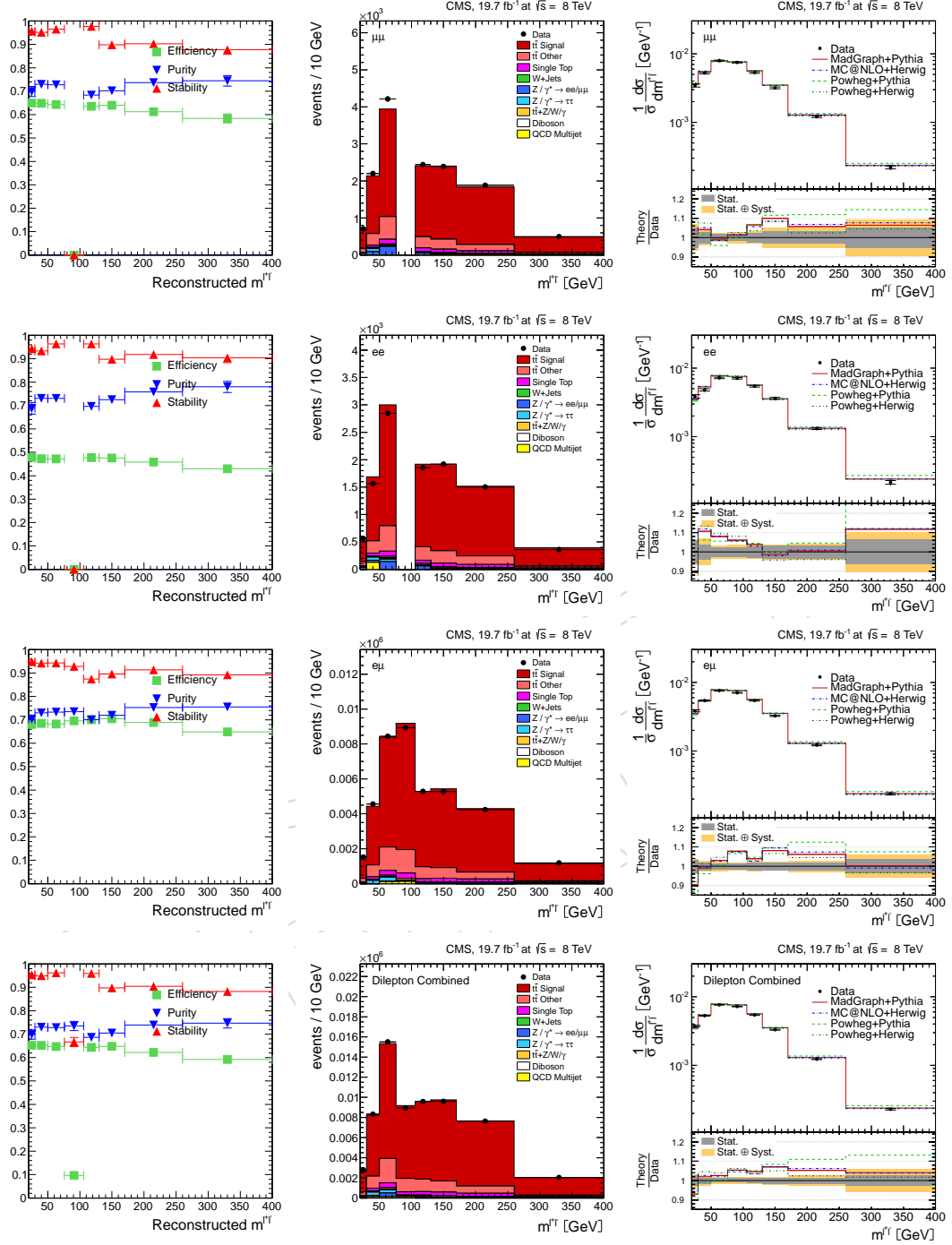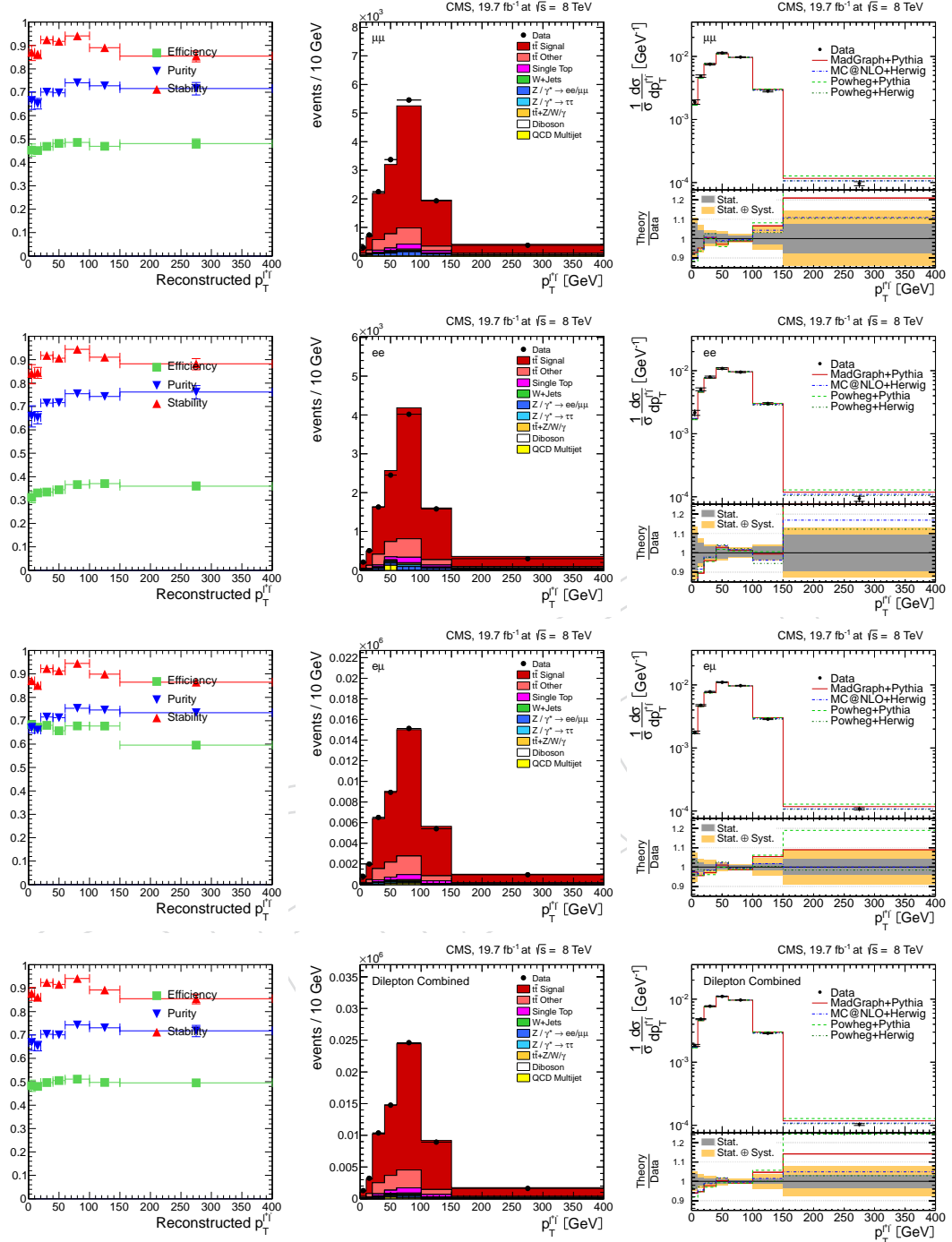
Figure 29: Differential $t\bar{t}$ production cross section (right column) as a function of the transverse momentum of the leptons for the three decay channels $\mu^+\mu^-$ (top), e^+e^- (2nd row) and $\mu^\pm e^\mp$ (3rd row) and combined (bottom). The inner error bar shows the statistical error, the outer error bars statistical and systematic errors added in quadrature. The measurements are compared to the predictions from MADGRAPH [6]+PYTHIA [14], POWHEG [8–10]+PYTHIA [14], and MC@NLO [7]+HERWIG [16]. In the left column the reconstruction efficiency, purity and stability are shown. The middle column shows the number of events in data and simulation.

Figure 30: Differential $t\bar{t}$ production cross section (right column) as a function of the pseudorapidity of the leptons for the three decay channels $\mu^+\mu^-$ (top), e^+e^- (2nd row) and $\mu^\pm e^\mp$ (3rd row) and combined (bottom). The inner error bar shows the statistical error, the outer error bars statistical and systematic errors added in quadrature. The measurements are compared to the predictions from MAD-GRAPH [6]+PYTHIA [14], POWHEG [8–10]+PYTHIA [14], and MC@NLO [7]+HERWIG [16]. In the left column the reconstruction efficiency, purity and stability are shown. The middle column shows the number of events in data and simulation.
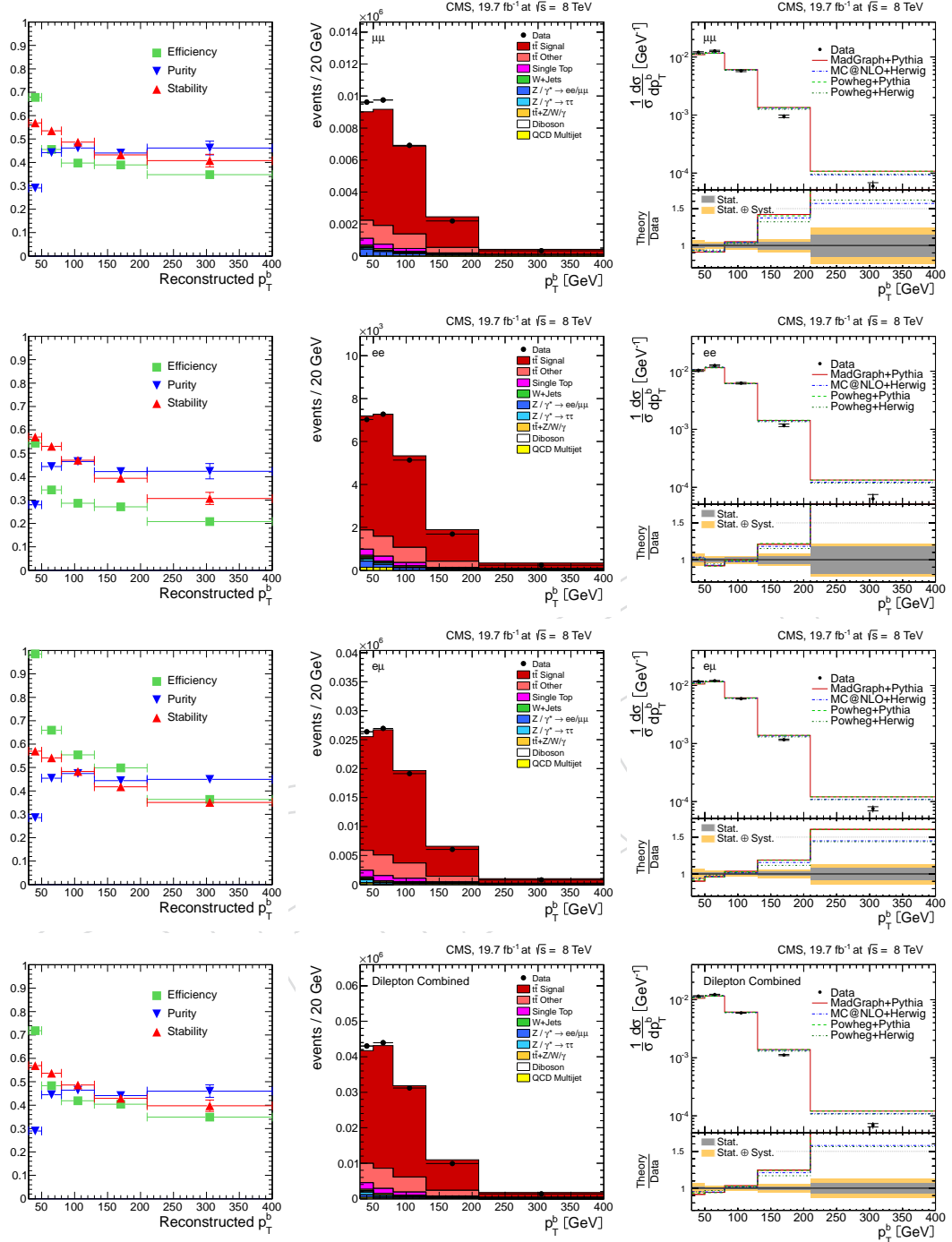
Figure 31: Differential $t\bar{t}$ production cross section (right column) as a function of the invariant mass of the lepton-pair system for the three decay channels $\mu^+\mu^-$ (top), e^+e^- (2nd row) and $\mu^\pm e^\mp$ (3rd row) and combined (bottom). The inner error bar shows the statistical error, the outer error bars statistical and systematic errors added in quadrature. The measurements are compared to the predictions from MADGRAPH [6]+PYTHIA [14], POWHEG [8–10]+PYTHIA [14], and MC@NLO [7]+HERWIG [16]. In the left column the reconstruction efficiency, purity and stability are shown. The middle column shows the number of events in data and simulation. For the $\mu^+\mu^-$ and e^+e^- channels, no measurement is available in the Z veto region $76\,\text{GeV} < m^{\ell\ell} < 106\,\text{GeV}$.

Figure 32: Differential $t\bar{t}$ production cross section (right column) as a function of the transverse momentum of the lepton-pair system for the three decay channels $\mu^+\mu^-$ (top), e^+e^- (2nd row) and $\mu^\pm e^\mp$ (3rd row) and combined (bottom). The inner error bar shows the statistical error, the outer error bars statistical and systematic errors added in quadrature. The measurements are compared to the predictions from MADGRAPH [6]+PYTHIA [14], POWHEG [8–10]+PYTHIA [14], and MC@NLO [7]+HERWIG [16] In the left column the reconstruction efficiency, purity and stability are shown. The middle column shows the number of events in data and simulation.

Figure 33: Differential $t\bar{t}$ production cross section (right column) as a function of the transverse momentum of the b-jets for the three decay channels $\mu^+\mu^-$ (top), e^+e^- (2nd row) and $\mu^\pm e^\mp$ (3rd row) and combined (bottom). The inner error bar shows the statistical error, the outer error bars statistical and systematic errors added in quadrature. The measurements are compared to the predictions from MADGRAPH [6]+PYTHIA [14], POWHEG [8–10]+PYTHIA [14], and MC@NLO [7]+HERWIG [16] In the left column the reconstruction efficiency, purity and stability are shown. The middle column shows the number of events in data and simulation.
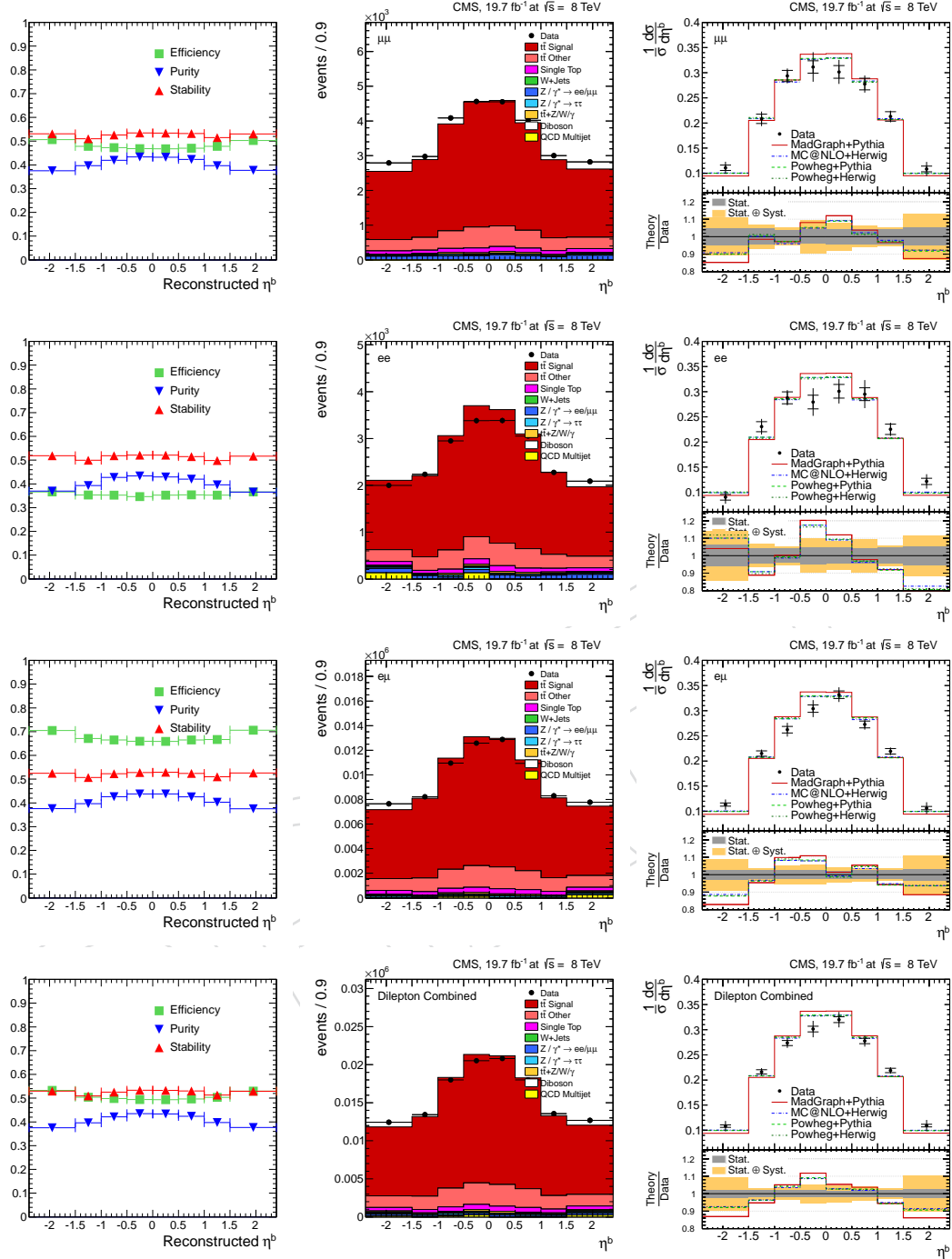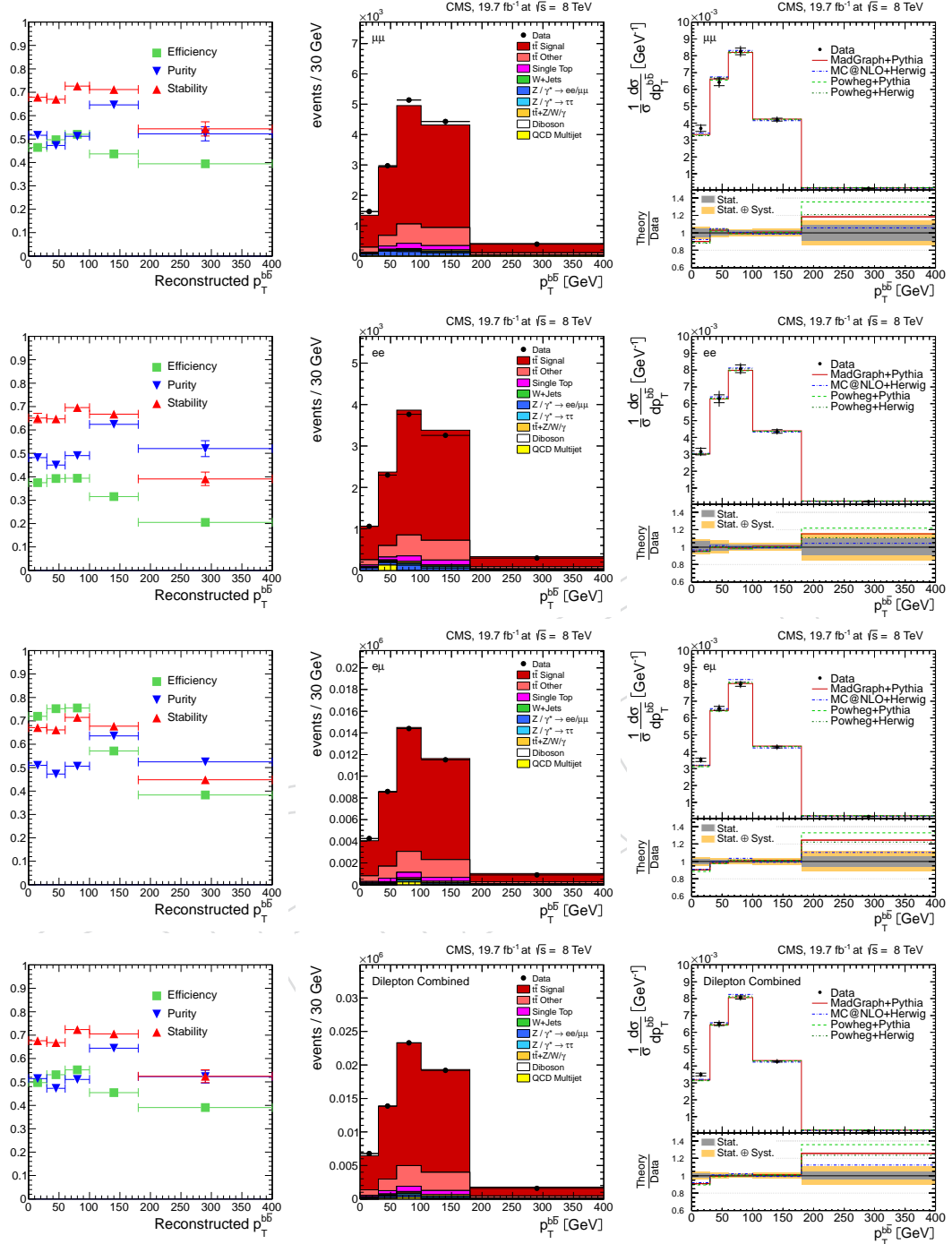
Figure 34: Differential $t\bar{t}$ production cross section (right column) as a function of the pseudorapidity of the b-jets for the three decay channels $\mu^+\mu^-$ (top), e^+e^- (2nd row) and $\mu^\pm e^\mp$ (3rd row) and combined (bottom). The inner error bar shows the statistical error, the outer error bars statistical and systematic errors added in quadrature. The measurements are compared to the predictions from MADGRAPH [6]+PYTHIA [14], POWHEG [8–10]+PYTHIA [14], and MC@NLO [7]+HERWIG [16] In the left column the reconstruction efficiency, purity and stability are shown. The middle column shows the number of events in data and simulation.
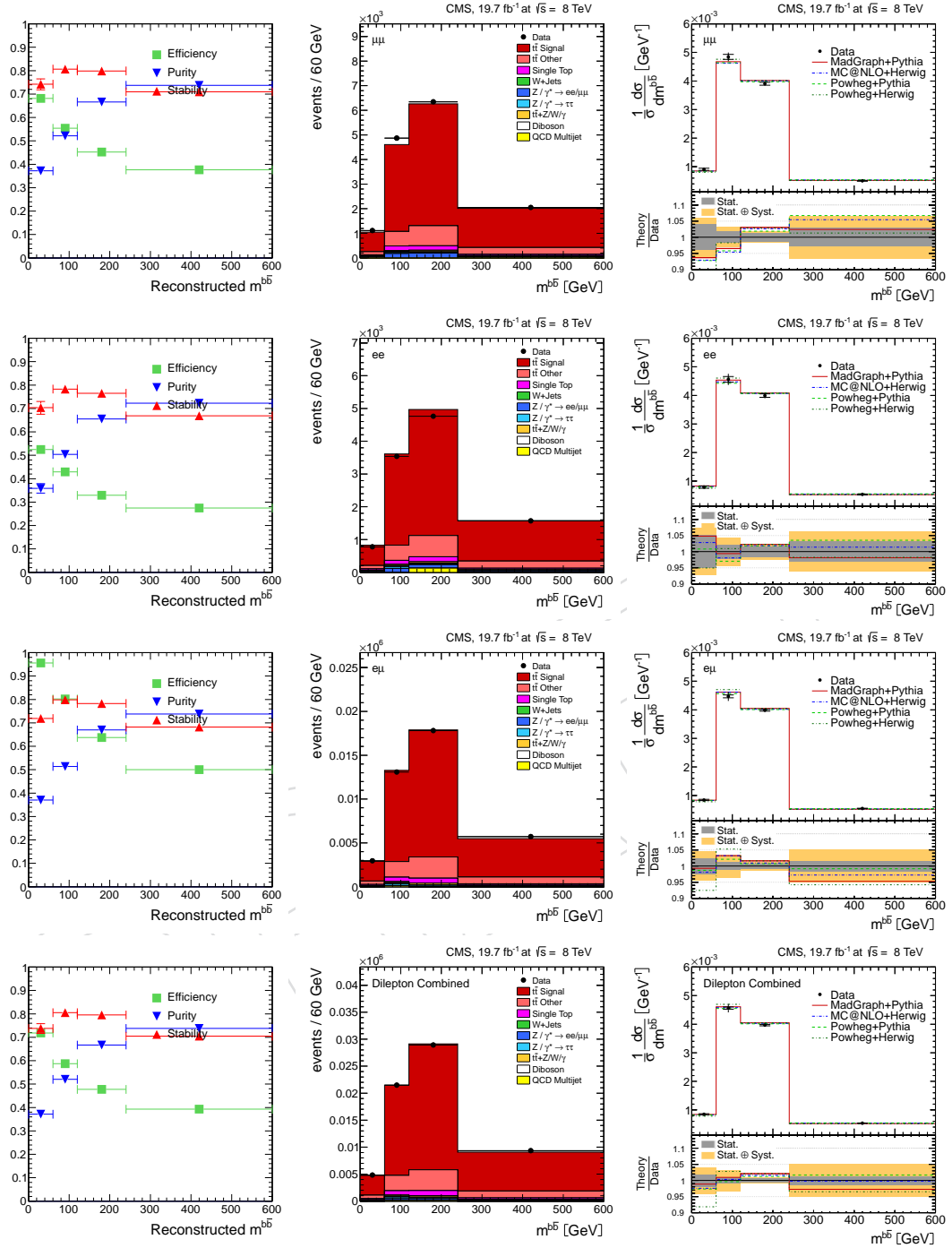
Figure 35: Differential $t\bar{t}$ production cross section (right column) as a function of the transverse momentum of the $b\bar{b}$ system for the three decay channels $\mu^+\mu^-$ (top), e^+e^- (2nd row) and $\mu^\pm e^\mp$ (3rd row) and combined (bottom). The inner error bar shows the statistical error, the outer error bars statistical and systematic errors added in quadrature. The measurements are compared to the predictions from MADGRAPH [6]+PYTHIA [14], POWHEG [8–10]+PYTHIA [14], and MC@NLO [7]+HERWIG [16] In the left column the reconstruction efficiency, purity and stability are shown. The middle column shows the number of events in data and simulation.
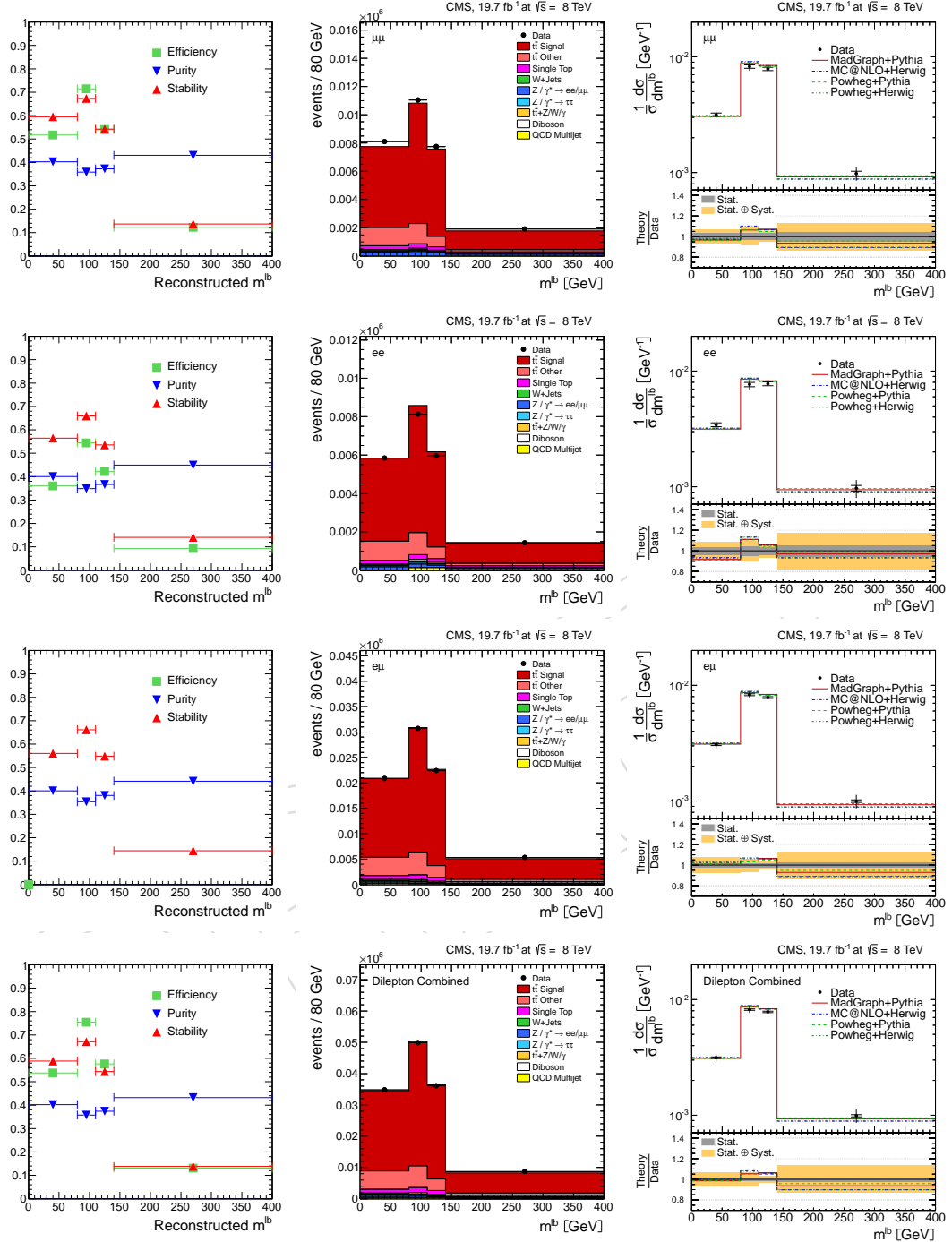
Figure 36: Differential $t\bar{t}$ production cross section (right column) as a function of the invariant mass of the $b\bar{b}$ system for the three decay channels $\mu^+\mu^-$ (top), e^+e^- (2nd row) and $\mu^\pm e^\mp$ (3rd row) and combined (bottom). The inner error bar shows the statistical error, the outer error bars statistical and systematic errors added in quadrature. The measurements are compared to the predictions from MAD-GRAPH [6]+PYTHIA [14], POWHEG [8–10]+PYTHIA [14], and MC@NLO [7]+HERWIG [16] In the left column the reconstruction efficiency, purity and stability are shown. The middle column shows the number of events in data and simulation.
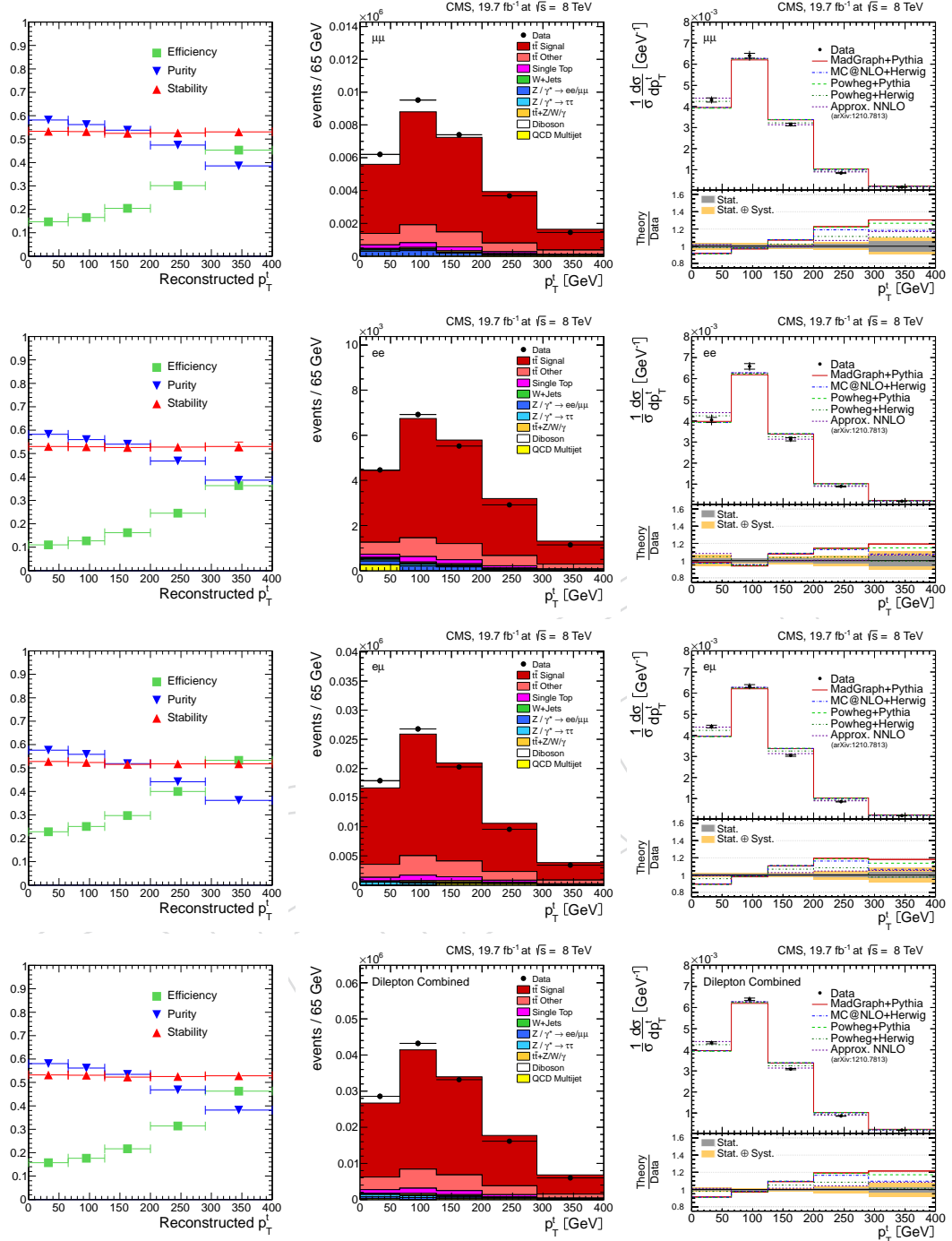
Figure 37: Differential $t\bar{t}$ production cross section (right column) as a function of the invariant mass of the lepton-b-jet system for the three decay channels $\mu^+\mu^-$ (top), e^+e^- (2nd row) and $\mu^\pm e^\mp$ (3rd row) and combined (bottom). The inner error bar shows the statistical error, the outer error bars statistical and systematic errors added in quadrature. The measurements are compared to the predictions from MADGRAPH [6]+PYTHIA [14], POWHEG [8–10]+PYTHIA [14], and MC@NLO [7]+HERWIG [16] In the left column the reconstruction efficiency, purity and stability are shown. The middle column shows the number of events in data and simulation.

Figure 38: Differential $t\bar{t}$ production cross section (right column) as a function of the transverse momentum of the p_T top quark for the three decay channels $\mu^+\mu^-$ (top), e^+e^- (2nd row) and $\mu^\pm e^\mp$ (3rd row) and combined (bottom). The inner error bar shows the statistical error, the outer error bars statistical and systematic errors added in quadrature. The measurements are compared to the predictions from MADGRAPH [6]+PYTHIA [14], POWHEG [8–10]+PYTHIA [14], MC@NLO [7]+HERWIG [16], and an approximate NNLO calculation [3] In the left column the reconstruction efficiency, purity and stability are shown. The middle column shows the number of events in data and simulation.
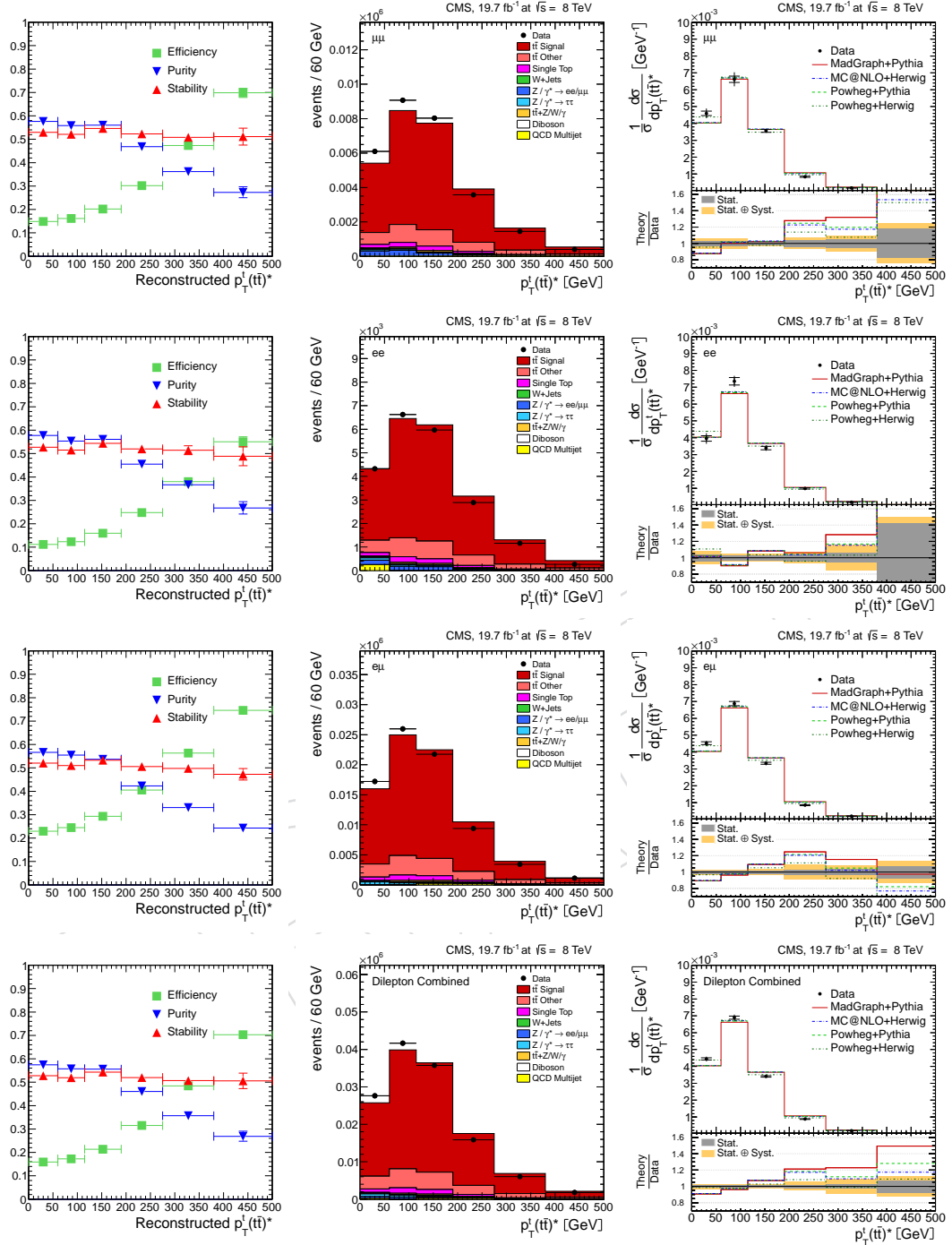
Figure 39: Differential $t\bar{t}$ production cross section (right column) as a function of the transverse momentum of the p_T top quark, measured in the $t\bar{t}$ system rest frame, for the three decay channels $\mu^+\mu^-$ (top), e^+e^- (2nd row) and $\mu^\pm e^\mp$ (3rd row) and combined (bottom). The inner error bar shows the statistical error, the outer error bars statistical and systematic errors added in quadrature. The measurements are compared to the predictions from MADGRAPH [6]+PYTHIA [14], POWHEG [8–10]+PYTHIA [14], MC@NLO [7]+HERWIG [16], and an approximate NNLO calculation [3] In the left column the reconstruction efficiency, purity and stability are shown. The middle column shows the number of events in data and simulation.
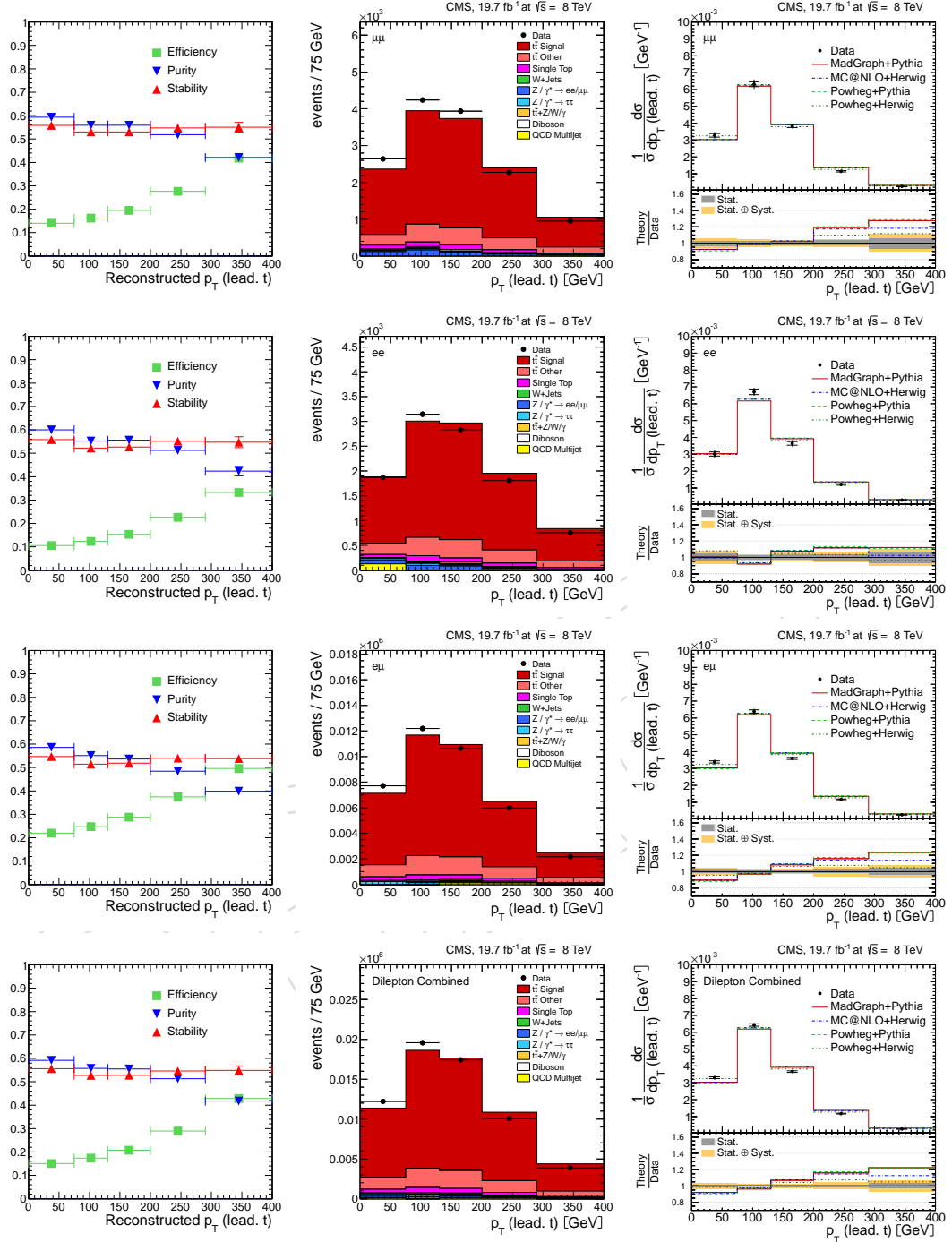
Figure 40: Differential $t\bar{t}$ production cross section (right column) as a function of the transverse momentum of the first leading p_T top quark for the three decay channels $\mu^+\mu^-$ (top), e^+e^- (2nd row) and $\mu^\pm e^\mp$ (3rd row) and combined (bottom). The inner error bar shows the statistical error, the outer error bars statistical and systematic errors added in quadrature. The measurements are compared to the predictions from MADGRAPH [6]+PYTHIA [14], POWHEG [8–10]+PYTHIA [14], MC@NLO [7]+HERWIG [16], and an approximate NNLO calculation [3] In the left column the reconstruction efficiency, purity and stability are shown. The middle column shows the number of events in data and simulation.
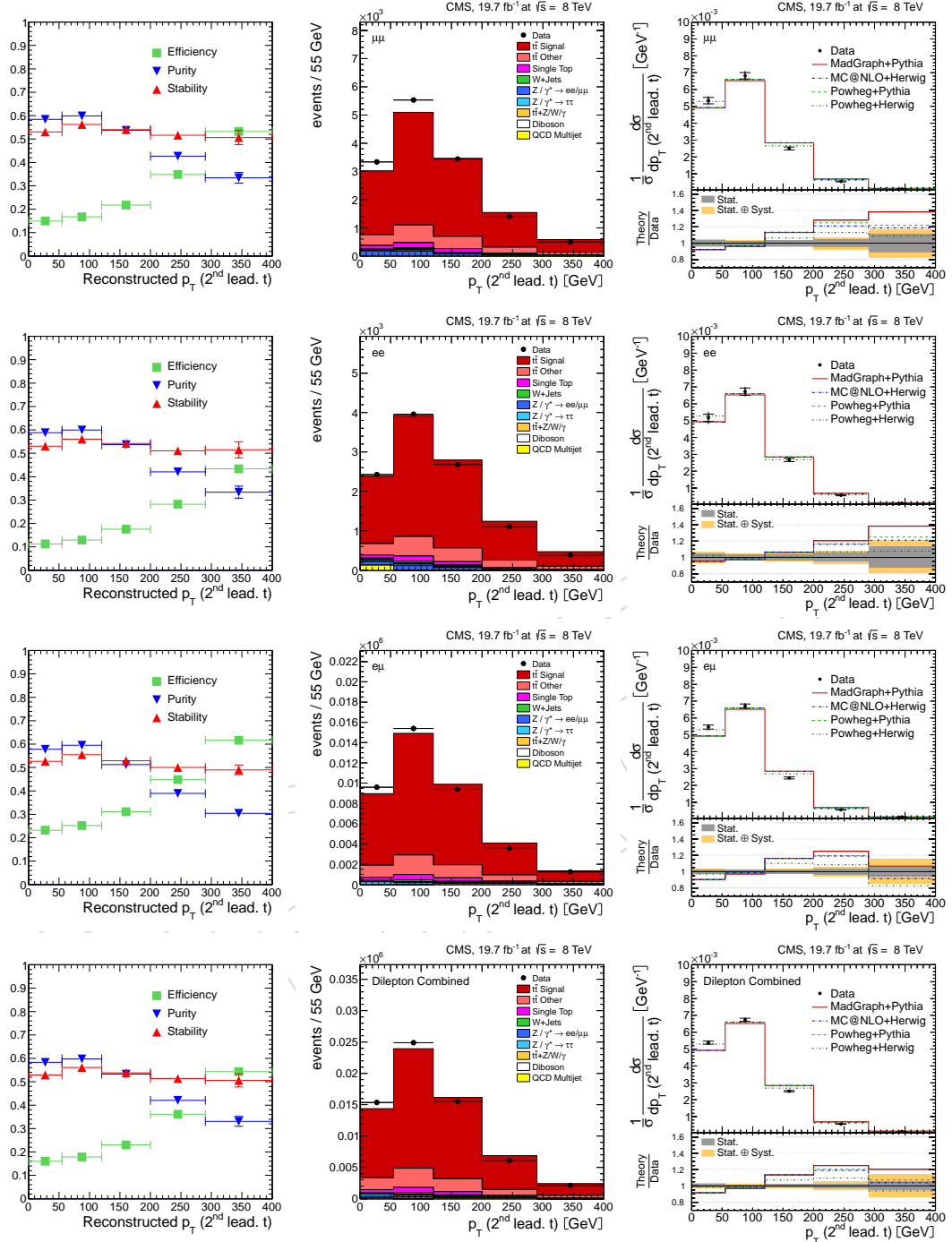
Figure 41: Differential $t\bar{t}$ production cross section (right column) as a function of the transverse momentum of the second leading p_T top quark for the three decay channels $\mu^+\mu^-$ (top), e^+e^- (2nd row) and $\mu^\pm e^\mp$ (3rd row) and combined (bottom). The inner error bar shows the statistical error, the outer error bars statistical and systematic errors added in quadrature. The measurements are compared to the predictions from MADGRAPH [6]+PYTHIA [14], POWHEG [8–10]+PYTHIA [14], MC@NLO [7]+HERWIG [16], and an approximate NNLO calculation [3] In the left column the reconstruction efficiency, purity and stability are shown. The middle column shows the number of events in data and simulation.
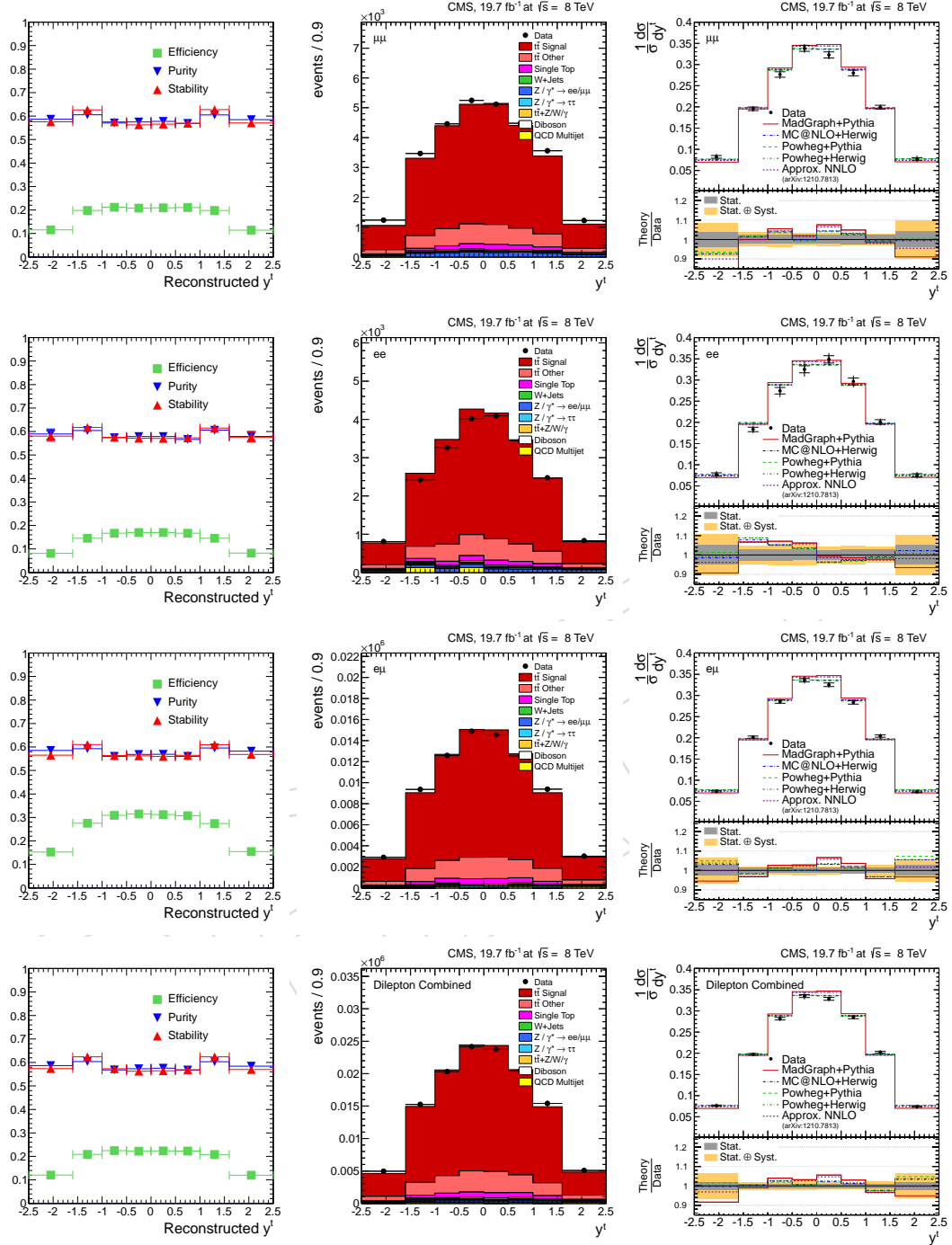
Figure 42: Differential $t\bar{t}$ production cross section (right column) as a function of the rapidity of the top quark for the three decay channels $\mu^+\mu^-$ (top), e^+e^- (2nd row) and $\mu^\pm e^\mp$ (3rd row) and combined (bottom). The inner error bar shows the statistical error, the outer error bars statistical and systematic errors added in quadrature. The measurements are compared to the predictions from MAD-GRAPH [6]+PYTHIA [14], POWHEG [8–10]+PYTHIA [14], MC@NLO [7]+HERWIG [16] and an approximate NNLO calculation [3] In the left column the reconstruction efficiency, purity and stability are shown. The middle column shows the number of events in data and simulation.
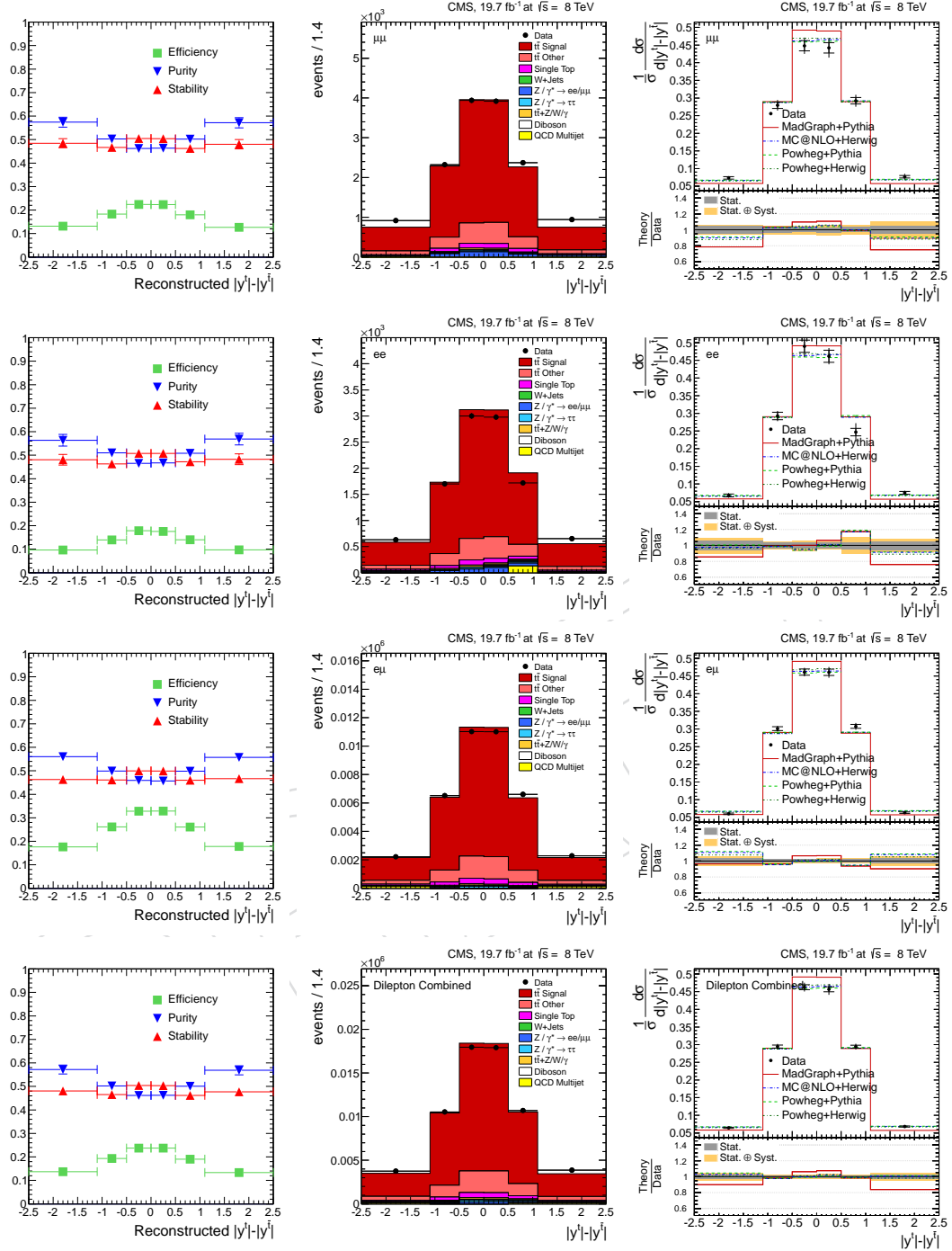
Figure 43: Differential $t\bar{t}$ production cross section (right column) as a function of $|y^t| - |y^{\bar{t}}|$ of the top-quarks for the three decay channels $\mu^+\mu^-$ (top), e^+e^- (2nd row) and $\mu^\pm e^\mp$ (3rd row) and combined (bottom). The inner error bar shows the statistical error, the outer error bars statistical and systematic errors added in quadrature. The measurements are compared to the predictions from MAD-GRAPH [6]+PYTHIA [14], POWHEG [8–10]+PYTHIA [14], and MC@NLO [7]+HERWIG [16] In the left column the reconstruction efficiency, purity and stability are shown. The middle column shows the number of events in data and simulation.
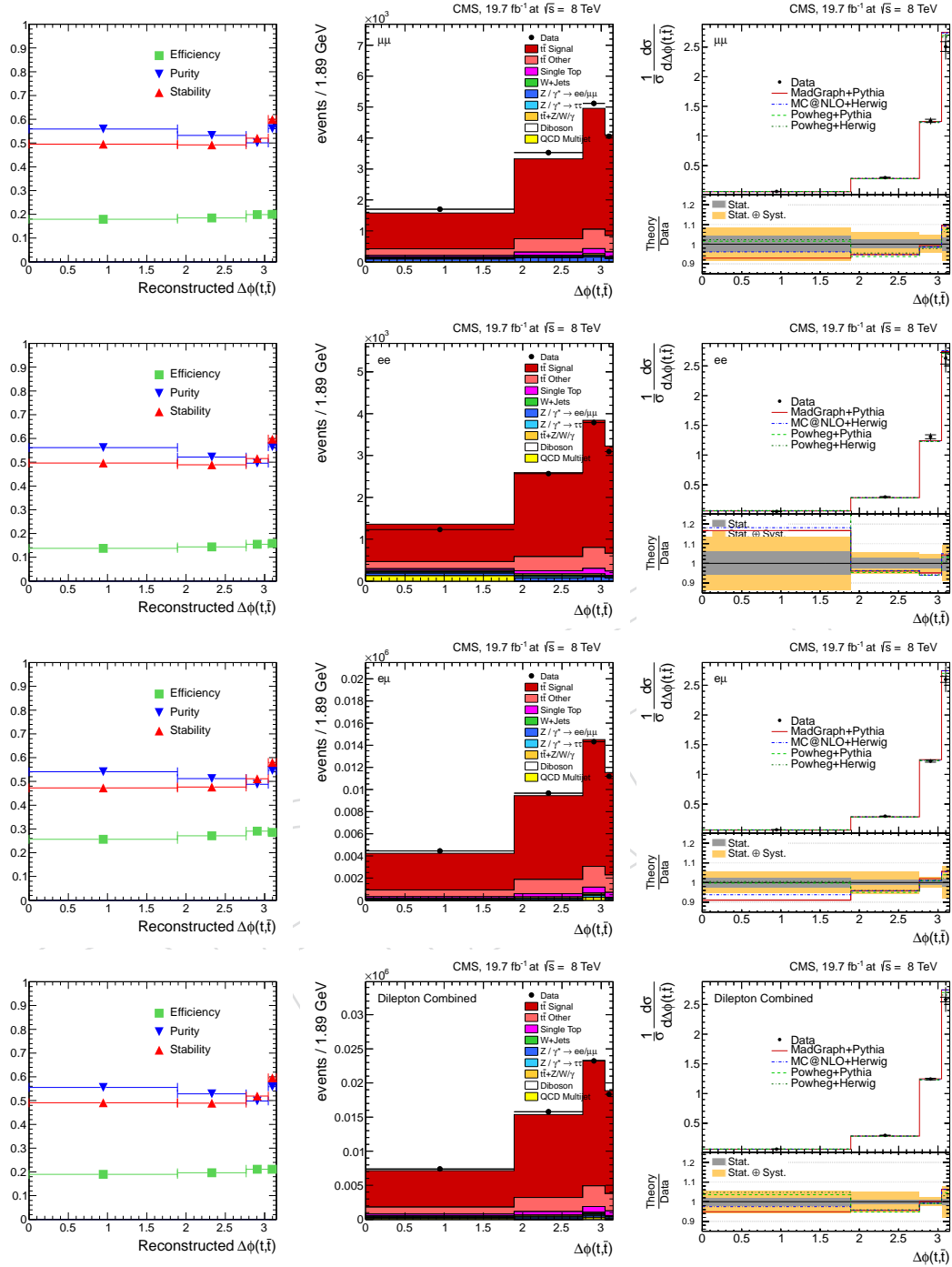
Figure 44: Differential $t\bar{t}$ production cross section (right column) as a function of $\Delta\phi$ of the $t\bar{t}$ system for the three decay channels $\mu^+\mu^-$ (top), e^+e^- (2nd row) and $\mu^{\pm}e^{\mp}$ (3rd row) and combined (bottom). The inner error bar shows the statistical error, the outer error bars statistical and systematic errors added in quadrature. The measurements are compared to the predictions from MADGRAPH [6]+PYTHIA [14], POWHEG [8–10]+PYTHIA [14], and MC@NLO [7]+HERWIG [16] In the left column the reconstruction efficiency, purity and stability are shown. The middle column shows the number of events in data and simulation.
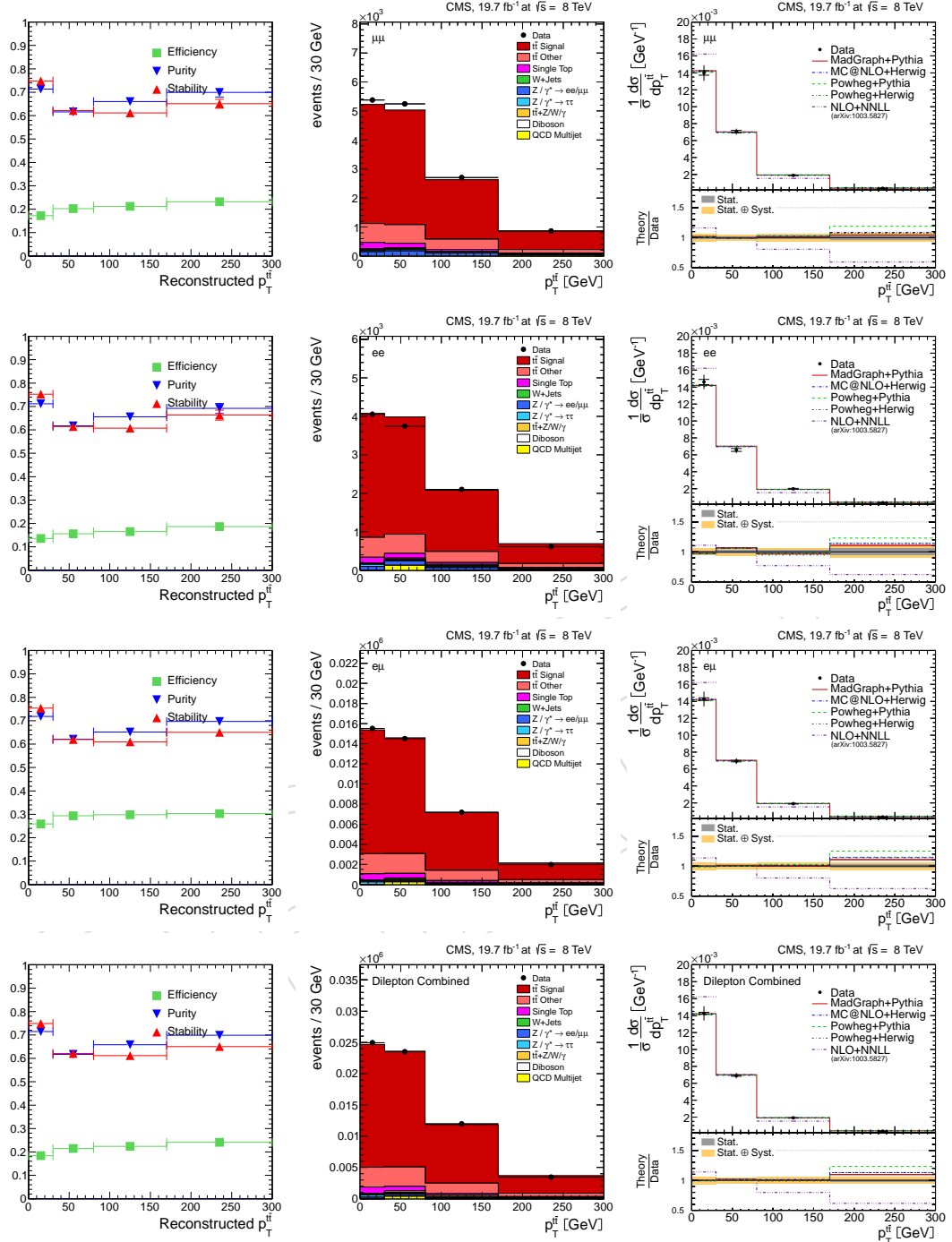
Figure 45: Differential $t\bar{t}$ production cross section (right column) as a function of the transverse momentum of the $t\bar{t}$ quark pair for the three decay channels $\mu^+\mu^-$ (top), e^+e^- (2nd row) and $\mu^\pm e^\mp$ (3rd row) and combined (bottom). The inner error bar shows the statistical error, the outer error bars statistical and systematic errors added in quadrature. The measurements are compared to the predictions from MADGRAPH [6]+PYTHIA [14], POWHEG [8–10]+PYTHIA [14], MC@NLO [7]+HERWIG [16], and the latest NLO+NNLL theory prediction [2] In the left column the reconstruction efficiency, purity and stability are shown. The middle column shows the number of events in data and simulation.
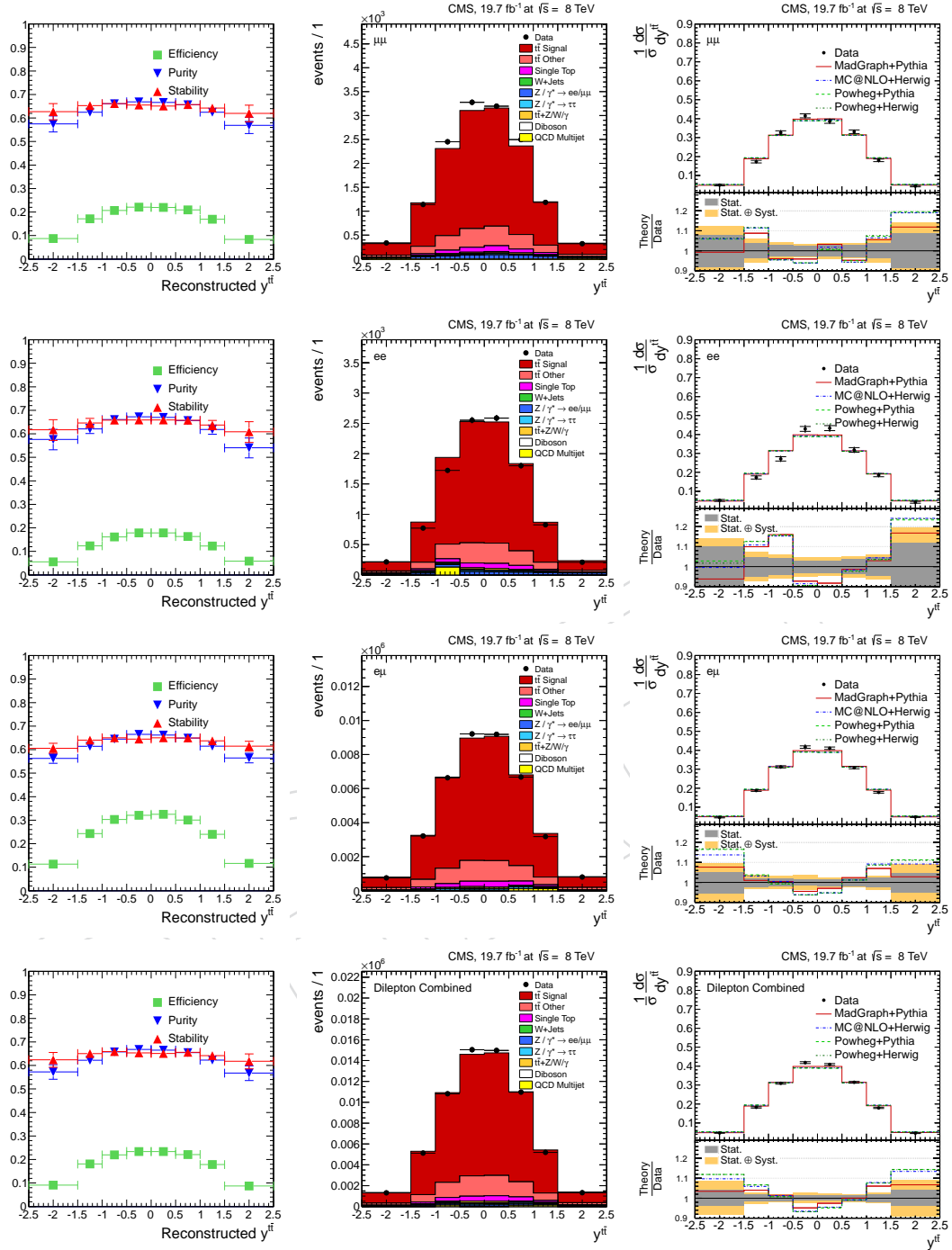
Figure 46: Differential $t\bar{t}$ production cross section (right column) as a function of the rapidity of the $t\bar{t}$ system for the three decay channels $\mu^+\mu^-$ (top), e^+e^- (2nd row) and $\mu^\pm e^\mp$ (3rd row) and combined (bottom). The inner error bar shows the statistical error, the outer error bars statistical and systematic errors added in quadrature. The measurements are compared to the predictions from MAD-GRAPH [6]+PYTHIA [14], POWHEG [8–10]+PYTHIA [14], and MC@NLO [7]+HERWIG [16] In the left column the reconstruction efficiency, purity and stability are shown. The middle column shows the number of events in data and simulation.
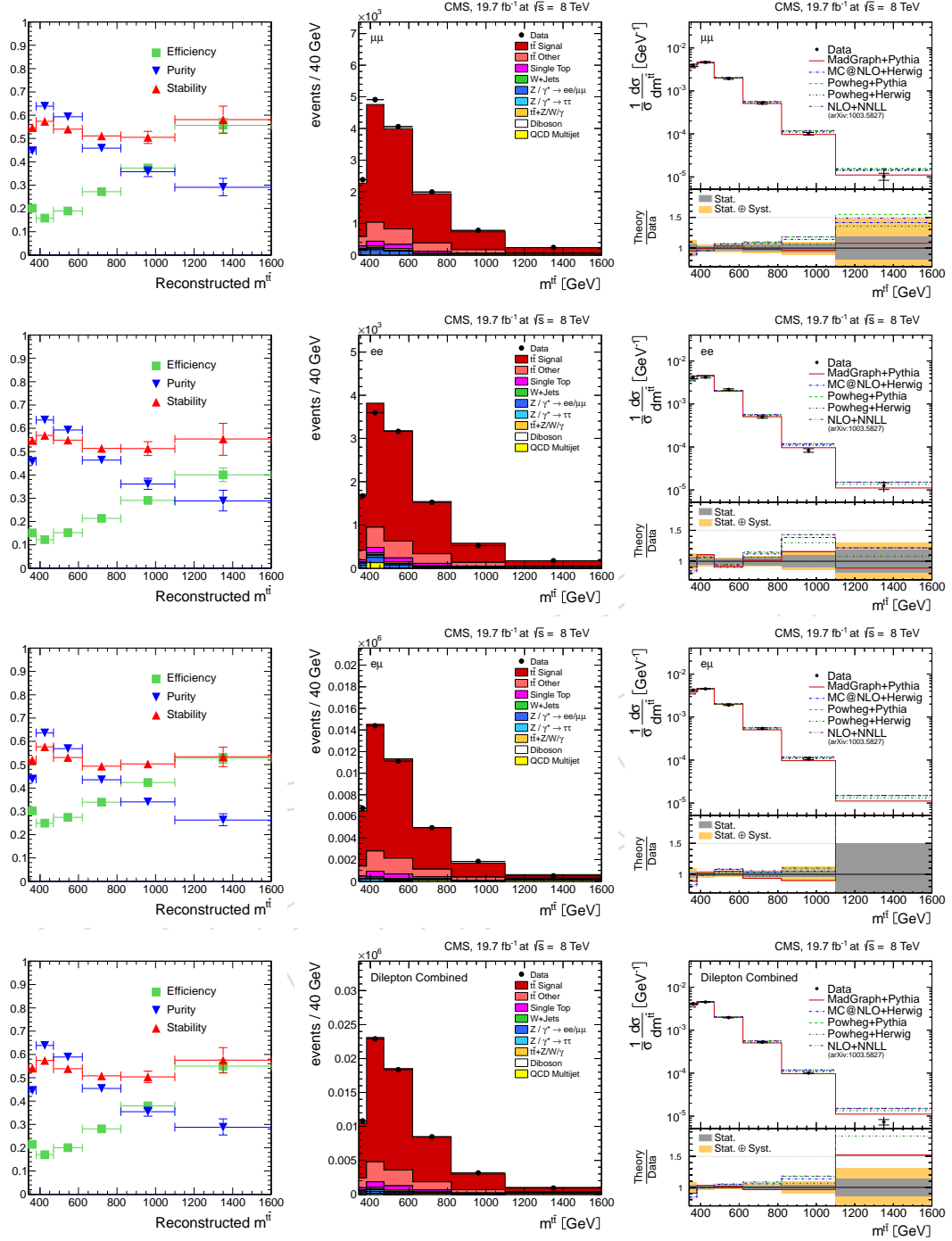
Figure 47: Differential $t\bar{t}$ production cross section (right column) as a function of the invariant mass of the $t\bar{t}$ system for the three decay channels $\mu^+\mu^-$ (top), e^+e^- (2nd row) and $\mu^\pm e^\mp$ (3rd row) and combined (bottom). The inner error bar shows the statistical error, the outer error bars statistical and systematic errors added in quadrature. The measurements are compared to the predictions from MADGRAPH [6]+PYTHIA [14], POWHEG [8–10]+PYTHIA [14], MC@NLO [7]+HERWIG [16] and the latest NLO+NNLL theory prediction [1] In the left column the reconstruction efficiency, purity and stability are shown. The middle column shows the number of events in data and simulation.

Table 10: Normalised differential cross section as a function of the leptons observables: the transverse momentum (p_T^l) and the pseudorapidity (η^l).

bin-center [GeV]	bin [GeV]	$1/\sigma d\sigma/dp_T^l$	stat. [%]	sys. [%]	total [%]
30	20 to 40	0.019327	0.531	1.33	1.43
55	40 to 70	0.012532	0.54	0.684	0.871
95	70 to 120	0.00379	0.849	1.7	1.9
150	120 to 180	0.00065105	1.96	4.79	5.17
290	180 to 400	3.8856e-05	4.61	9.75	10.8
bin-center	bin	$1/\sigma d\sigma/d\eta^l$	stat. [%]	sys. [%]	total [%]
-2.25	-2.4 to -2.1	0.060426	3.02	3.86	4.9
-1.95	-2.1 to -1.8	0.094923	2.25	2.73	3.54
-1.65	-1.8 to -1.5	0.14009	1.88	1.41	2.35
-1.35	-1.5 to -1.2	0.19801	1.54	1.44	2.11
-1.05	-1.2 to -0.9	0.24261	1.41	0.635	1.55
-0.75	-0.9 to -0.6	0.28584	1.23	1.35	1.83
-0.45	-0.6 to -0.3	0.32214	1.18	1.32	1.77
-0.15	-0.3 to 0	0.33592	1.15	0.704	1.35
0.15	0 to 0.3	0.31734	1.23	1.34	1.82
0.45	0.3 to 0.6	0.32346	1.22	1.15	1.68
0.75	0.6 to 0.9	0.29011	1.27	1.15	1.71
1.05	0.9 to 1.2	0.24274	1.41	1.02	1.74
1.35	1.2 to 1.5	0.19702	1.57	1.99	2.54
1.65	1.5 to 1.8	0.13048	2.11	2.33	3.14
1.95	1.8 to 2.1	0.097032	2.31	3.07	3.84
2.25	2.1 to 2.4	0.0538	3.53	5.35	6.41

10   Conclusions

A measurement of the $t\bar{t}$ quark pair production cross section in pp collisions at $\sqrt{s} = 8$ TeV has been presented using the decay channels into two opposite-sign leptons (electrons or muons) in the final state.

Both the absolute inclusive cross section and normalised differential cross sections are measured. The measurements in the different decay channels are found to agree with each other and with theoretical expectations from Standard Model predictions, and only small differences between the different theory predictions are observed. The total inclusive $t\bar{t}$ production cross section is measured to be $\sigma_{t\bar{t}} = 245.10 \pm 1.05(stat.) \pm 14.25(syst.) \pm 14.29(total)$ pb. The invariant mass spectrum of the $t\bar{t}$ system is also measured and found to agree well with expectations. At the present level of precision, no hints for new phenomena are visible.

11   To-do list

12   Updates since AN-13-266-v12

- Add $t\bar{t} + Z/W/\gamma$ background contribution
- Added MVA Met reconstruction and hadronic recoil correction
- Added systematic uncertainty tables differential results

Table 11: Normalised differential cross section as a function of lepton observables: the transverse momentum of the lepton pair $p_T^{\ell\ell}$, and the invariant mass of the lepton pair $m^{\ell\ell}$.

bin-center [GeV]	bin [GeV]	$1/\sigma d\sigma/dp_T^{\ell\ell}$	stat. [%]	sys. [%]	total [%]
5	0 to 10	0.0018433	3.69	3.28	4.93
15	10 to 20	0.0048201	2.01	3.01	3.63
30	20 to 40	0.0077425	1.24	2.66	2.93
50	40 to 60	0.011031	1.05	1.67	1.97
80	60 to 100	0.0097039	0.697	0.945	1.17
125	100 to 150	0.0028721	1.29	3.64	3.86
275	150 to 400	0.00010327	3.35	7.04	7.8
bin-center [GeV]	bin [GeV]	$1/\sigma d\sigma/dm^{\ell\ell}$	stat. [%]	sys. [%]	total [%]
25	20 to 30	0.0037405	2.57	2	3.25
40	30 to 50	0.0052811	1.47	2.03	2.51
63	50 to 76	0.0076112	1	1.3	1.64
91	76 to 106	0.0071942	1	1.48	1.79
118	106 to 130	0.0054083	1.34	1.2	1.8
150	130 to 170	0.0032979	1.43	1.5	2.07
215	170 to 260	0.0012315	1.48	2.32	2.75
330	260 to 400	0.00022918	2.65	5.21	5.84

Table 12: Normalised differential cross section as a function of the b-jets observables: the transverse momentum (p_T^b) and the pseudorapidity (η^b).

bin-center [GeV]	bin [GeV]	$1/\sigma d\sigma/p_T^b$	stat. [%]	sys. [%]	total [%]
40	30 to 50	0.011554	1.25	6.26	6.38
65	50 to 80	0.012293	1.18	2.96	3.18
105	80 to 130	0.005936	1.4	3.23	3.52
170	130 to 210	0.0011115	2.23	5.36	5.8
305	210 to 400	6.8778e-05	6.82	10.9	12.9
bin-center	bin	$1/\sigma d\sigma/\eta^b$	stat. [%]	sys. [%]	total [%]
−1.95	−2.4 to −1.5	0.10817	2.27	9.33	9.6
−1.25	−1.5 to −1	0.21621	1.96	2.73	3.36
−0.75	−1 to −0.5	0.27357	1.86	3.05	3.57
−0.25	−0.5 to 0	0.30135	1.89	5.1	5.44
0.25	0 to 0.5	0.31987	1.81	4.43	4.79
0.75	0.5 to 1	0.27757	1.92	3.56	4.04
1.25	1 to 1.5	0.21895	1.97	2.13	2.91
1.95	1.5 to 2.4	0.10938	2.38	10.1	10.4

Table 13: Normalised differential cross section as a function of the $b\bar{b}$ system observables: the transverse momentum ($p_T^{b\bar{b}}$) and invariant mass ($m^{b\bar{b}}$).

bin-center [GeV]	bin [GeV]	$1/\sigma d\sigma / p_T^{b\bar{b}}$	stat. [%]	sys. [%]	total [%]
15	0 to 30	0.0034945	2.31	3.59	4.27
45	30 to 60	0.0064989	1.45	2.92	3.26
80	60 to 100	0.0080697	1.15	1.99	2.3
140	100 to 180	0.0042719	0.97	3.14	3.29
290	180 to 400	0.00015372	4.36	9.9	10.8
bin-center [GeV]	bin [GeV]	$1/\sigma d\sigma / m^{b\bar{b}}$	stat. [%]	sys. [%]	total [%]
30	0 to 60	0.00084771	1.94	3.6	4.09
90	60 to 120	0.004565	0.883	3.13	3.25
180	120 to 240	0.0039658	0.597	0.76	0.967
420	240 to 600	0.00053491	1.27	4.95	5.11

Table 14: Normalised differential cross section as a function of the invariant mass of the lepton-b-jet system.

bin-center [GeV]	bin [GeV]	$1/\sigma d\sigma / dm^{\ell b}$	stat. [%]	sys. [%]	total [%]
40	0 to 80	0.0031487	1.54	6.59	6.76
95	80 to 110	0.0081967	1.56	6.43	6.62
125	110 to 140	0.0078417	1.42	2.89	3.22
270	140 to 400	0.00099155	2.12	13	13.2

777   • Add POWHEG +HERWIG theory prediction to results

778   • Added correlation matrices

13   Updates since AN-13-266-v8

780   • Added PDF uncertainties to result plots

781   • Update result tables with PDF uncertainties

782   • Add differential cross section result as a function of the transverse momentum of the
783   1st and 2nd leading top quark

784   • Added binned control distributions in Appendix

Table 15: Normalised differential cross section as a function of top quark observables: the transverse momentum (p_T^t), the rapidity (y^t), the transverse momentum in the $t\bar{t}$ rest frame ($p_T^t(t\bar{t})^*$), the difference of azimuthal angles of the top-quarks ($\Delta\phi(t,\bar{t})$) and the difference of rapidities of the top-quarks ($|y^t| - |y^{\bar{t}}|$).

bin-center [GeV]	bin [GeV]	$1/\sigma d\sigma/dp_T^t$	stat. [%]	sys. [%]	total [%]
32.5	0 to 65	0.0043301	1.11	2.11	2.39
95	65 to 125	0.0063951	0.898	1.67	1.9
162	125 to 200	0.0030832	1	1.61	1.9
245	200 to 290	0.00086183	1.29	3.51	3.74
345	290 to 400	0.00018768	2.74	7.54	8.02
bin-center	bin	$1/\sigma d\sigma/y^t$	stat. [%]	sys. [%]	total [%]
−2.05	−2.5 to −1.6	0.076282	1.98	6.19	6.5
−1.3	−1.6 to −1	0.19741	1.03	1.62	1.92
−0.75	−1 to −0.5	0.28166	1.08	1.68	2
−0.25	−0.5 to 0	0.33484	1.01	2.09	2.32
0.25	0 to 0.5	0.32837	1.04	1.46	1.79
0.75	0.5 to 1	0.28489	1.12	1.07	1.55
1.3	1 to 1.6	0.20262	1.05	2.27	2.5
2.05	1.6 to 2.5	0.073992	1.97	6	6.32
bin-center [GeV]	bin	$1/\sigma d\sigma/dp_T^t(t\bar{t})^*$	stat. [%]	sys. [%]	total [%]
30	0 to 60	0.004446	1.48	2.66	3.05
87.5	60 to 115	0.006894	1.37	2.09	2.5
152	115 to 190	0.0034069	1.32	1.97	2.37
232	190 to 275	0.00087841	2.15	4.9	5.35
328	275 to 380	0.00018695	2.59	8.91	9.28
440	380 to 500	2.9106e-05	7.49	9.61	12.2
bin-center	bin	$1/\sigma d\sigma/d\Delta\phi(t,\bar{t})$	stat. [%]	sys. [%]	total [%]
0.945	0 to 1.89	0.063992	1.97	5.39	5.74
2.33	1.89 to 2.77	0.29646	1.04	5.2	5.3
2.91	2.77 to 3.04	1.2444	1.05	2.02	2.28
3.1	3.04 to 3.15	2.5825	1.52	7.87	8.02
bin-center	bin	$1/\sigma d\sigma/d|y^t| - |y^{\bar{t}}|$	stat. [%]	sys. [%]	total [%]
−1.8	−2.5 to −1.1	0.064512	2.56	3.82	4.59
−0.8	−1.1 to −0.5	0.29468	1.45	2.09	2.54
−0.25	−0.5 to 0	0.46278	1.5	2.24	2.7
0.25	0 to 0.5	0.4565	1.52	3.05	3.4
0.8	0.5 to 1.1	0.29431	1.45	2.38	2.79
1.8	1.1 to 2.5	0.068243	2.43	4.48	5.09

Table 16: Normalised differential cross section as a function of transverse momentum of the leading and second leading top quark: $p_T^{Lead.t}$, $p_T^{NLead.t}$.

bin-center [GeV]	bin [GeV]	$1/\sigma d\sigma/dp_T^{Lead.t}$	stat. [%]	sys. [%]	total [%]
37.5	0 to 75	0.0033057	1.51	3.33	3.66
102	75 to 130	0.0064253	1.11	1.96	2.26
165	130 to 200	0.0036651	1.2	2.32	2.61
245	200 to 290	0.0011741	1.49	3.78	4.06
345	290 to 400	0.00026088	3.19	5.87	6.68
bin-center [GeV]	bin [GeV]	$1/\sigma d\sigma/dp_T^{NLead.t}$	stat. [%]	sys. [%]	total [%]
27.5	0 to 55	0.0053812	1.71	2.22	2.8
87.5	55 to 120	0.0067351	1.38	1.73	2.21
160	120 to 200	0.0025027	1.71	1.83	2.5
245	200 to 290	0.00055808	2.42	4.45	5.06
345	290 to 400	0.00011447	5.13	13.3	14.2

Table 17: Normalised differential cross section as a function of top quark pair observables: the transverse momentum ($p_T^{t\bar{t}}$), the rapidity ($y^{t\bar{t}}$) and the invariant mass ($^{t\bar{t}}$).

bin-center [GeV]	bin [GeV]	$1/\sigma d\sigma/dp_T^{t\bar{t}}$	stat. [%]	sys. [%]	total [%]
15	0 to 30	0.01426	0.838	5.89	5.95
55	30 to 80	0.0069019	0.975	4.48	4.59
125	80 to 170	0.0019136	1.09	5.08	5.2
235	170 to 300	0.00034654	2.13	5.32	5.73
bin-center	bin	$1/\sigma d\sigma/dy^{t\bar{t}}$	stat. [%]	sys. [%]	total [%]
-2	-2.5 to -1.5	0.047092	4.05	7.37	8.4
-1.25	-1.5 to -1	0.18185	1.75	2.31	2.9
-0.75	-1 to -0.5	0.3091	1.44	1.36	1.98
-0.25	-0.5 to 0	0.41833	1.22	2.19	2.5
0.25	0 to 0.5	0.40866	1.25	1.72	2.12
0.75	0.5 to 1	0.31462	1.49	1.32	1.99
1.25	1 to 1.5	0.17938	1.84	1.82	2.59
2	1.5 to 2.5	0.045888	3.98	8.09	9.02
bin-center [GeV]	bin [GeV]	$1/\sigma d\sigma/dm^{t\bar{t}}$	stat. [%]	sys. [%]	total [%]
360	340 to 380	0.0041432	2.99	7.76	8.31
425	380 to 470	0.0044957	1.74	3.48	3.89
545	470 to 620	0.001953	1.81	2.89	3.42
720	620 to 820	0.00052517	2.81	3.71	4.66
960	820 to 1100	0.00010027	3.69	8.9	9.64
1350	1100 to 1600	7.278e-06	14.4	28.4	31.8

A   Binned Control Distributions

In Section 9 a Data-to-MC slope is shown in p_T related quantities, both for detector objects, such as leptons and b-jets, as for reconstructed objects as the top quark and top-quark pair. The effect of different event reconstruction and selection, and check for unfolding biases are studied in Appendix C and B respectively. No individual source of this effect is found.

The effect of different top-quark-pair regimes (invariant mass, transverse momentum) on the top-quark transverse momentum spectrum are studied. The top-quark p_T spectra is measured in the kinematic ranges

- top-quark-pair invariant mass: $m^{t\bar{t}} = [340, 380], [380, 470], [470, 620], [620, 820], [820, 1100],$ $[1100, 1600]$ GeV
- top-quark-pair transverse momentum: $p_T^{t\bar{t}} = [0, 30], [30, 80], [80, 170], [170, 300]$ GeV

Control distributions in the aforementioned kinematic ranges are shown in Figures 48 and 49. The $t\bar{t}$ contribution is normalised to the cross section value obtained in the standard analysis and shown in Table 9.

Figures 48 and 49 show that the reconstruction level Data-to-MC slope in the top-quark transverse momentum is present in all different $t\bar{t}$ regions.

B   Check in the Unfolding Method

B.1   Closure Test

To demonstrate sensitivity of the unfolding procedure to possible deviations of the data from the expectation as implemented in the simulation, several closure tests have been performed. To replace our data, an equivalent of 19.7 fb^{-1} of simulation from the $t\bar{t}$ MADGRAPH +MADSPIN [6, 15] simulation signal sample which we call "pseudo-data", is used. The pseudo-data is then varied by assigning weights to the events based on the true level values. After reweighting, the true level information is ignored and the pseudo-data is treated in the same way as the real data of the standard analysis.

The weighted fake data are then unfolded using the non-reweighted MADGRAPH +MADSPIN [6] sample. This way, possible biases of the method due to the use of a possibly inappropriate simulation are estimated.

In the following, the result of this study in the $\mu^\pm e^\mp$ channel is presented. Similar results are found in e$^+$e$^-$ and $\mu^+\mu^-$ channels.

For the investigation of the top rapidity distribution, the event weights are determined using the following linear function:

$$w = \max\Big(\left(1 + (|y_t| - 1)s\right) \left(1 + (|y_{\bar{t}}| - 1)s\right), 0.1\Big) \tag{27}$$

where w is the weight of an event, top quark y the rapidity (at generator truth level), and s a slope that is varied.

For the top p_T distribution the event weights are determined using the following linear function:

$$w = \max\left(\left(1 + \left(\frac{p_{T,t}}{\text{GeV}} - 100\right)s\right) \left(1 + \left(\frac{p_{T,\bar{t}}}{\text{GeV}} - 100\right)s\right), 0.1\right) \tag{28}$$

where w is the weight of an event, p_T the transverse momentum (at generator truth level), and s a slope that is varied.
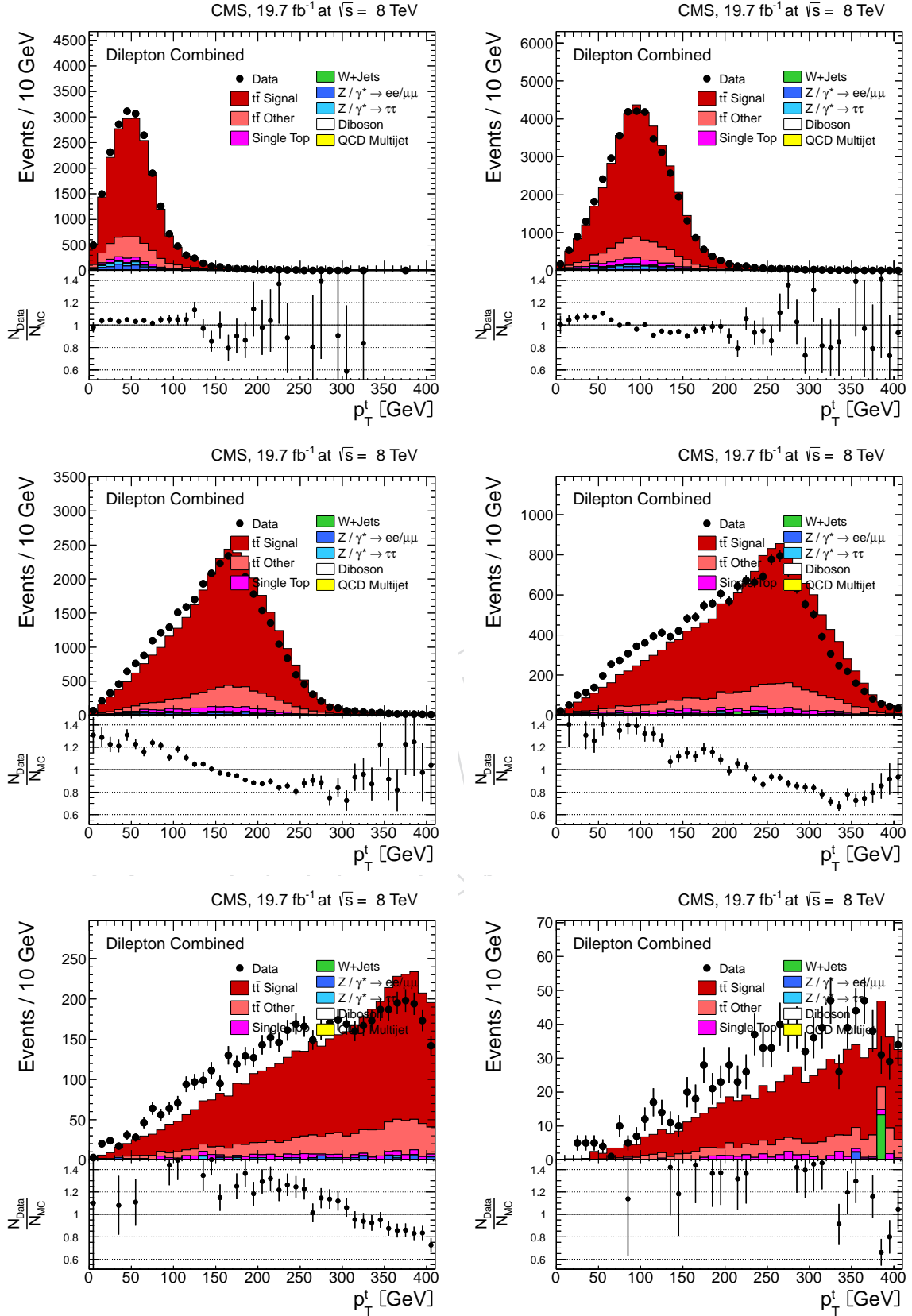
Figure 48: Control distributions of the top-quark tranverse momentum in different top-quark-pair invariant mass ranges. From top to bottom, from left to right: $m^{t\bar{t}} = [340, 380]$, $[380, 470]$, $[470, 620]$, $[620, 820]$, $[820, 1100]$, $[1100, 1600]$ GeV
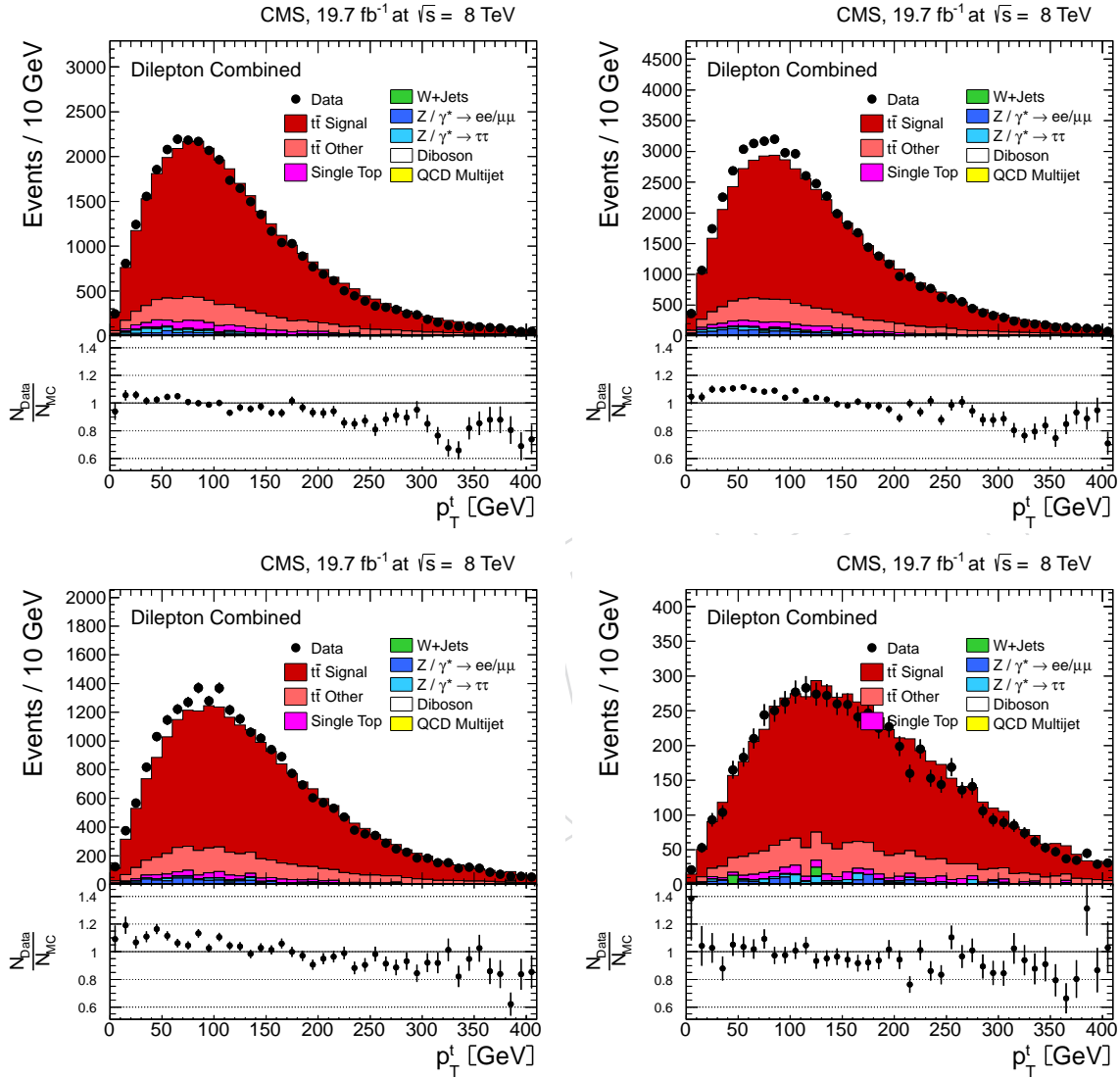
Figure 49: Control distributions of the top-quark tranverse momentum in different top-quark-pair transverse momentum ranges. From top to bottom, from left to right: $p_T^{t\bar{t}} = [0,30], [30,80], [80,170], [170,300]$ GeV

The results for different values for positive and negative slopes can be found in Figures 50 to 53. For both observables, the reconstructed "pseudo-data" distributions follow the modified generated input distribution ("Simu. Reweighted"). However, the control plots on the left of Figures 50 – 53, show that larger deviations from the simulation would be visible also in the control distributions before unfolding. As the control plots agree with real data, the measurement is performed in a region where the unfolding only introduces negligible bias.

B.2   Pull Plots

An independent study is performed to check any biases in the error of the result due to the unfolding method. 1000 pseudo-experiments are performed by randomly varying the elements of the covariance matrix according to a Gaussian distribution (centered at 0 and width 1). The following figures show the pull distributions for the pseudo-experiments, defined as $\frac{x_{exp} - x_{mean}}{\sigma_{exp}}$. The results correspond to differential cross-section as a function of the top quark momentum and in the three channels $\mu^+\mu^-$, $\mu^\pm e^\mp$ and e^+e^- are shown in Figures 54, 55 and 56 respectively. The pull distributions are centered at 0 with a width close to 1, similar results are obtained for the rest of the variables. This result confirms that the unfolding method introduces a negligible bias in the result.

C   Checks for Biases Due to Event Selection

The default analysis, described in Section 3 is modified changing different event selection criteria to find possible experimental sources of trend in the top-quark p_T spectrum. The different variations which are studied are:

- Different PU regimes: PU$\leq$ 10, 10 $\leq$PU$\leq$ 16 and PU$\geq$ 16
- Tight muon ID requirement
- 2 CSVL b tagged jets
- 1 CSVT jet tagged as b jet

Results for lepton p_T top quark p_T $t\bar{t}$ system p_T and $t\bar{t}$ invariant mass are derived for each variation listed above, for the combination of e^+e^- $\mu^\pm e^\mp$ and $\mu^+\mu^-$ channels. Results are shown in Figures 57 to 62.

C.1   Different PU Regimes

The analysis is repeated by requiring a certain number of reconstructed primary vertices in the event. Three different PU regimes are requested: PU$\leq$ 10, 10 $\leq$PU$\leq$ 16 and PU$\geq$ 16.

Results for the 3 different PU ranges are shown in Figures 57, 58 and 59. The additional requirement of an specific PU range leads to a reduction of the final number of events by 50-75%, depending on the particular PU region. The statistical uncertainty on the final result only increases by 0.7-1.5%, depending on the particular bin and the PU range selected. No significant effect in the fully unfolded result is visible, and thus the Data-to-Simulation p_T trend remains.
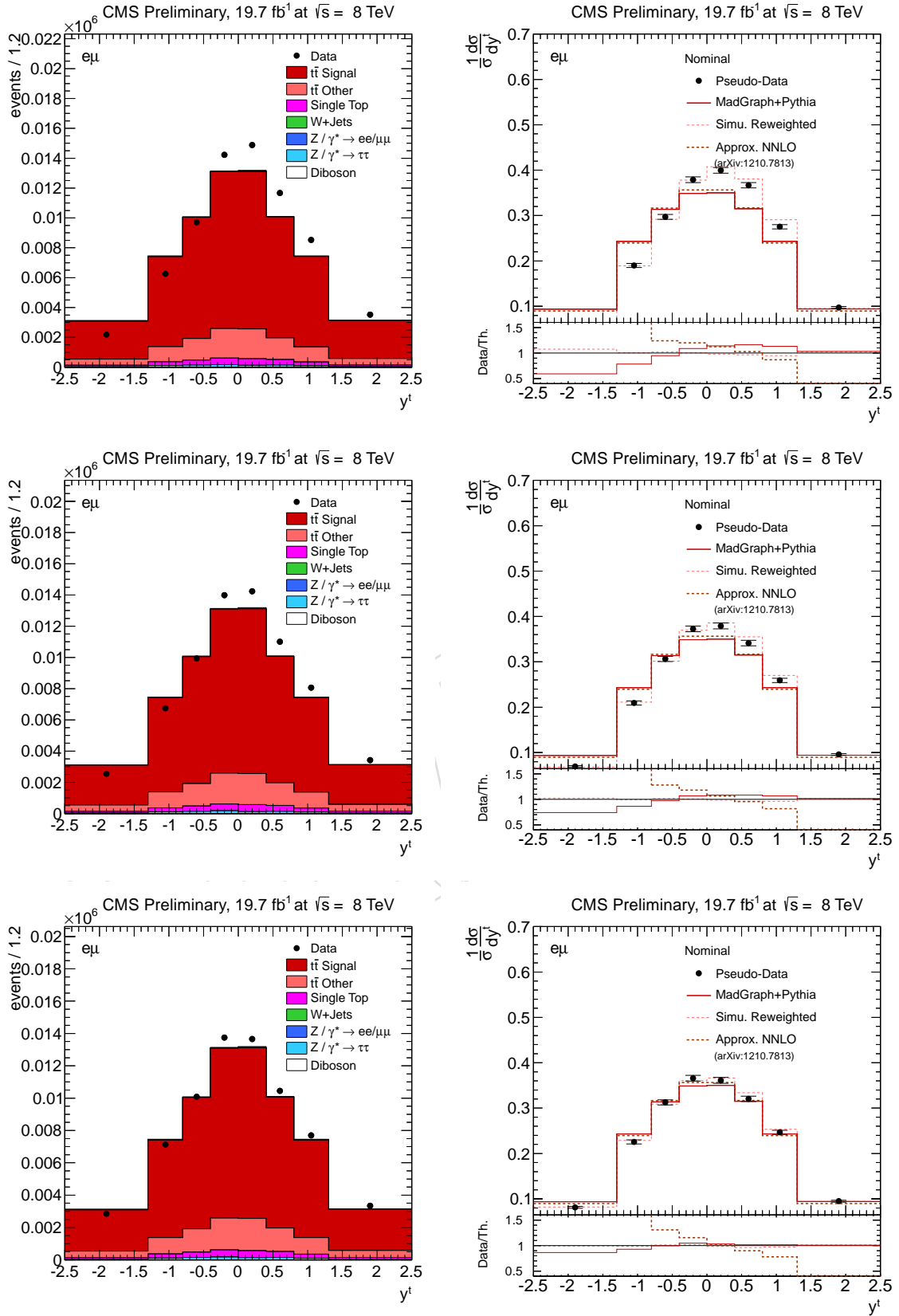
Figure 50: Control distributions (left column) and normalised differential cross sections (right column) as a function of the top quark rapidity for the shape variations of the signal, variations with slope -0.240, -0.160, -0.080.
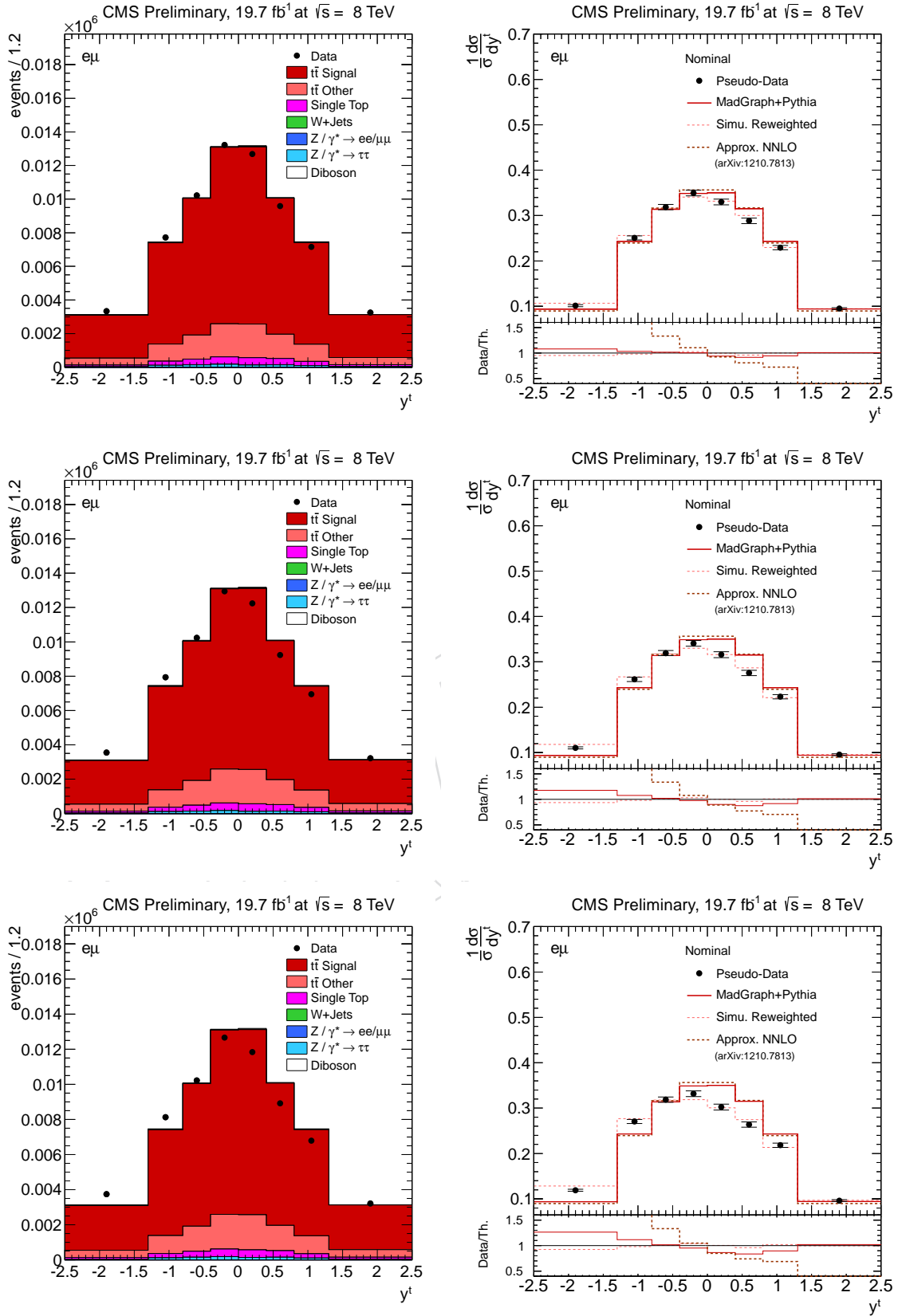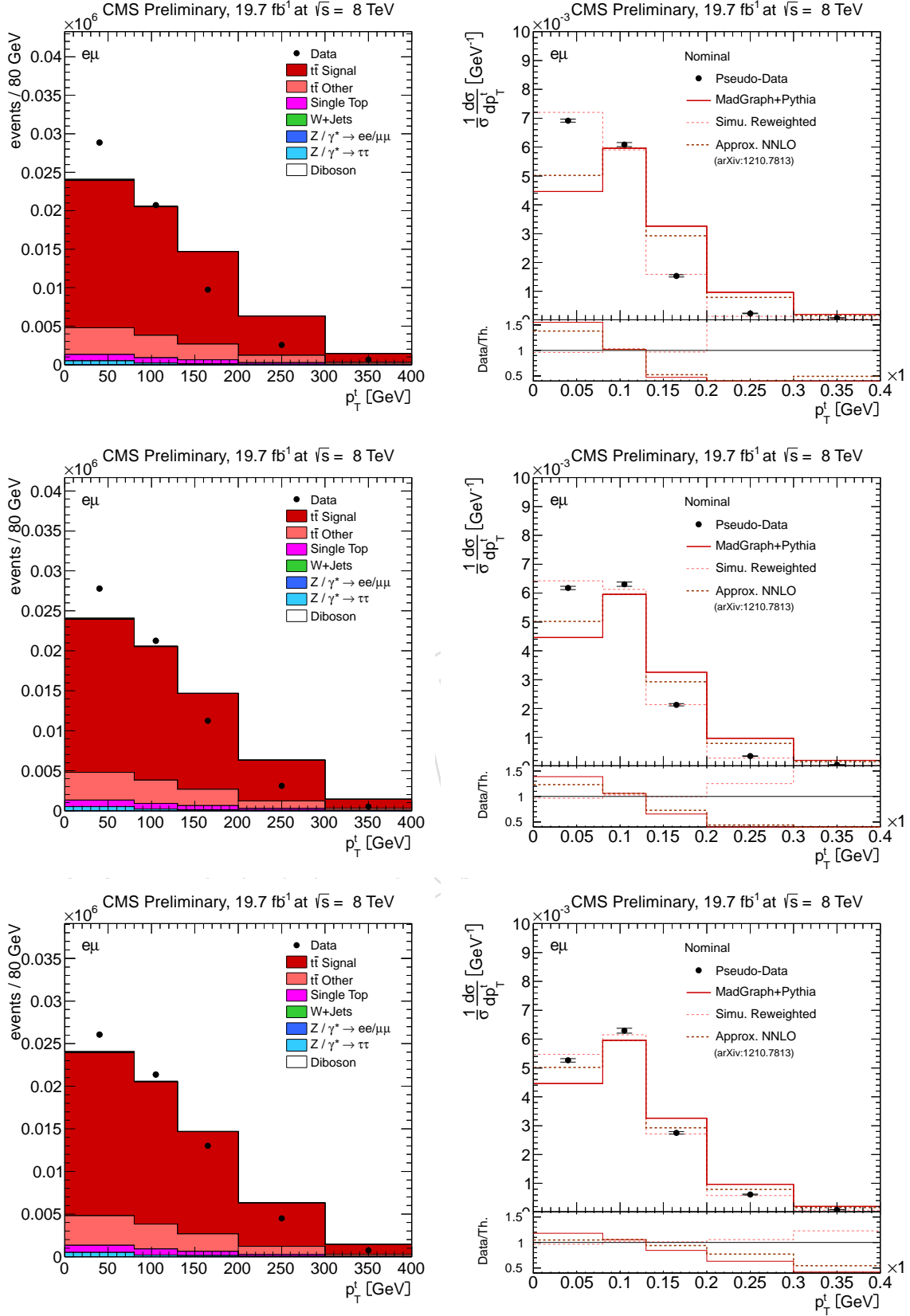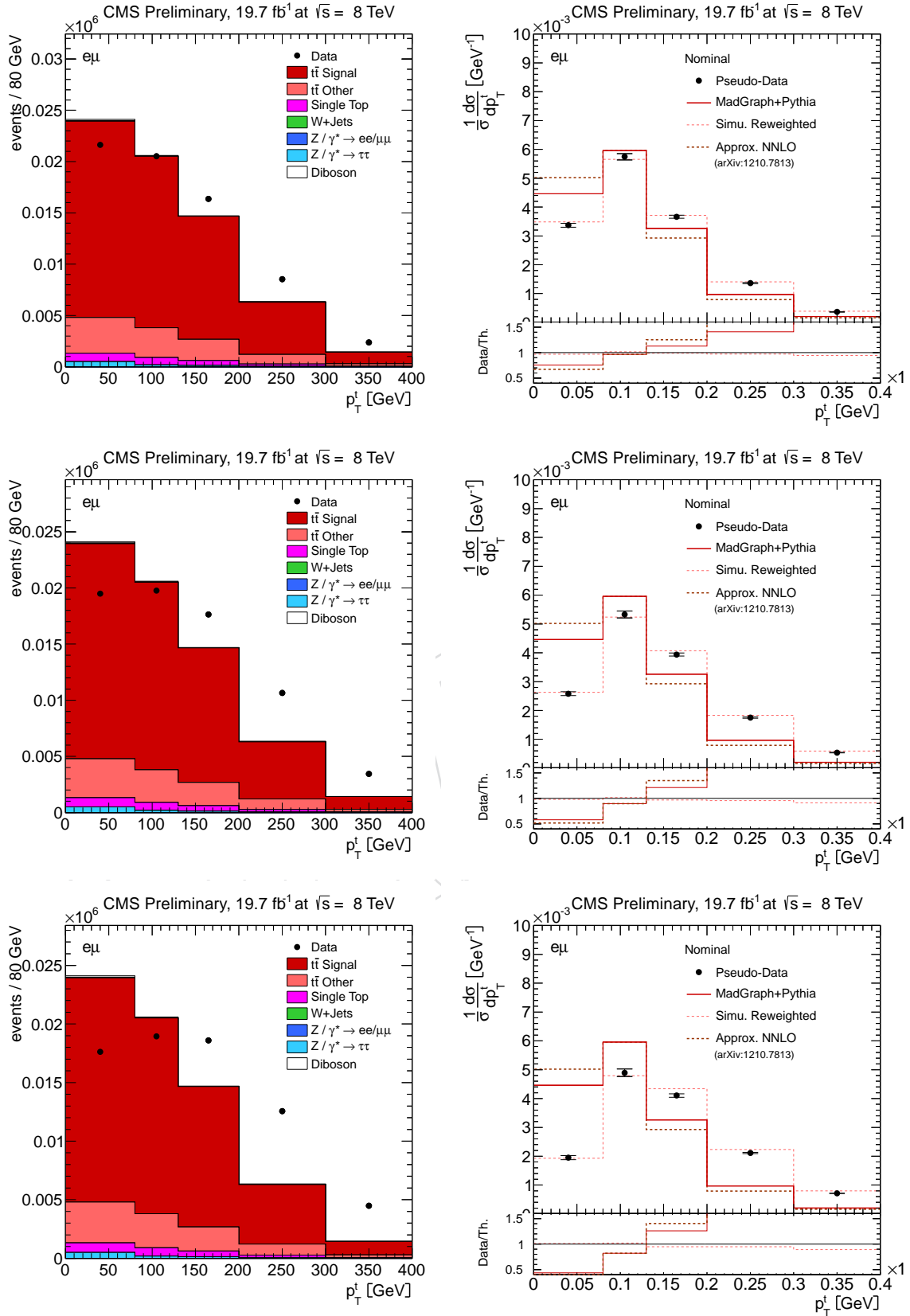
Figure 51: Control distributions (left column) and normalised differential cross sections (right column) as a function of the top quark rapidity for the shape variations of the signal, variations with slope 0.080, 0.160, 0.240.

Figure 52: Control distributions (left column) and normalised differential cross sections (right column) as a function of the top quark p_T for the shape variations of the signal, variations with slope -0.006 (top row), -0.004 (middle row), -0.002 (bottom row).

Figure 53: Control distributions (left column) and normalised differential cross sections (right column) as a function of the top quark p_T for the shape variations of the signal, variations with slope 0.002 (rop tow), 0.004 (middle row), 0.006(bottom row).
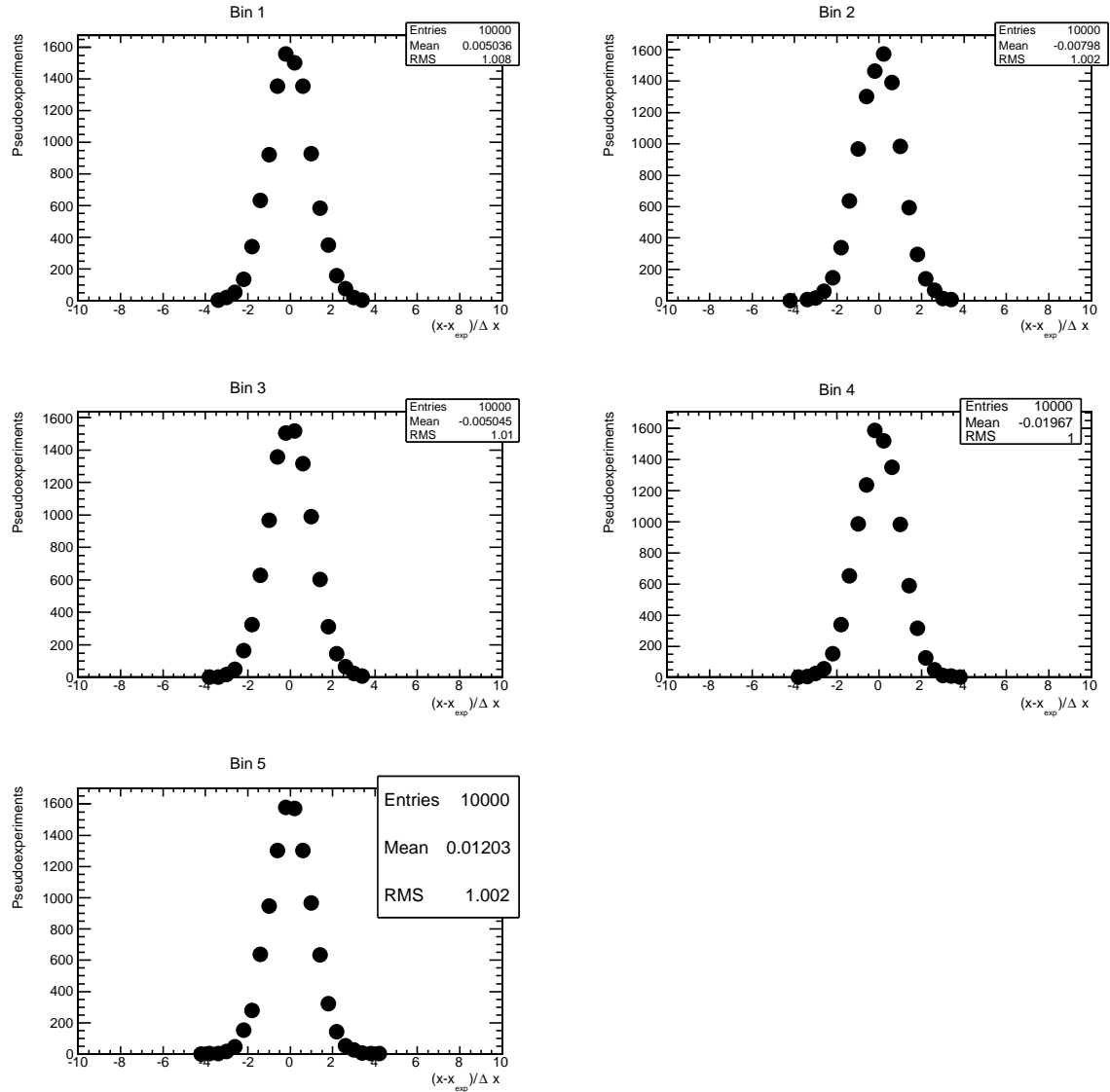
Figure 54: Pull distributions for each of the bins of the normalised differential cross-section as a function of p_T measured in the $\mu^+\mu^-$ channel. From top to bottom and left to right, the plots correspond to the bins (0,80), (80,130), (130,200), (200,300), (300,400) GeV.
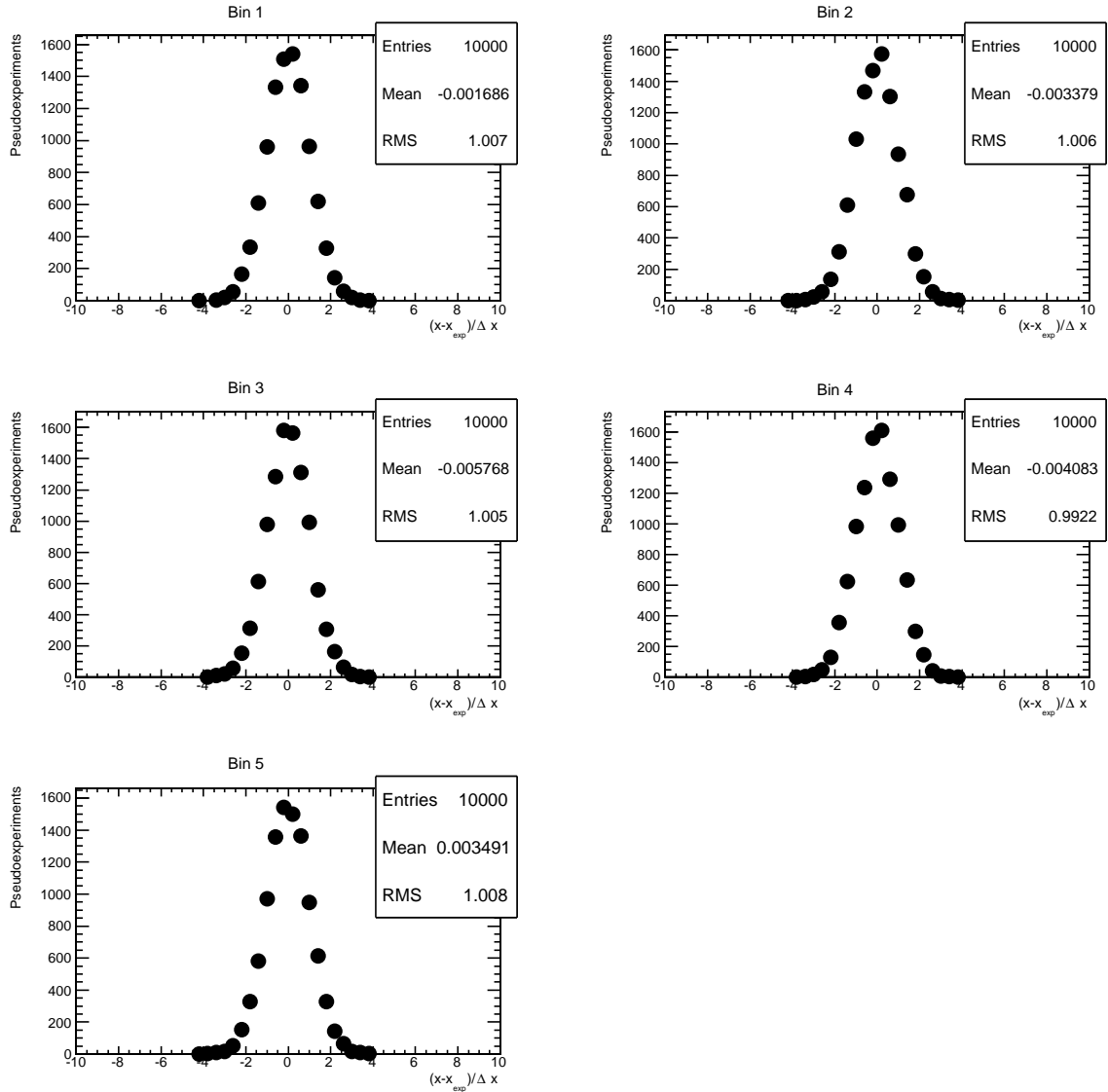
Figure 55: Pull distributions for each of the bins of the normalised differential cross-section as a function of p_T measured in the $\mu^\pm e^\mp$ channel. From top to bottom and left to right, the plots correspond to the bins (0,80), (80,130), (130,200), (200,300), (300,400) GeV.
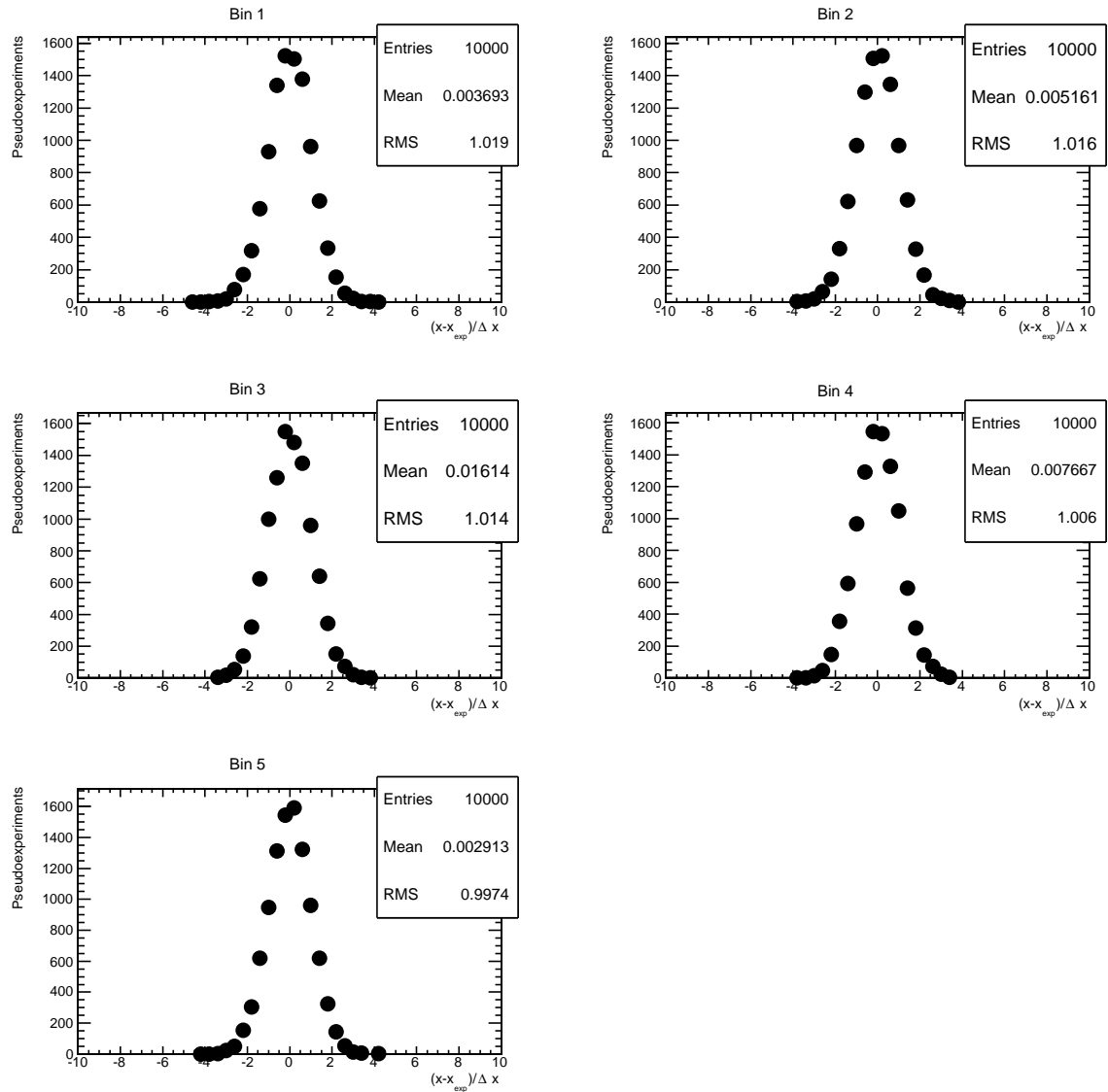
Figure 56: Pull distributions for each of the bins of the normalised differential cross-section as a function of p_T measured in the e^+e^- channel. From top to bottom and left to right, the plots correspond to the bins (0,80), (80,130), (130,200), (200,300), (300,400) GeV.
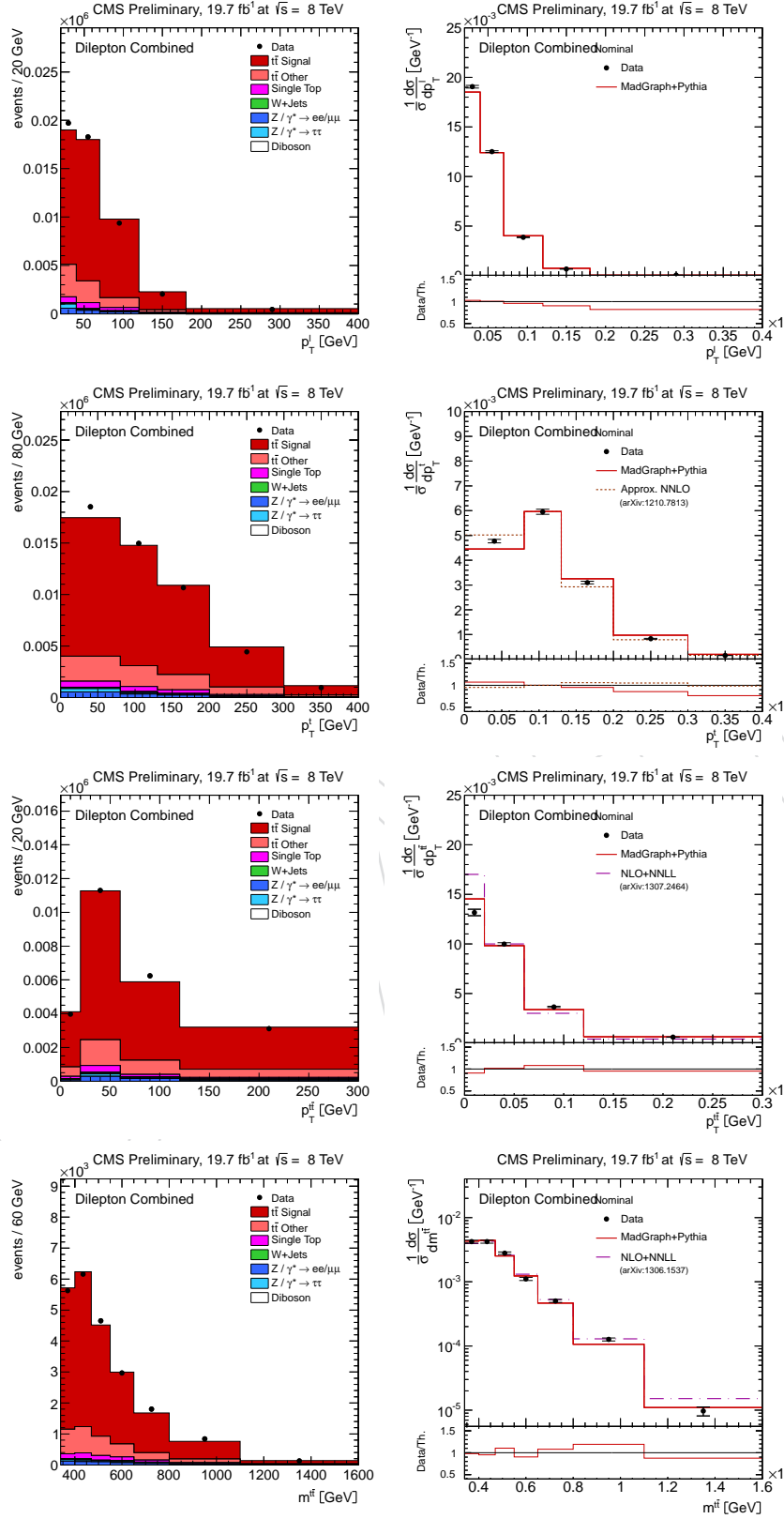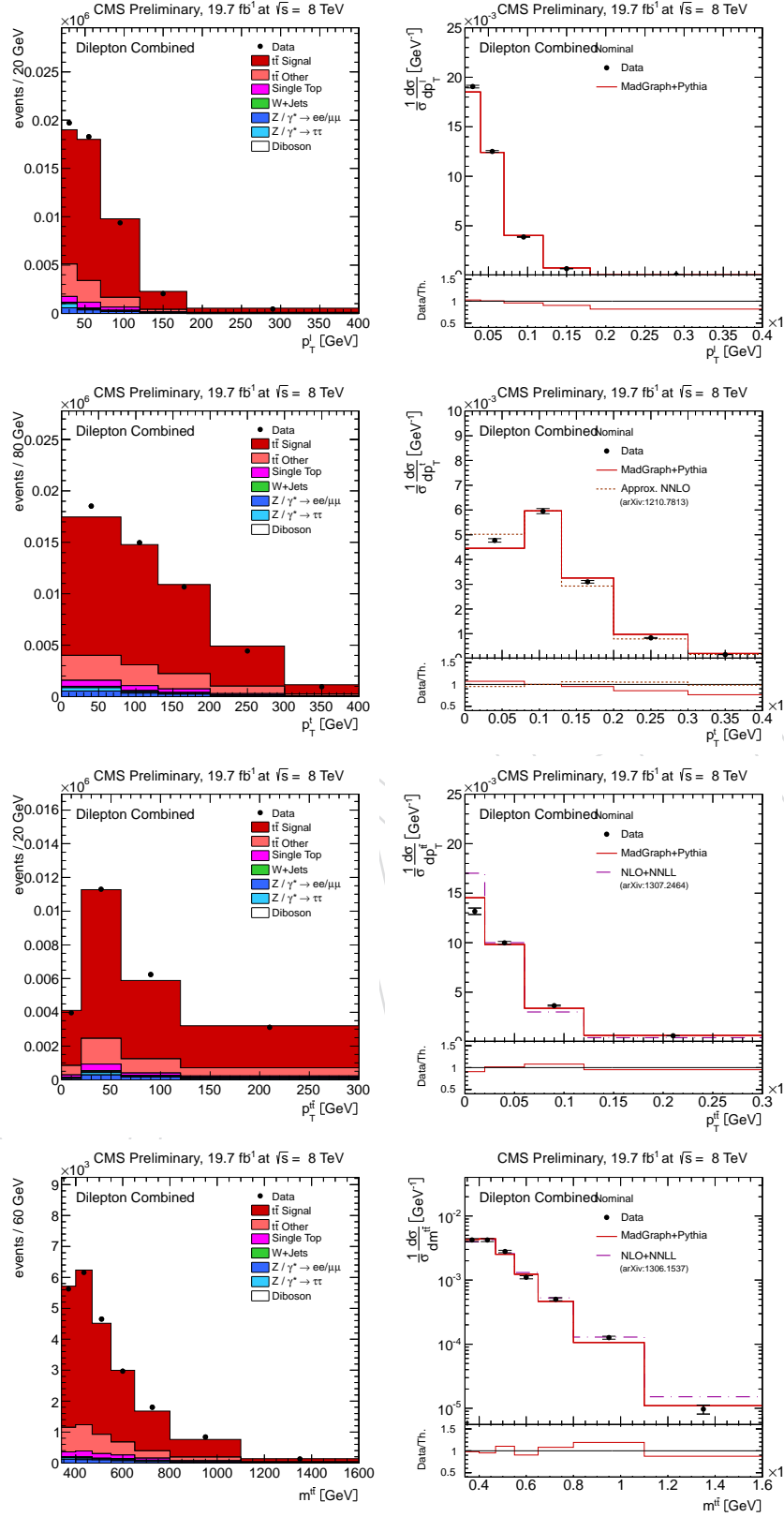
Figure 57: Event yield (left column) and normalised differential cross section (right column) as a function of lepton (top row), top quark p_T (middle top row), top quark pair p_T (middle low row) and top quark pair invariant mass (bottom row). The statistical uncertainties only are considered in the normalised differential cross section result. Results are derived in events with a number of vertices: $PU \leq 10$
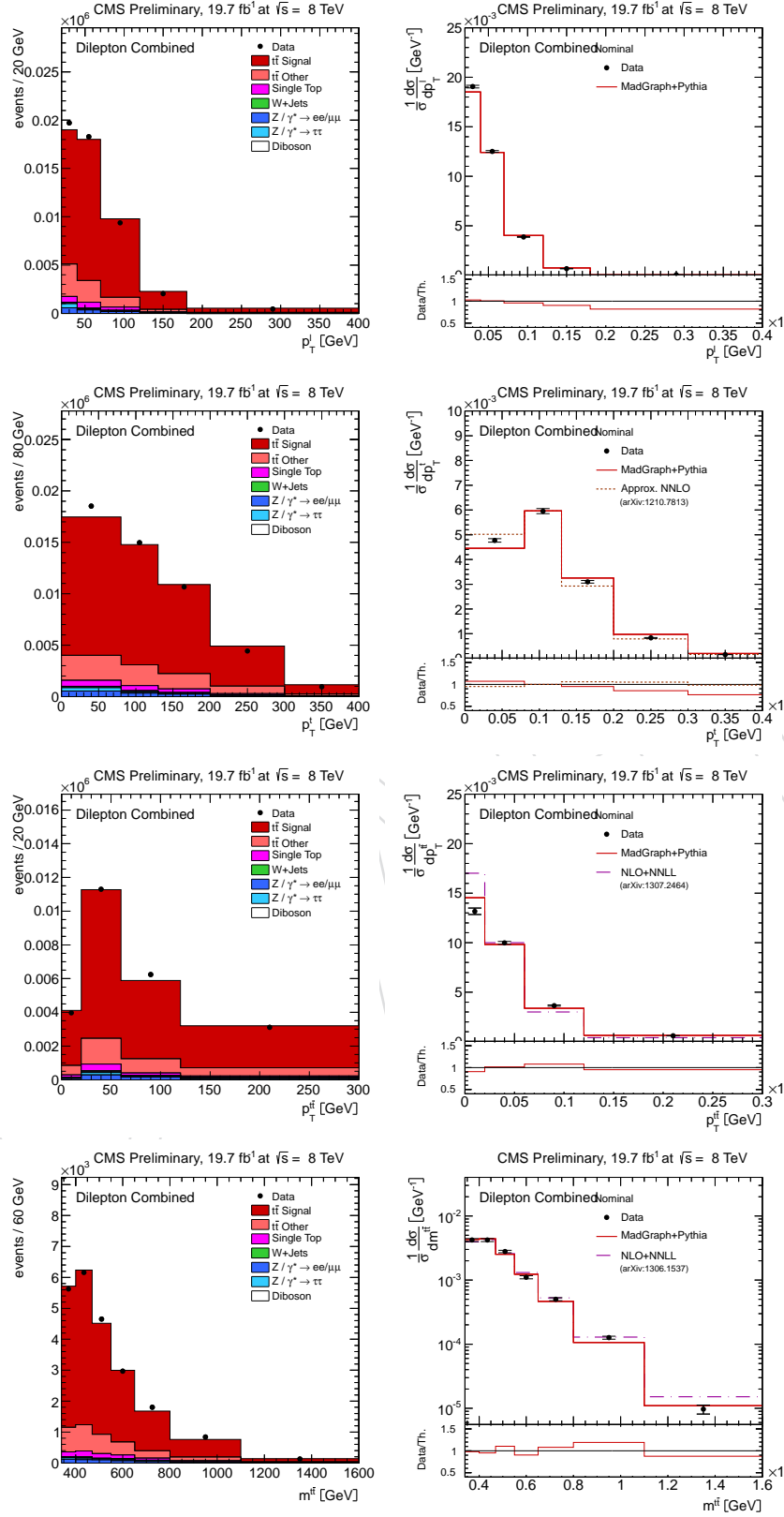
Figure 58: Event yield (left column) and normalised differential cross section (right column) as a function of lepton (top row), top quark p_T (middle top row), top quark pair p_T (middle low row) and top quark pair invariant mass (bottom row). The statistical uncertainties only are considered in the normalised differential cross section result. Results are derived in events with a number of vertices: $10 \leq PU \leq 16$

Figure 59: Event yield (left column) and normalised differential cross section (right column) as a function of lepton (top row), top quark p_T (middle top row), top quark pair p_T (middle low row) and top quark pair invariant mass (bottom row). The statistical uncertainties only are considered in the normalised differential cross section result. Results are derived in events with a number of vertices: $PU \geq 16$

C.2   Tight Muon Identification

In the main analysis the loose muon reconstruction and identification criteria where used to select $t\bar{t}$ dileptonic events involving muons. The effect of a tighter selection is studied by re- quiring the muons to be reconstructed and identified with the CMS *Tight Muon Id*.

Tight muons are reconstructed with the Particle Flow algorithm. A global fit is done using tracks from the tracker and the muon detector, requiring a χ^2/ndf of the global fit to be below 10. The muon tracks in the tracking detector are required to have at least 1 valid hit in the pixel detector and 5 hits in the tracker layers, and in addition at least 1 valid hit in the muon chamber. Furthermore, at least one of the muon chambers has to be matched to the track reconstructed in the tracker system. The longitudinal distance of the muon track with respect to the primary vertex has to be below 0.5 cm, and the relative isolation as defined in 3.1 should be less than 0.09.

In this analysis set up, the identified tight muons are required to have kinematic constrains identical as in the default analysis:$p_\mathrm{T} > 20$ GeV and $|\eta| \leq 2.4$

This event selection, reduces the background in the final event selection but not significant effect appears in the final unfolded cross section result. Results are shown in Figures 60
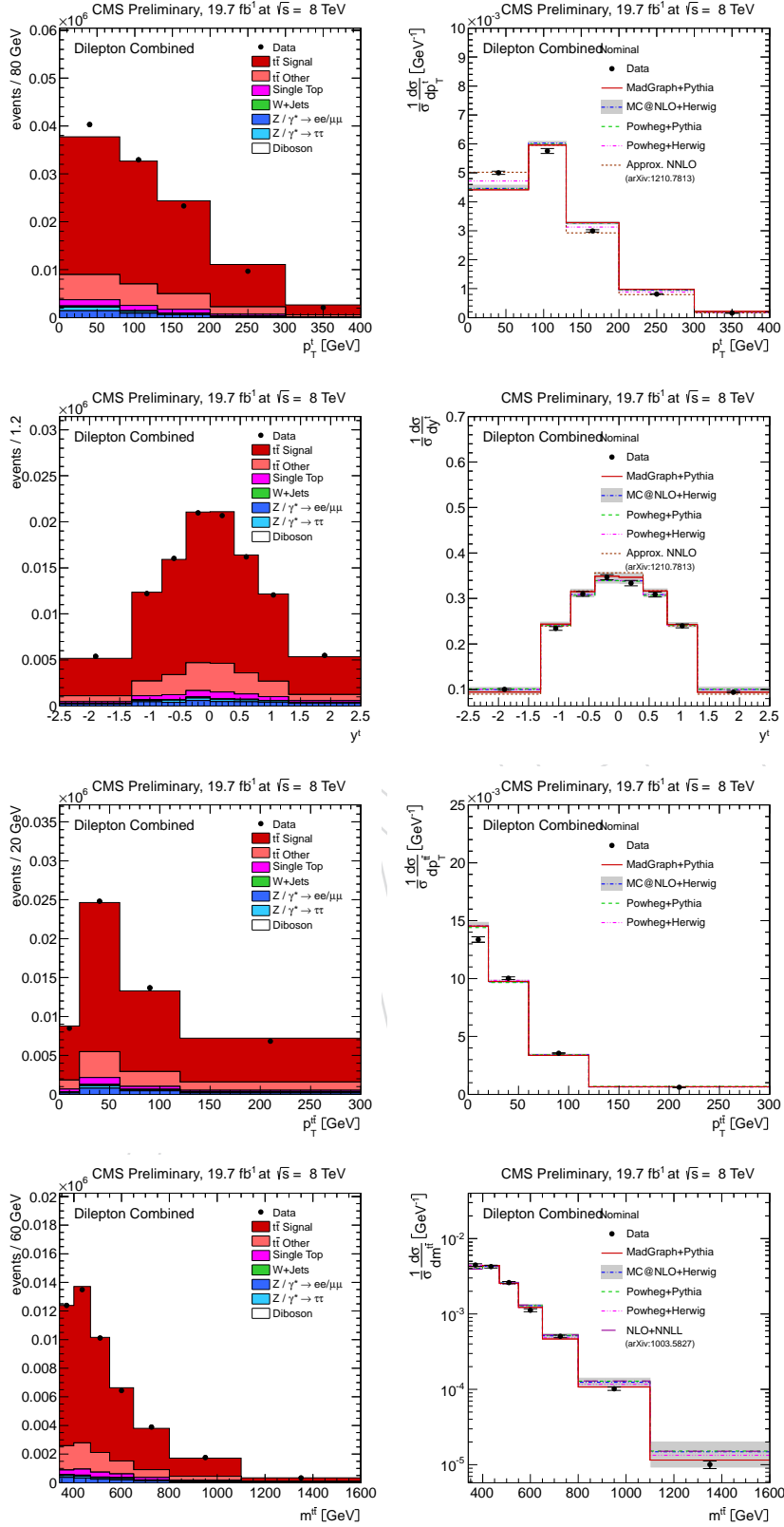
Figure 60: Event yield (left column) and normalised differential cross section (right column) as a function of lepton (top row), top quark p_T (middle top row), top quark pair p_T (middle low row) and top quark pair invariant mass (bottom row). The statistical uncertainties only are considered in the normalised differential cross section result. Results are derived in events with tight muon ID criteria

C.3   Different b-tagging Requirements

The standard analysis requires 2 jets, and at least one of those to be tagged a b-jet with a CSV algorithm in the loose working point. The event selection is modified by requiring more or different b tagged jets.

In a first step 2 CSVL b tagged jets are requested. The result is shown in Figure 61. This increases the purity of the final event composition, increasing the $t\bar{t}$ compositions from $\sim 79\%$ to $\sim 82\%$. The difference in the top quark p_T result changes by less than 1% in statistically relevant bins, and the statistical uncertainty of the result is reduced by $\sim 0.2\%$.

A different b tagging requirement is also tested. The "tight" (T) working point of the same combined secondary vertex tagging algorithm is used in this case. In this case the tight working point corresponds to a light jet mistag efficiency of $\sim 0.1\%$. In this approach the event is required to have 1 CSVT jet. Results are shown in Figure 62. The particular choice of the event cut reduces the background contribution in the composition of the final event from $\sim 21\%$ to $\sim 17\%$. This, nevertheless, has an small effect in the final result. In the particular case of the top quark p_T differential cross section the central values change by less than 0.5% in statistically relevant bins, while the statistical uncertainty changes by less than 0.1%.
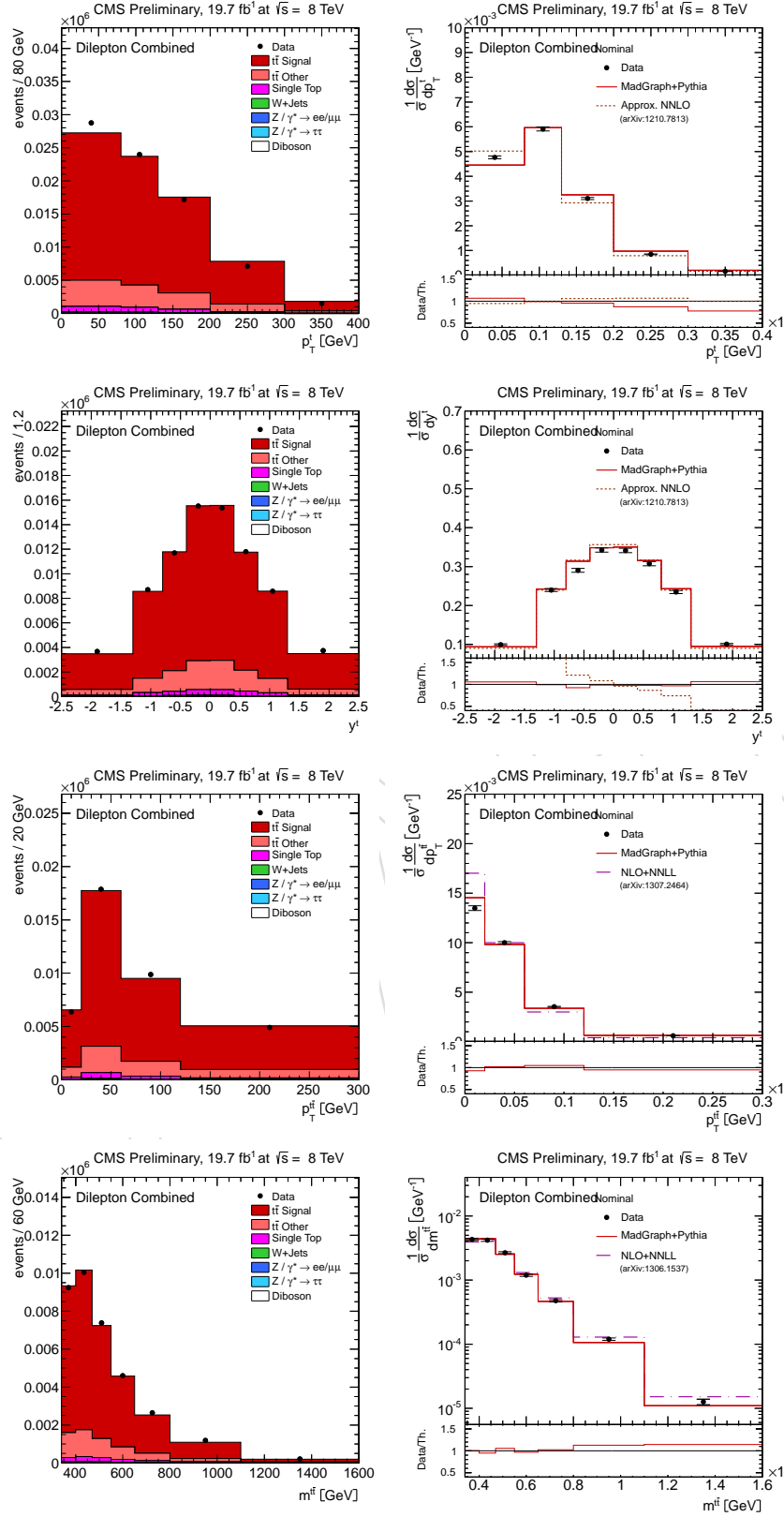
Figure 61: Event yield (left column) and normalised differential cross section (right column) as a function of lepton (top row), top quark p_T (middle top row), top quark pair p_T (middle low row) and top quark pair invariant mass (bottom row). The statistical uncertainties only are considered in the normalised differential cross section result. Results are derived in events with 2 CSVL b jets
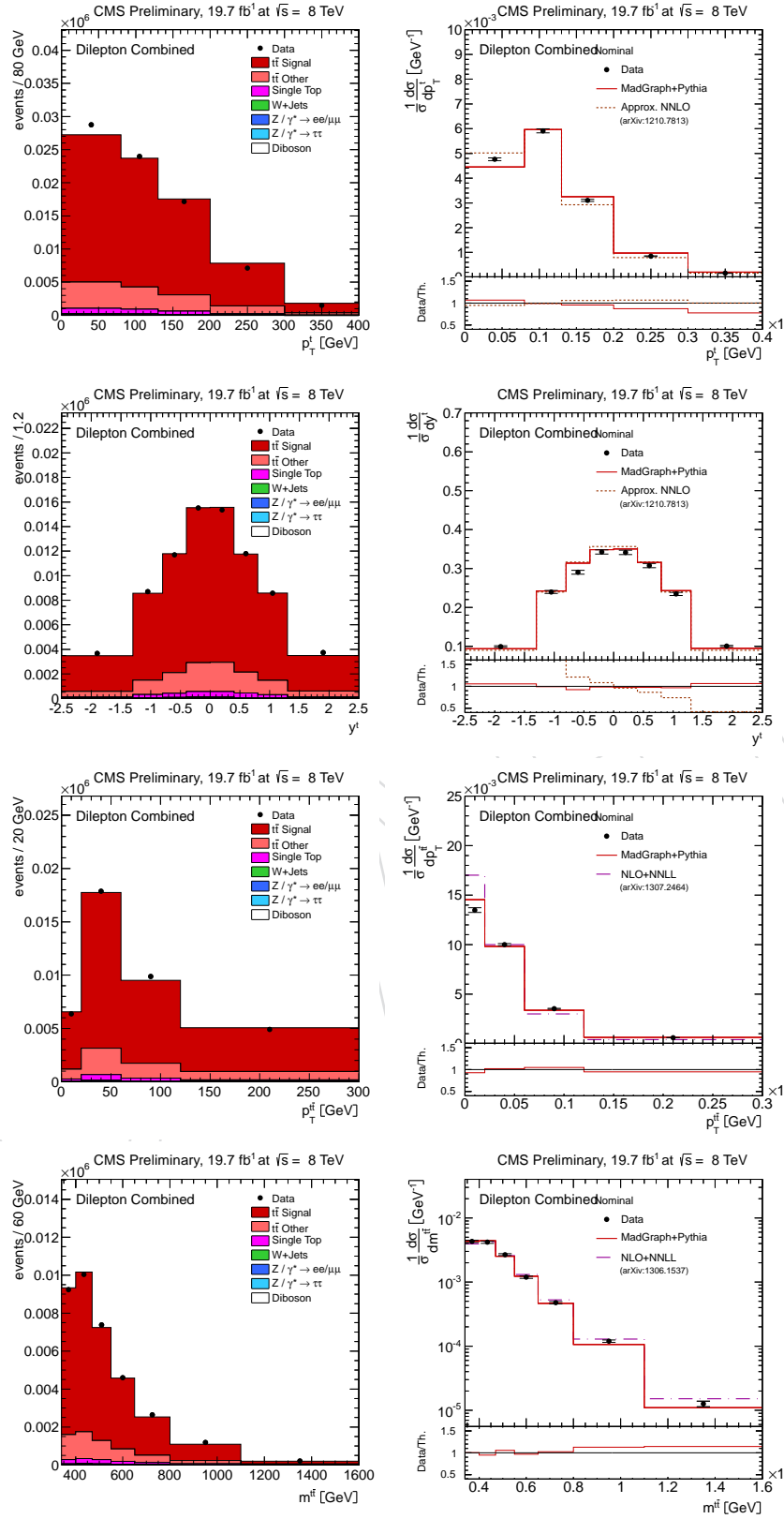
Figure 62: Event yield (left column) and normalised differential cross section (right column) as a function of lepton (top row), top quark p_T (middle top row), top quark pair p_T (middle low row) and top quark pair invariant mass (bottom row). The statistical uncertainties only are considered in the normalised differential cross section result. Results are derived in events with 1 CSVT b jet

D Covariance Matrices of Uncertainties

The correlation of the systematic uncertainties among different bins are measured by means of the covariance matrices.

The statistical covariance matrix $cov^{stat.}$ is defined in Sec. 8.3.

The covariance matrix ($cov^{syst.}$) of a given systematic source between two bins i and j is defined as the product of the uncertainty (δ) of the result in each of the bins

$$cov_{ij}^{syst.} = \delta_i \cdot \delta_j \tag{29}$$

The full correlation matrix of all systematic uncertainty sources is given as the sum of the covariance matrices of the individual covariance matrices

$$cov_{ij}^{total\ syst.} = \sum_{all\ syst.} cov_{ij}^{syst.} \tag{30}$$

while the total covariance matrix is then derived as

$$cov_{ij}^{total} = cov_{ij}^{stat.} + cov_{ij}^{syst.} \tag{31}$$

Finally, the correlation of the measured normalised differential cross section is derived as

$$cov_{ij}^{total} = \frac{cov_{ij}^{total}}{\sqrt{cov_{ii}^{total} \cdot cov_{jj}^{total}}} \tag{32}$$

Result of the full correlation matrices for all measured variables are presented in Fig. 63 to 67, for the $\mu^{\pm}e^{\mp}$ channel.
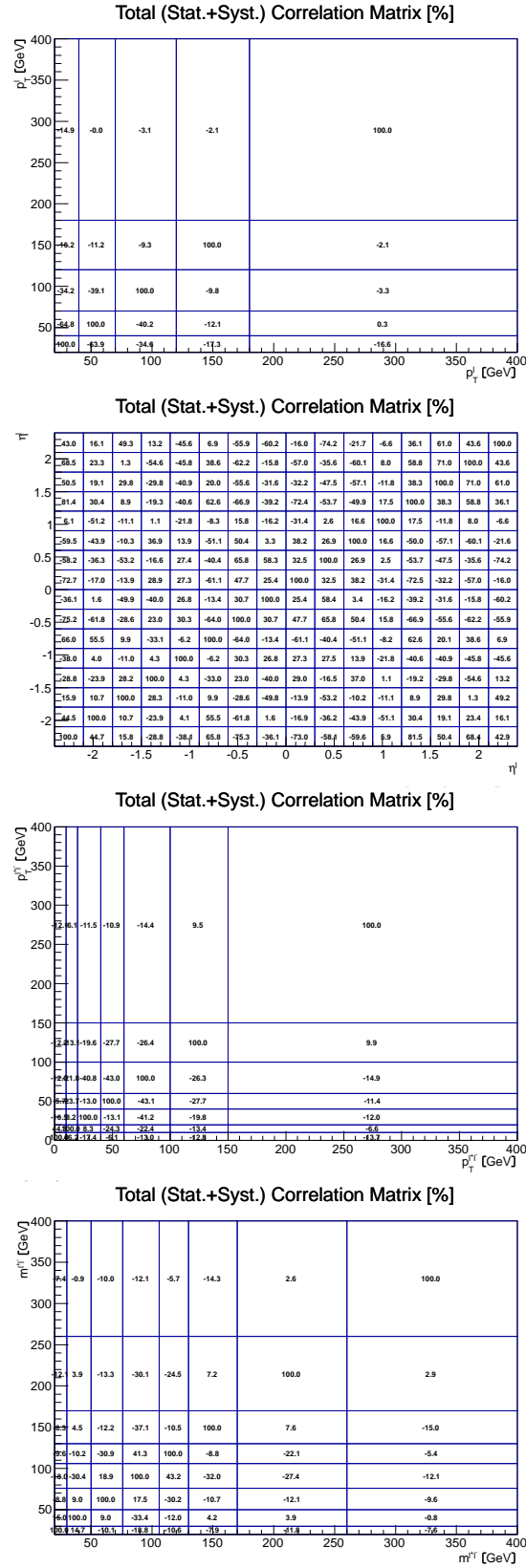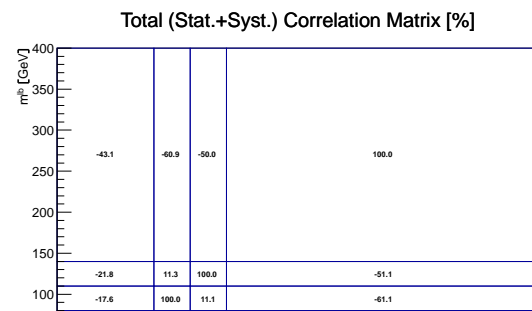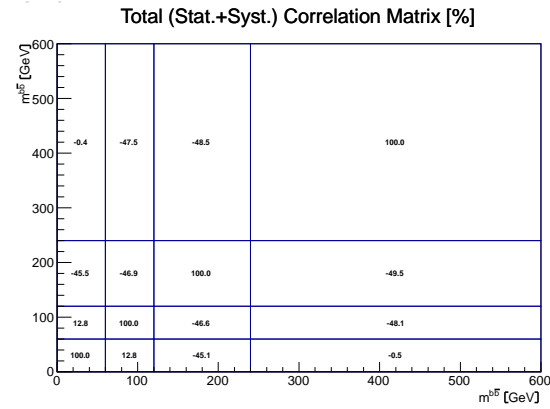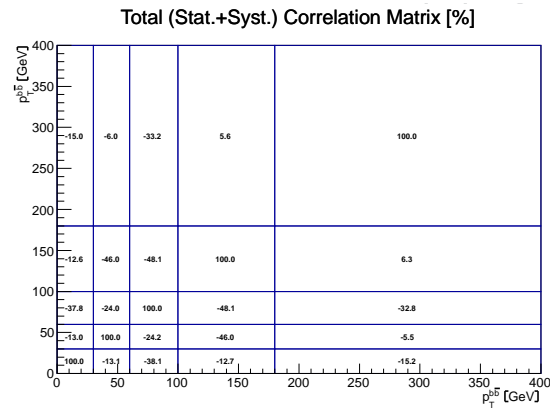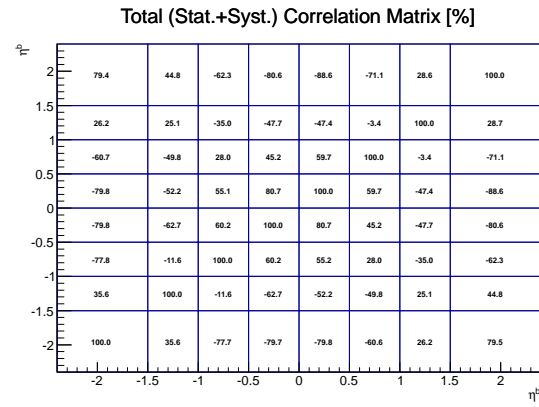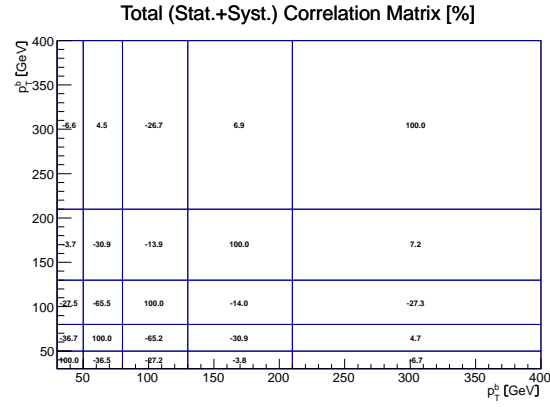
Figure 63: Covariance matrix of all systematic uncertainties for the lepton p_{T} (top left), lepton η (top right), lepton-pair p_{T} (bottom left) and lepton-pair invariant mass (bottom right). Results are only considered for the combination of the e^+e^-, $\mu^\pm e^\mp$ and $\mu^+\mu^-$ channels.

Total (Stat.+Syst.) Correlation Matrix [%]

Total (Stat.+Syst.) Correlation Matrix [%]

Total (Stat.+Syst.) Correlation Matrix [%]

Total (Stat.+Syst.) Correlation Matrix [%]
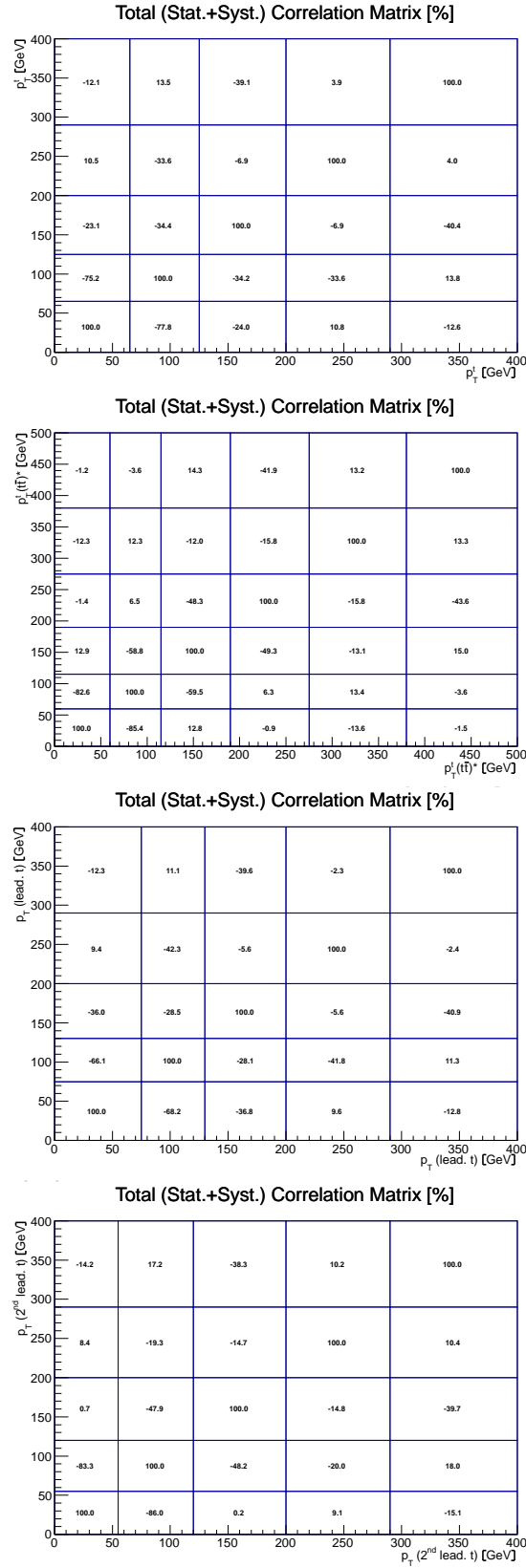

Total (Stat.+Syst.) Correlation Matrix [%]

Figure 65: Covariance matrix of all systematic uncertainties for the top-quark p_T (top left), top-quark p_T in the $t\bar{t}$ rest reference system (top right), 1st leading top-quark p_T (bottom left) and 2nd leading top-quark p_T (bottom right). Results are only considered for the combination of the e^+e^-, $\mu^\pm e^\mp$ and $\mu^+\mu^-$ channels.
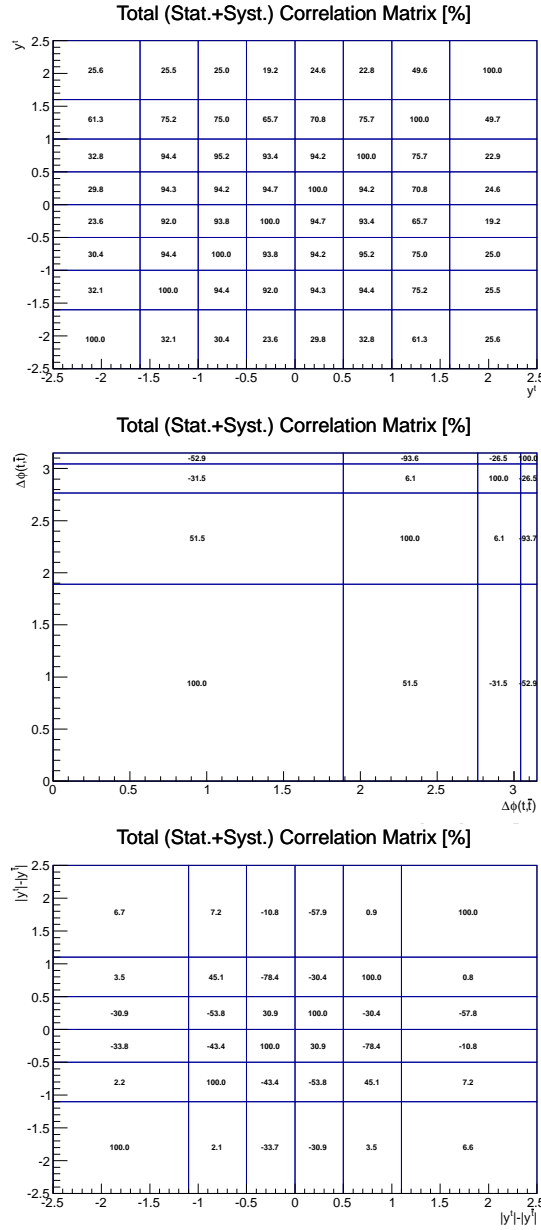
Figure 66: Covariance matrix of all systematic uncertainties for the top-quark y (top left), azimuthal angle difference between both top quarks $\Delta\phi(t,\bar{t})$ (top right) and rapidity difference between both top quarks $|y^{t}| - |y^{\bar{t}}|$ (bottom). Results are only considered for the combination of the e^+e^-, $\mu^\pm e^\mp$ and $\mu^+\mu^-$ channels.
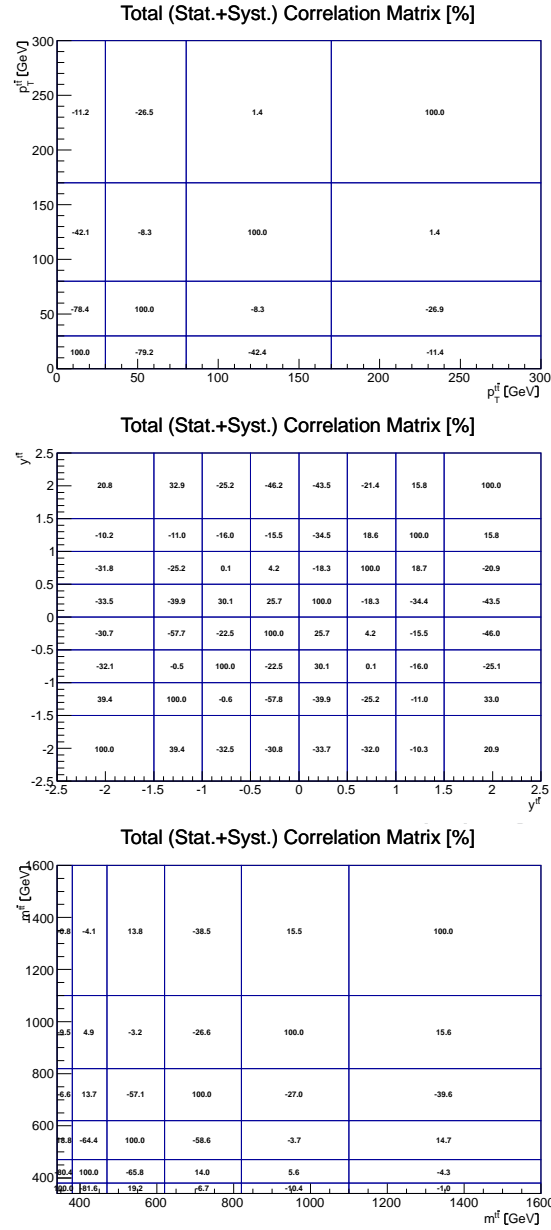
Figure 67: Covariance matrix of all systematic uncertainties for the top-quark-pair p_T (top left), rapidity y (top right) and invariant mass m (bottom). Results are only considered for the combination of the e^+e^-, $\mu^\pm e^\mp$ and $\mu^+\mu^-$ channels.

References

[1] A. Ferroglia, B. D. Pecjak, and L. L. Yang, "Top-quark pair production at high invariant mass: an NNLO soft plus virtual approximation", *JHEP* **1309** (2013) 032, `doi:10.1007/JHEP09(2013)032`, `arXiv:1306.1537`.

[2] Li, Hai Tao and Li, Chong Sheng and Shao, Ding Yu and Yang, Li Lin and Zhu, Hua Xing, "Top quark pair production at small transverse momentum in hadronic collisions", *Phys. Rev. D* **88** (Oct, 2013) 074004, `doi:10.1103/PhysRevD.88.074004`.

[3] N. Kidonakis, "NNLL threshold resummation for top-pair and single-top production", (2012). `arXiv:hep-ph/1210.7813.`.

[4] D0 Collaboration, "Measurement of the top quark mass using dilepton events. DØ Collaboration", *Phys. Rev. Lett.* **80** (1998) 2063–2068, `doi:10.1103/PhysRevLett.80.2063`, `arXiv:hep-ex/9706014`.

[5] J. Andrea et al., "Measurement of the Top quark mass with fully-leptonic t -t decays in pp collisions at $\sqrt{s}$ = 7 TeV with the full 2010 dataset",. CMS AN-2010/369.

[6] J. Alwall et al., "MadGraph v5: going beyond", *JHEP* **06** (2011) 128, `doi:10.1007/JHEP06(2011)128`, `arXiv:1106.0522`.

[7] S. Frixione and B. R. Webber, "Matching NLO QCD computations and parton shower simulations", *JHEP* **06** (2002) 29, `arXiv:hep-ph/0204244`.

[8] S. Alioli et al., "NLO single-top production matched with shower in POWHEG: *s*- and *t*-channel contributions", *JHEP* **09** (2009) 111, `doi:10.1088/1126-6708/2009/09/111`, `arXiv:0907.4076`.

[9] S. Alioli et al., "A general framework for implementing NLO calculations in shower Monte Carlo programs: the POWHEG BOX", *JHEP* **06** (2010) 043, `doi:10.1007/JHEP06(2010)043`, `arXiv:1002.2581`.

[10] E. Re, "Single-top Wt-channel production matched with parton showers using the POWHEG method", *Eur. Phys. J. C* **71** (2011) 1547, `doi:10.1140/epjc/s10052-011-1547-z`, `arXiv:1009.2450`.

[11] The CMS Collaboration, "Measurement of differential top-quark-pair production cross sections in pp collisions at $\sqrt{s}$ = 7 TeV", (2012). `arXiv:hep-ex/1211.2220`. Submitted to EPJC.

[12] JSON file `/afs/cern.ch/cms/CAF/certification/Collisions12/8TeV/` `Reprocessing/Cert_190456-208686_8TeV_22Jan2013ReReco_` `Collisions12_JSON.txt`.

[13] The CMS Collaboration, "CMS Luminosity Based on Pixel Counting - Summer 2012 Update",. CMS PAS LUM-12-001.

[14] T. Sjostrand, S. Mrenna, and P. Z. Skands, "PYTHIA 6.4 Physics and Manual", *JHEP* **05** (2006) 026, `doi:10.1088/1126-6708/2006/05/026`, `arXiv:hep-ph/0603175`.

[15] P. Artoisenet et al., "Automatic spin-entangled decays of heavy resonances in Monte Carlo simulations", *JHEP* **03** (2013) 015, `doi:10.1007/JHEP03(2013)015`, `arXiv:1212.3460`.

[16] G. Corcella et al., "HERWIG 6.5: An event generator for hadron emission reactions with interfering gluons (including supersymmetric processes)", *JHEP* **01** (2001) 010, `doi:10.1088/1126-6708/2001/01/010`, `arXiv:hep-ph/0011363`.

[17] `https://twiki.cern.ch/twiki/bin/view/CMS/StandardModelCrossSectionsat8TeV`.

[18] `https://twiki.cern.ch/twiki/bin/view/CMS/SWGuidePAT`.

[19] `https://twiki.cern.ch/twiki/bin/view/CMS/TWikiTopRefEventSel`.

[20] CMS Collaboration, "Determination of the Jet Energy Scale in CMS with pp Collisions at $\sqrt{s} = 7$ TeV",. PAS JME-10-010.

[21] `https://twiki.cern.ch/twiki/bin/view/CMS/JetID`.

[22] The CMS collaboration, "Identification of b-quark jets with the CMS experiment", *Journal of Instrumentation* **8** (2013), no. 04, P04013.

[23] CMS Collaboration, "Performance of b tagging at sqrt(s)=8 TeV in multijet, ttbar and boosted topology events", Technical Report CMS-PAS-BTV-13-001, CERN, Geneva, 2013.

[24] `https://twiki.cern.ch/twiki/bin/view/CMS/BTagSFMethods#2a_Jet_by_jet_updating_of_the_b`.

[25] P. Harris et al., "Reducing pileup dependence of $\not{E}_T$ with a pileup jet identifier and a multivariate regression technique",. CMS Note 2012/226.

[26] CMS Collaboration, "Measurement of the tt production cross section and the top quark mass in the dilepton channel in pp collisions at $\sqrt{s} = 7$ TeV", *JHEP* **1107, 049** (2011) `arXiv:1105.5661`.

[27] The CMS Collaboration, "Measurement of the $t\bar{t}$ production cross section in the dilepton channel in pp collisions at $\sqrt{s} = 7$ TeV", (2012). `arXiv:hep-ex/1208.2671`. Submitted to JHEP.

[28] The CMS Collaboration, "Measurement of the $t\bar{t}$ production cross section in the filepton channel in pp collisions at $\sqrt{s} = 8$ TeV ",. PAS TOP-12-007 (2012).

[29] CMS Collaboration Collaboration, "Measurement of the $t\bar{t}$ production cross section in the dilepton channel in pp collisions at $\sqrt{s}$=8 TeV", *J. High Energy Phys.* **02** (Dec, 2013) 024. 29 p.

[30] G. Bauer et al., "Modeling of $W \to l\nu$ MET with Boson Recoil",. CMS Analysis Note 2010/332.

[31] CMS Collaboration, "Measurement of the differential top-quark pair production cross section in the dilepton channel in pp collisions at $\sqrt{s} = 8$ TeV",.

[32] L. Sonnenschein, "Analytical solution of ttbar dilepton equations", *Phys.Rev.* **D73** (2006) 054015, `doi:10.1103/PhysRevD.78.079902,10.1103/PhysRevD.73.054015`, `arXiv:hep-ph/0603011`.

[33] CDF Collaboration, "Measurement of the top quark mass using template methods on dilepton events in $p\bar{p}$ collisions at $\sqrt{s}$ =1.96 TeV", *Phys. Rev. D* **73** (Jun, 2006) 112006, `doi:10.1103/PhysRevD.73.112006`.

977 [34] J. Kieseler, C. Diez Pardos, "Dilepton trigger and lepton identification efficiencies for the
978 top quark pair production cross section measurement at 8 TeV in the dilepton decay
979 channel",. CMS AN-12-389.

980 [35] "Uncertainty on the differential shapes" in BTV TWiki `https://twiki.cern.ch/`
981 `twiki/bin/viewauth/CMS/BtagPOG#2012_Data_and_MC_EPS13_prescript`.

982 [36] The CMS Collaboration, "Determination of the Jet Energy Scale in CMS with pp
983 collisions at $\sqrt{s} = 7$ TeV",. PAS JME-10-010 (2010).

984 [37] `https://twiki.cern.ch/twiki/bin/view/CMS/JetResolution#JER_`
985 `Scaling_factors`.

986 [38] Particle Data Group Collaboration, "Review of Particle Physics (RPP)", *Phys.Rev.* **D86**
987 (2012) 010001, `doi:10.1103/PhysRevD.86.010001`.

988 [39] A. Hoecker and V. Kartvelishvili, "SVD Approach to Data Unfolding",
989 *Nucl.Instrum.Meth.* **A372** (1996) 469–481, `doi:10.1016/0168-9002(95)01478-0`,
990 `arXiv:hep-ph/9509307v2`.

991 [40] V. Blobel, "An unfolding method for high energy physics experiments",
992 `arXiv:0208022`.

993 [41] F. James, "Statistical methods in experimental physics". World Scientific, second edition,
994 2006.

995 [42] `https://wiki.terascale.de/index.php?title=PDF4LHC_WIKI`.